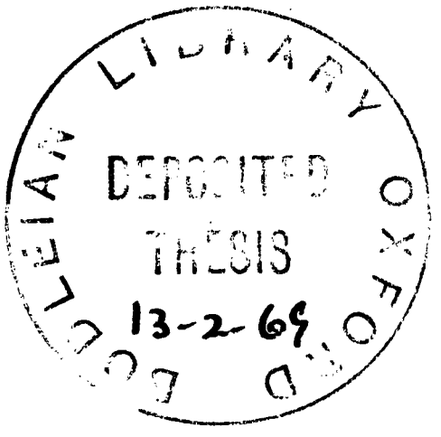
Some Chemical Applications of Magnetic Resonance

A thesis submitted in partial fulfilment of the requirements for the degree of Doctor of Philosophy

by

James D. Halliday



Lincoln College
Oxford

December, 1968

Acknowledgements.

I wish to express my gratitude to Professor R.E. Richards, F.R.S. for his constant interest and encouragement throughout the course of this work.

I would also like to acknowledge the invaluable assistance of my colleagues Dr. H.D.W. Hill and Dr. R.R. Sharp, without whom this work would probably never have been completed. My thanks go also to Dr. I. Campbell and Mr. C. Hall for much assistance and many helpful discussions and to all the other members of the group, too numerous to name but never forgotten, for helping to make my three years in Oxford so enjoyable.

The author also acknowledges the receipt of a grant from the Viscount Rothermere, through the Rothermere Fellowship Trust, University College, London.

Contents

	Page
Chapter 1. Signal to Noise in n.m.r.	1
1.1 Introduction	
1.2 The Magnetic Resonance Experiment	2
1.3 Improvement in the Signal to Noise ratio	4
1.4 Conclusion	
Chapter 2. The Magnet:-Description	8
2.1 Introduction	8
2.2 Design of High Homogeneity Superconducting Solenoids	10
2.3 The Magnet	11
2.4 Support System	15
2.5 The Dewar	15
2.6 Helium Recovery	16
2.7 Helium Level Indicator	17
Chapter 3. The Magnet:-Experiments	18
3.1 Introduction	18
3.2 Operation of the Solenoid	19
3.2.1. Pre-cooling	19
3.2.2. Cooling with liquid helium	20
3.2.3. Replenishment of liquid helium in the cryostat.	20
3.2.4. Replenishment of liquid nitrogen	21

3.2.5. Energizing the solenoid 22

3.2.6. Observations 23

3.3 Initial difficulties 24

3.3.1. The solenoid 24

3.3.2. The dewar 25

3.4 Reducing the liquid helium boil-off 27

3.5 Field Homogeneity Tests 28

3.5.1. Probe for Field Plotting 28

3.5.2. Remanent fields 30

3.5.3. Field Profiles 32

3.6 Homogeneity Improvement with Gradient Cancelling Coils 35

3.6.1. Superconducting gradient cancelling coils 35

3.6.2. Room temperature gradient cancelling coils 36

Chapter 4. The Spectrometer 38

4.1 Introduction 38

4.2 Description 38

4.3 The Probes 42

4.4 Sample Changing 46

4.5 Sample Temperature Control 47

4.6 Performance of the Spectrometer 48

4.7 Problems encountered with the spectrometer 49

4.7.1. Low frequency noise 49

4.7.2. Modulation pick-up 50

4.7.3. Homogeneity degradation 50

Chapter 5. The Chemical Shift in Alkali Halide Ions 52

5.1 Introduction 52

5.2 Chemical Shifts in Alkali Halide Crystals 53

5.3 Chemical Shifts of Alkali Halides in Solution 57

5.4 Calculation of the Ion-Ion Contribution to the chemical shift of alkali halides in solution 58

5.4.1. The theory 59

5.4.2. Determination of form of (R) 62

Chapter 6. $^{133}Cs^{+}$ Chemical Shifts in Aqueous Solution 67

6.1 Introduction 67

6.2 Experimental 68

6.3 Results 71

6.4 Discussion 73

6.4.1. Introduction 73

6.4.2. Predictions of the proposed theory for ion-ion contribution to the chemical shift 74

6.4.3. Solvent isotope effects 78

Chapter 7. ^{133}Cs Chemical Shifts in mixed and non-aqueous solvents 82

7.1 Introduction

7.2 Experimental 82

7.3 Results 85

7.4 Discussion 85

Appendix. Chemical Shift data 89

References 97

Abstract 101

Chapter 1. Signal to Noise in n.m.r.

1.1 Introduction

Ever since the first successful observations of nuclear magnetic resonance signals by Bloch (1) and Purcell (2) n.m.r. spectroscopists have endeavoured to improve the sensitivity of the technique.

Many nuclei of interest have low natural abundance and/or low sensitivities. These include ^{13}C, ^{15}N, ^{17}O. The last has been used to elucidate information on ion-solvent interactions in solutions of several alkali metal salt solutions (3).

N.m.r. is now becoming a useful technique for research in the life sciences, especially biochemistry, where proton measurements are commonplace and other nuclei are being used as probes to determine the position and conformation of active sites in large biological molecules. The ^{35}Cl resonance has recently been used for this purpose (4).

For some years now this research group has been interested in the properties of electrolytes, alkali halides in particular, in aqueous and non-aqueous solutions (5 - 10). One aspect of these solutions that has not been investigated due to sensitivity limitations is solute interactions at low concentrations. There has been little overlap between the concentration ranges studied by conductivity measurements and by n.m.r. To overcome this limitation it was hoped to design and construct a spectrometer that would be more versatile and sensitive than any commercially available.

This chapter will introduce the n.m.r. experiment and comment on those factors that influence its sensitivity.

1.2 The Magnetic Resonance Experiment, Continuous Wave Method.

The sample is placed in a coil tuned to the Larmor frequency and the assembly is put into a magnetic field H_o. A rotating field H_1 is induced by energizing the coil from an r.f. generator. When the H_1 rotation reaches the Larmor frequency resonance occurs. The voltage induced in the coil by the nuclear magnetization is measured at the same time as it is being driven by the H_1 field. To aid detection it is desirable to allow only the signal voltage to reach the receiver. This is accomplished by using a balancing technique, either a radiofrequency bridge (single coil) (11) or a geometrical balance (crossed coil system) (12).

Both these methods have the same limiting signal to noise ratio (13) :

$$\frac{v_s}{v_n} = k \frac{\eta\, Q^{\frac{1}{2}}\, \omega_o^{\frac{1}{2}}\, V_c^{\frac{1}{2}}}{(F.\ 4kT.\ \Delta f)^{\frac{1}{2}}} \cdot 2\chi H_1 \qquad 1$$

where k is a numerical factor (1) depending on the geometry of the coil

η is the 'filling factor', i.e. the volume of the sample divided by the volume of H_1 field produced by the coil

Q is the 'quality factor' of the coil

V_c is the volume of the H_1 field produced by the coil

ω_o is the Larmor frequency

F is the 'noise figure' of the detection apparatus

Δf is the effective band width of the detection system

H_1 is the amplitude of the rotating field and χ is the complex magnetic susceptibility where $\chi = \chi' - i\chi''$ The component of the susceptibility, χ', which is in-phase with H_1 is the dispersion mode and the out-of-phase component, χ'', is the absorption mode.

Solution of the Bloch Equations yields (14) :

$$\chi' = \tfrac{1}{2}\chi_0 \omega_0 T_2 \left\{ \frac{(\omega_0 - \omega)T_2}{1 + (\omega_0 - \omega)^2 T_2^2 + \gamma^2 H_1^2 T_1 T_2} \right\} \qquad 2$$

$$\chi'' = \tfrac{1}{2}\chi_0 \omega_0 T_2 \left\{ \frac{1}{1 + (\omega_0 - \omega)^2 T_2^2 + \gamma^2 H_1^2 T_1 T_2} \right\} \qquad 3$$

where T_1 and T_2 are the spin-lattice and spin-spin relaxation times respectively.

The resonant nature of the signal is apparent from equations 2 and 3. To observe true line shapes saturation must be avoided (i.e. $\gamma^2 H_1^2 T_1 T_2 \ll 1$). Under these conditions the peak value of χ'', when $\omega = \omega_0$, is

$$\chi''_{peak} = \tfrac{1}{2}\chi_0 \omega_0 T_2 \qquad 4$$

The peak signal amplitude can be increased by introducing a certain amount of saturation. The product $\chi'' H_1$ reaches a maximum given by

$$(\chi'' H_1)_{max} = \frac{1}{4}\frac{\chi_0 \omega_0}{\gamma}\left(T_2/T_1\right)^{\frac{1}{2}} \qquad 5$$

when $\gamma^2 H_1^2 T_1 T_2 = 1$

Under these conditions significant distortion of the line shape occurs; a Lorentzian line is broadened to twice its natural width.

Combining equations 1 and 4 or 5, we have

$$\left(\frac{v_s}{v_n}\right)_{\substack{absorption \\ peak}} = K \frac{\eta Q^{\frac{1}{2}} \omega_0^{\frac{3}{2}} V_c^{\frac{1}{2}}}{(F.\ 4kT.\ \Delta f)^{\frac{1}{2}}} \frac{\chi_0 T_2}{2} H_1 \qquad 6$$

when there is no saturation of the signal, and

$$\left(\frac{v_s}{v_n}\right)_{\substack{\text{absorption}\\ \text{peak max.}}} = k\,\frac{\eta\, Q^{\frac{1}{2}}\,\omega_o^{\frac{3}{2}}\,V_c^{\frac{1}{2}}}{(F.\,4kT.\,\Delta f)^{\frac{1}{2}}}\,\frac{\chi_o}{4}\left(\frac{T_2}{T_1}\right)^{\frac{1}{2}} \qquad 7$$

for the maximum attainable absorption signal.

1.3 Improvement in the Signal to Noise ratio.

Methods for improvement may be broadly separated into two groups:

1) Physical changes in the conditions under which resonance occurs to increase the magnitude of the signal from the sample.

2) Electronic manipulation of the signal by suitable methods to raise it as far as possible above background noise.

1.3.1 Physical factors determining magnitude of magnetic resonance signal.

In equations 6 and 7 the Larmor frequency ω_o appears to the $3/2$ power, i.e. the signal to noise ratio increases as $H_o^{\frac{3}{2}}$. This is the dominating term in the equations as it is the only one with >1 power dependence.

Until 1964 the maximum magnetic field that was available for n.m.r. experiments was ~ 25 kilogauss, the saturation point for iron core electromagnets. To obtain fields beyond this great amounts of power were required and the fields produced were far from being very homogeneous. In that year Varian Associates produced a superconducting solenoid operating at 47 kilogauss with a very homogeneous field over a 5 mm. diameter sample. A new step had been taken in the improvement of sensitivity.

The relationship, signal to noise improvement $\propto H_o^{\frac{3}{2}}$, holds for frequencies $< 200 MH_z$. At this point the effective gain in signal to

noise is approximately linear with increasing field due to losses in the r.f. system (15).

The other terms of equations 6 and 7 are significant, especially the sample volume, represented by η and V_c. As large a sample as possible, to contain the maximum number of resonating nuclei, should be used providing the homogeneity over the sample can be maintained.

The inhomogeneity of the magnetic field, H_o, should be less than the line width of the nuclear resonance. If it is not, the appropriate value of T_2 in equations 6 and 7 becomes $2/\gamma\Delta H$ (16) where ΔH is the magnet inhomogeneity.

1.3.2. Electronic techniques for increasing signal to noise ratio.

The sensitivity can be appreciably increased by the use of suitable electronic techniques for signal detection and processing.

In equations 6 and 7 the term $(F.\ 4kT.\Delta f)^{\frac{1}{2}}$ allows for the thermal noise generated in the system and the noise from all other sources in the spectrometer. Possible sources for this are: radiofrequency generator, receiver, variation in receiver gain, and drift in d.c. amplifiers. The need for d.c. amplifiers can be eliminated if the signal is modulated, usually with a frequency in the audio region. The signal then has a.c. components as well as the d.c. one. The first a.c. component can be r.f. phase detected and the signal at the modulation frequency further amplified and a.f. phase detected with a lock-in amplifier. This usually supplies the modulation frequency and provides a very narrow bandwidth at the same frequency for detection. Therefore the noise, which extends over the entire bandwidth of the system, is greatly reduced.

The most common modulation technique is to apply a sinusoidal field modulation (or equivalent frequency modulation) as the resonance line is scanned. However, with modulation other difficulties arise. Parts of the probe may respond mechanically to the modulation frequency giving rise to an unwanted background signal that is detected and amplified with a phase-sensitive detector.

The detected signal depends upon the modulation frequency ω_m and the modulation amplitude H_m. When ω_m and H_m are small compared with the resonance line width $\Delta\omega$, the output of the audio-phase detector is proportional to the derivative of the absorption or dispersion mode, depending on which mode is selected at the r.f. phase detector. The amplitude of the resultant signal is proportional to H_m but is only a fraction of the maximum possible signal in the absence of modulation, if distortion is to be avoided.

When $\omega_m \gg \Delta\omega$ the separate harmonics (sidebands) of the signal become well separated and any one may be detected. Howarth and Richards (17) discuss this modulation technique and illustrate the output from the four possible r.f., a.f. phase combinations, with modulation index $\beta = 1$. (Figure 1.1)

If combination 4 is used, with $\beta = 1.8$, the centreband becomes 1.16 times the d.c. component (18) and the first sidebands are reduced to zero.

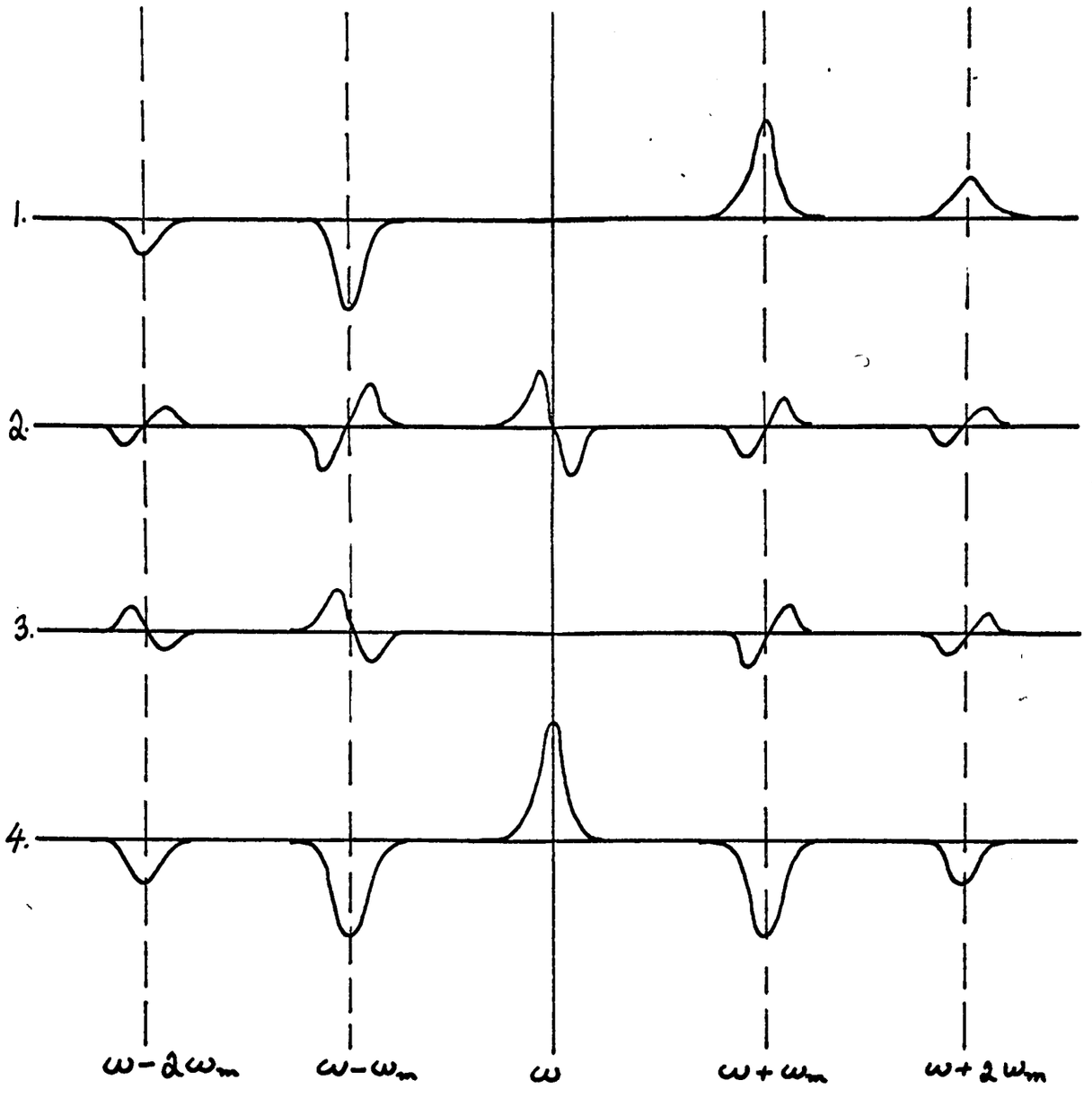


Figure 1.1 Centrebands and sidebands for the first a.c. component for the phase settings (1) r.f. out, a.f. in, (2) r.f. out, a.f. out, (3) r.f. in, a.f. in, (4) r.f. in, a.f. out.

An additional aid that can be employed is the digital memory oscilloscope, sometimes referred to as a CAT (Computer for Averaging Transients). The CAT digitizes the spectrum and stores the amplitude of each point in its memory. If the signal is scanned repetitively it adds linearly as N, the number of scans, while the noise, since it is random, adds as $N^{\frac{1}{2}}$ (19). This method is most advantageous when the noise increases towards the low frequencies where multiple scan measurements will give a greater signal to noise improvement than a single scan lasting the same total time (20).

1.4 Conclusion.

As mentioned at the beginning of this chapter it was hoped to construct a spectrometer that would prove more versitile and sensitive than any commercially available. Themagnetic field is shown to be important so a 50 kilogauss superconducting solenoid is used as the magnetic field source. The other factors affecting the signal to noise ratio have also been carefully considered when designing the spectrometer. Where possible optimum advantage is taken to improve the spectrometer sensitivity.

Some properties of the superconducting wire used to manufacture the solenoid are discussed next in Chapter 2. A detailed description of the solenoid and its related cryogenic apparatus is also given.

Chapter 2. The Magnet:- Description

2.1 Introduction.

To achieve the field at which we wished to work, 50 kilogauss, it was decided that a high homogeneity superconducting solenoid would be necessary.

These only became a reality this decade. For, although superconductivity was discovered in 1911 by Ohnes, it was not until recently that superconducting materials that had a high critical field with a high current density were developed. The three most useful are the alloys Nb/Zr and Nb/Ti and the compound Nb_3Sn.

In 1965 only Nb/Zr 25% was available in a form suitable for winding into a high homogeneity solenoid.

Superconducting wires, Nb/Zr in particular and type 11 superconductors in general, have some properties that should be mentioned to shed light on the difficulties encountered in the construction of our solenoid.

1) Nb/Zr, a type 11 superconductor, in the hardworked state has a knee in its Critical Current-Critical Field graph (Figure 2.1) This knee is important in that it permits a high field to be achieved at a high current density.

2) Type 11 superconductors behave differently from type 1 superconductors in their Magnetization vs. Field curves (Figure 2.2). It is the breakup of the type 11 superconductor into a mixed state of a filamentary structure of normal and superconducting regions between H_{c_1} and H_{c_2}, the field at which superconductivity is finally suppressed, that makes possible high fields.

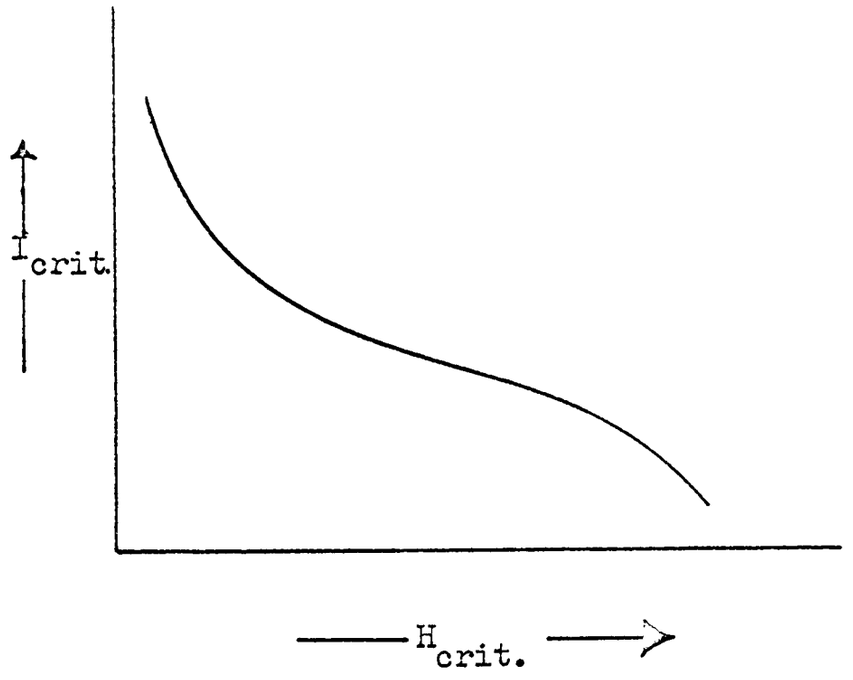


Figure 2.1 Critical current vs critical field curve for a hard-drawn type 11 superconductor.

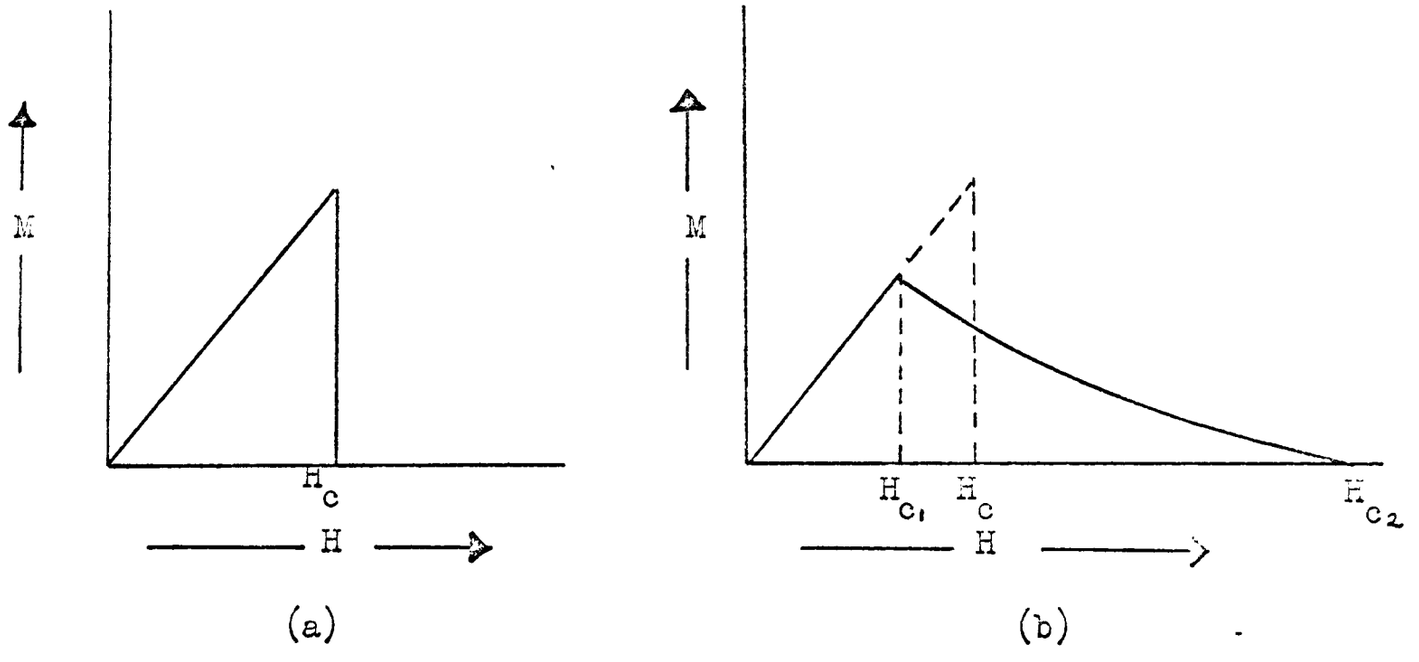


Figure 2.2 Magnetization curves for a) Type 1 superconductor
b) Type 11 superconductor

3) Quite often, during the energizing of a solenoid, it will quench at a field much lower than its critical field. It was shown in 1964 (21) that as the solenoid field was increased there were short sharp changes of a few tens of gauss superimposed on it with a time duration ranging from 10 to 500 usec. These rapid field fluctuations were attributed to 'flux jumps', caused by whole domains changing their state of magnetization.

Occasionally the energy of a flux jump is sufficient to initiate the formation of a normal region in the wire. Energy is then dissipated there and within a fraction of a second the normal region spreads and the field collapses. Unless the wire is very well protected the energy expended is sufficient to fuse the wire and destroy the coil locally.

4) The wire can be protected against damage caused by quenches to a certain extent by enclosing it in a tightly adhering copper sheath. The copper acts as a good conductor for the heat generated during the quench. However the copper sheath plays another important part. Since copper at 4.2°K is approximately 1000 times better as a conductor than Nb/Zr in its normal state (22), it provides a temporary path for the current should a flux jump introduce a normal region in the wire. Provided that the wire is cooled sufficiently fast the normal region is brought back to its superconducting state and no quench occurs. Without the sheath the superconducting wire is prone to quenching since all flux jumps are likely triggers.

2.2 Design of High Homogeneity Superconducting Solenoids.

Even though a right circular superconducting solenoid of uniform cross section can produce fields of 50 kilogauss, the field over a volume of 1 cm^3 is not sufficiently homogeneous for high resolution n.m.r. experiments. The homogeneity may be improved by the manipulation of the current distribution in the solenoid. Basic methods for doing this were proposed by Helmholtz, two coils, and by Maxwell, three coils axially symmetric (23). An improved technique has been devised by Garrett (24, 25), whereby the cross section of a right circular solenoid made up of many turns, each carrying the same current, is altered in such a way that there are more turns at the ends than the centre. In this way remarkably good homogeneities are theoretically possible.

Three ways of increasing the number of turns at the ends of a solenoid are shown in figure 2.3. For practical reasons the most commonly used design is 'a'.

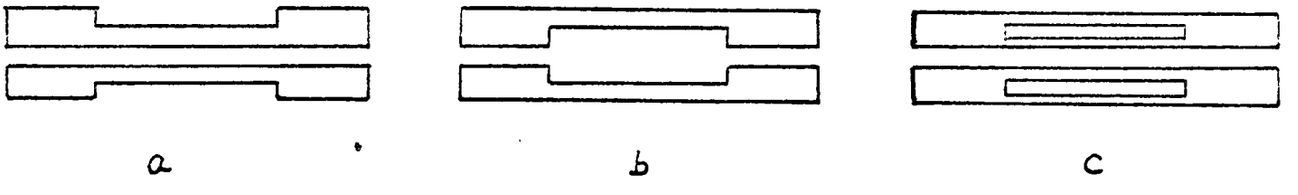


Figure 2.3 Various configurations for Garrett compensated solenoids.

The design for a fully compensated solenoid with the Garrett correcting coils on the outside of the main winding is known as an outside-notch sixth-order solenoid. The term sixth-order indicates the degree to which the solenoidal field has been flattened through the action of the compensating coils. This terminology is of mathematical origin and stems from the fact that the field may be expanded about the geometric centre. Since there is a plane of symmetry through the centre all odd order terms vanish. The end coils can fully correct for the 2nd and 4th order terms, thus leaving a net contribution to the 6th order and higher terms.

This was the design chosen for our solenoid, which will be fully described in the next section.

2.3 The Magnet

The solenoid used in this investigation (Figures 2.4 and 2.5) was designed in conjunction with the Oxford Instrument Co., Ltd., and subsequently manufactured, including its cryostat and support system, by them.

The solenoid was designed in the hope of producing a field of 50 kilogauss in a room temperature bore of 1" with a homogeneity of 1 in 10^6 over a sphere 1 cm. diameter.

The coil design chosen was a uniform multilayer solenoid with an outside pair of independently adjustable Garrett end correcting coils.(25) In magnet terminology, as described earlier, this is an outside notch sixth order solenoid.

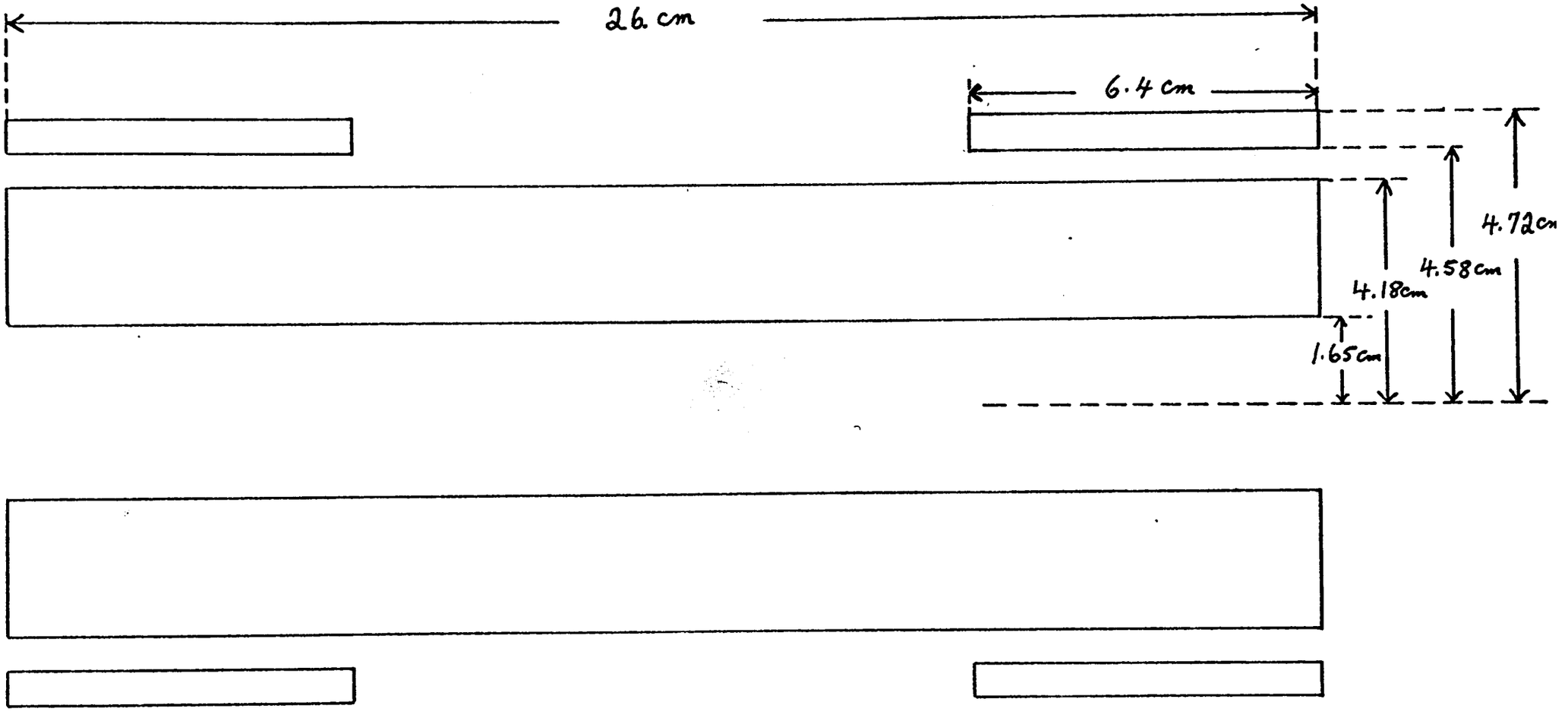
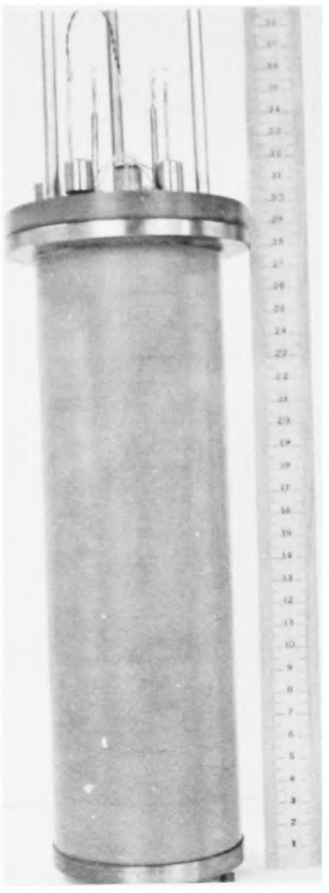
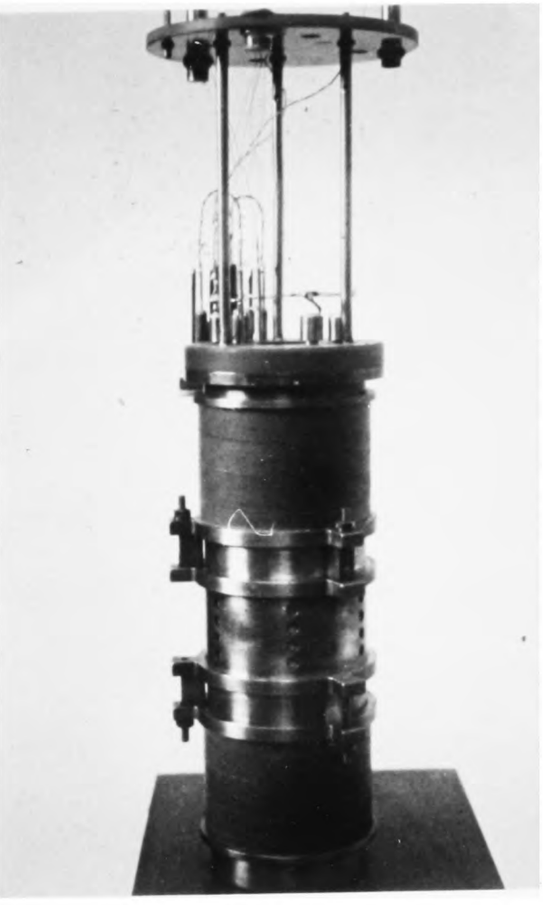


Figure 2.4 Solenoid dimensions



(a)



(b)



(c)



(d)

Figure 2.5 The solenoi[illegible] in various stages of construction.

Since superconducting wire is very expensive, an optimization technique is used to calculate the minimum size solenoid required to produce a given field, homogeneity, and bore diameter. This calculation carried out by the Oxford Instrument Co., Ltd., indicated a solenoid 18 cm. long with large and very critical end corrections. Since the maximum possible homogeneity was required for our nuclear magnetic resonance experiments and this coil left no margin for error in winding or other imperfections in the wire, it was decided that a larger solenoid would be preferable. Further calculations indicated that a 26 cm. solenoid would not be too much more costly and would provide the same homogeneity as the 18 cm. solenoid but with much smaller and less critical end corrections.

The superconducting wire used was Nb/Zr 25% alloy, 0.010" superconductor core, 0.001" electroplated copper sheath, and 0.001" Formvar insulation, 0.014" overall diameter.

The formers for the coils are made of copper, and this has a susceptibility and a coefficient of expansion approximating to that of the superconducting wire. In addition the copper, through its high conductivity, can provide an efficient means of heat transport from the centre of the solenoid to the helium bath in the advent of a quench.

The Garrett end correcting coils are wound on individual copper formers which fit on a cylinder that surrounds the main winding. Provision is made for mechanical adjustment of the positioning of the end coils on this cylinder to allow correction for any possible misalignment about the magnetic centre of the solenoid.

The main winding has 52783 turns in 72 layers and incorporates 3 lengths of wire with a total length of 34,600 feet. Interleaved between every third layer is a mylar-copper-mylar sheet (0.0002", 0.001", 0.0002") to provide more efficient heat conduction to the liquid helium bath.

The top end correcting coil has 742 turns in 4 layers with 0.001" mylar interleaving between each layer.

The bottom end correcting coil has 734 turns in 4 layers with no mylar interleaving.

The three coils are all wound so as to have the same space factor.

Each coil has its own superconducting switch. (Figure 2.5d) This switch allows the coil to be placed in the persistent mode. It is made by shorting the coil with a length of superconducting wire and winding a heating coil around this. Before energizing the coil the switch heater is turned on, thus raising the shorting wire above its transition temperature. The superconducting coil has zero resistance so current from the power supply will flow through it in preference to the switch. When the switch heater is shut off the shorting wire becomes superconducting and a closed superconducting loop is formed. There is now a standing current in the coil that will remain until the coil is raised above its transition temperature or the switch is opened by turning the heater back on. It is possible to pass a transport current through the switch without significantly disturbing the standing current provided that the ratio of the self-inductance of the coil to that of the switch is large. This permits the three coils

of the magnet to be connected as shown in figure 2.6. In this configuration only one pair of current leads are required, thus reducing heat inputs to the dewar. The currents in all three coils can be carried in unison or independently (exclusive of transformer coupling) by use of the superconducting switches.

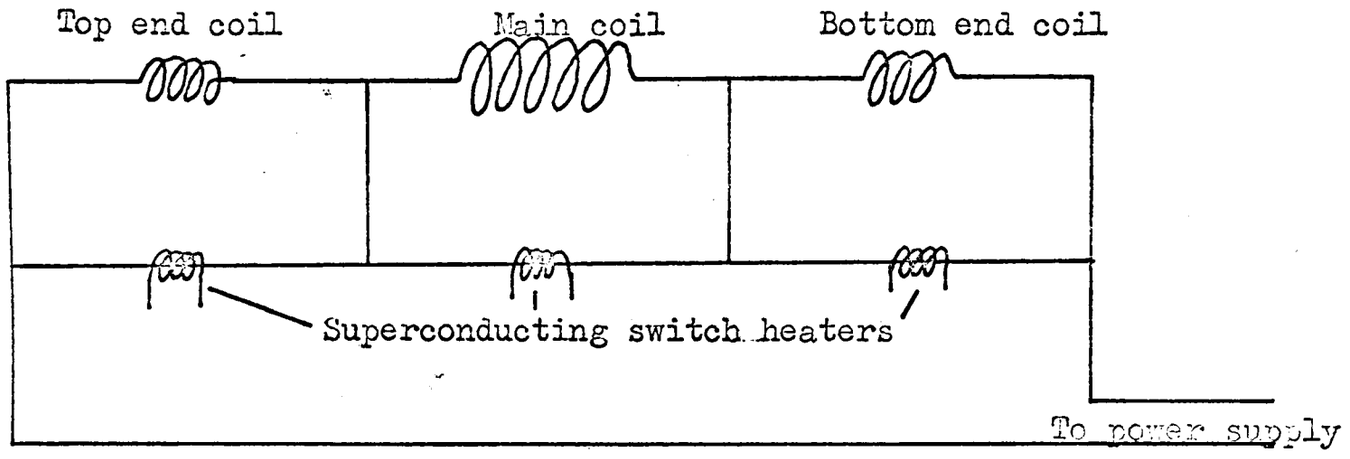


Figure 2.6 Connection of main and end correcting coils to permit individual operation butwith only one pair of current leads.

Adjustment of the current in each coil permits some degree of correction for possible winding imperfections and misalignment of the end coils.

A further refinement for improving the homogeneity of the solenoid is the incorporation of superconducting gradient cancelling coils. There are four mounted on a stainless steel cylinder that surrounds the magnet (Figure 2.5c). The coils will be described in Section 3.6.

The overall weight of the solenoid is ~9 kilograms.

2.4 Support System.

The solenoid is suspended in the dewar by the support system (Figure 2.7). This also provides on the top plate inputs for the liquid helium siphon and dip stick and an output pipe for the recovery of helium gas. Electrical connections are also made through seals in the top plate. Baffles on the support system act as radiation shields.

2.5 The Dewar.

The dewar (Figure 2.8) is mounted in a substantial aluminium framework. The plate from which the dewar is suspended is isolated from the rest of the frame by heavy duty antivibration mountings. The frame also provides a mounting space for the magnet power supply and other components.

The dewar is of conventional helium cryostat design with an insert in the bottom enabling room temperature access to the magnetic field.

The helium reservoir is widened to increase the helium capacity to 10 litres above the magnet. With a boiloff ≤ 120 cm^3 liquid helium/hour, this allows 2-3 days use without topping up.

To give the maximum room temperature working area the spacing between the dewar inserts is very close (0.030"). To enable the inserts to be positioned so accurately without touching the radiation shield



Figure 2.7 The magnet support system.

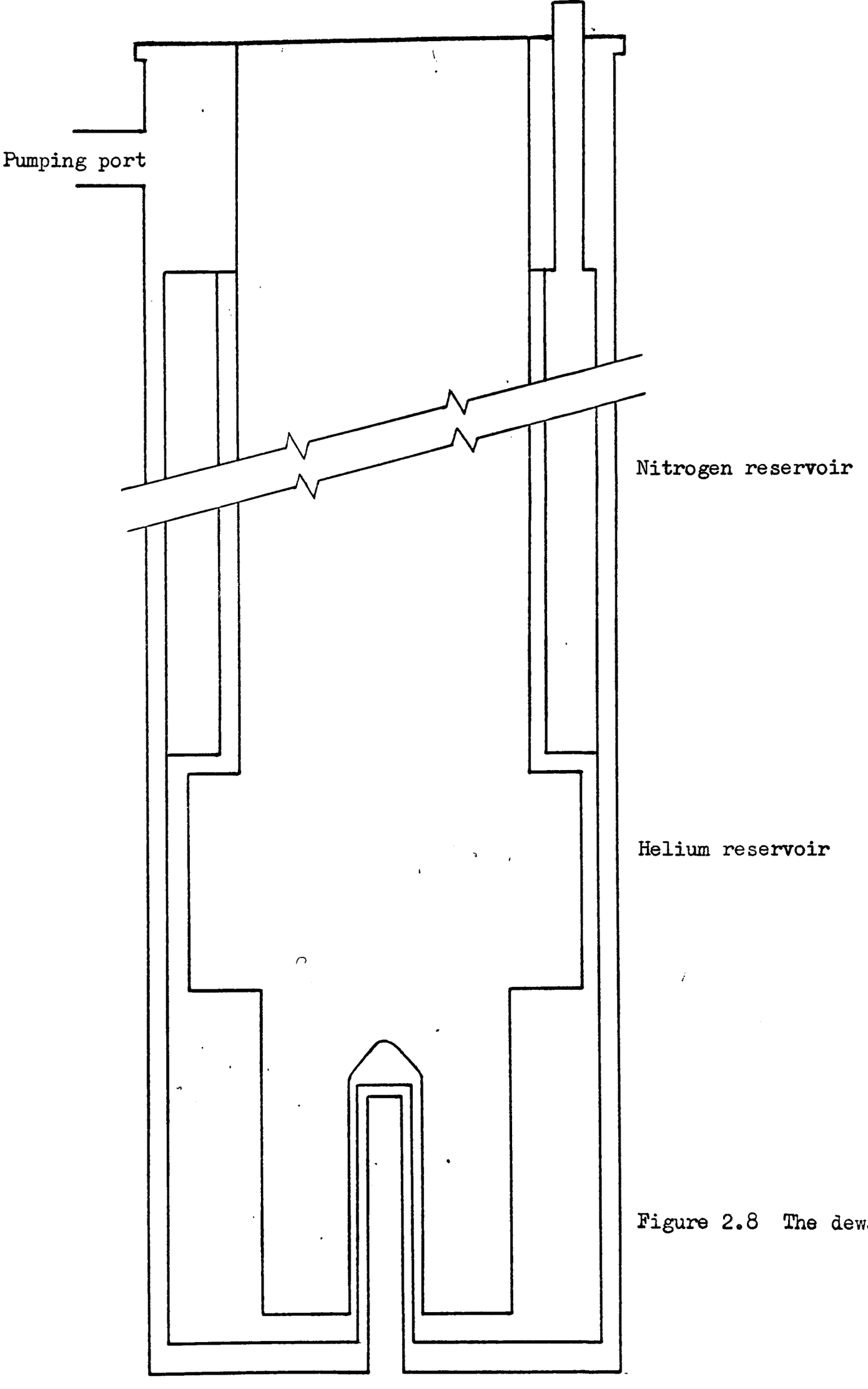


Figure 2.8 The dewar

and room temperature sections are adjustable. The radiation shield is electrically insulated from the rest of the dewar and connected to an insulated point on the pumping port by a copper wire brought up inside the vacuum space. By measuring the resistance between this and the dewar any touch between the radiation shield and either the helium can or the room temperature insert can be observed. Thus both inserts may be accurately positioned by a trial and error method of adjustment until a position is found that allows equidistant movement sideways without a touch occuring.

With the present stainless steel insert, to provide thermal isolation for variable temperature work, the room temperature access is 0.910" diameter.

The dewar vacuum jacket is evacuated with a rotary backing pump and oil diffusion pump. Before cooling the dewar with helium the vacuum jacket is isolated from the pumps. To prevent the possibility of any solid air trapped in the vacuum jacket of the dewar after long runs from causing pressures >1 atmosphere when the dewar is warm an atmospheric pressure release seal is fitted.

2.6 Helium Recovery.

The helium gas is recovered by collection in a low pressure rubber storage bag (capacity 3000 litres of gas) and then compressed into cylinders (2000 psi) by a Bristol compressor. The storage bag was counterweighted to eliminate the possibility of back pressure inducing

oscillations in the helium gas in the dewar. Advantage was taken of the movement of the counterwight to operate microswitches that control the starting and stopping of the compressor and this provides automatic control for the emptying of the storage bag.

Present figures indicate a helium recovery >95% with a 99.8 purity.

Total liquid helium consumption per week is ~34 litres.

2.7 Helium level indicator.

A continuously reading helium level indicator, designed by Dr. I. Campbell, has been recently incorporated into the system. It measures the change in capacitance between two concentric german silver tubes fixed to the top of the solenoid (Figure 2.9). It has the advantage of not dissipating any energy in the system as do the conventional carbon resistor level indicators.

Prior to this the level was determined by the use of a 'dip stick' (Figure 2.10). This is one of the simplest level indicators, consisting of a stainless steel tube, fitted with a rubber membrane on the top. It is based on the observation that when the cold end of a tube containing an oscillating gas column passes from the vapour into the liquid, the frequency of the oscillation decreases by ~30% and the intensity of the oscillation decreases by ~ 60% (26).

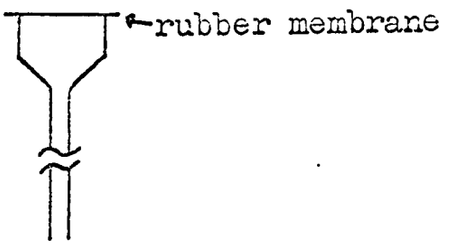
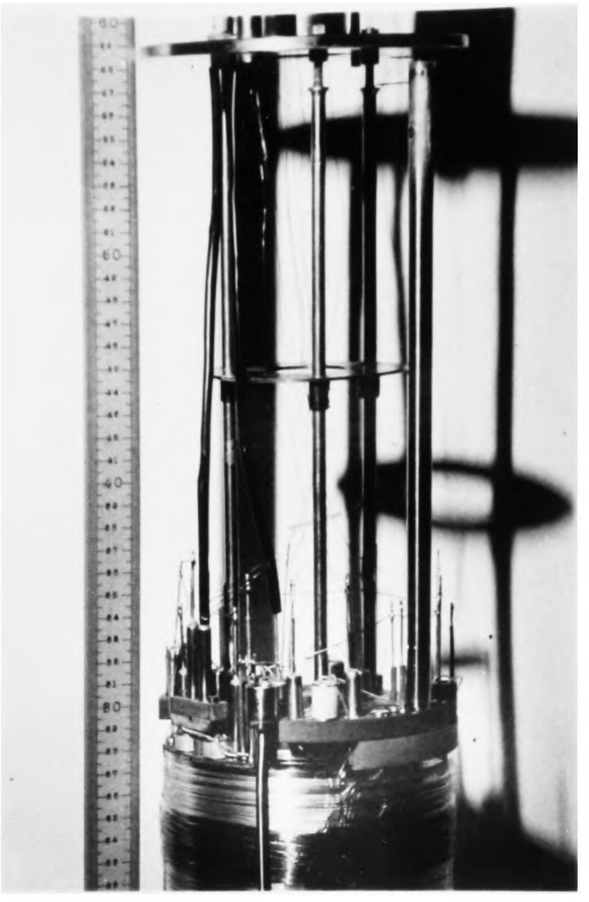


Figure 2.10 Oscillating gas column helium level indicator



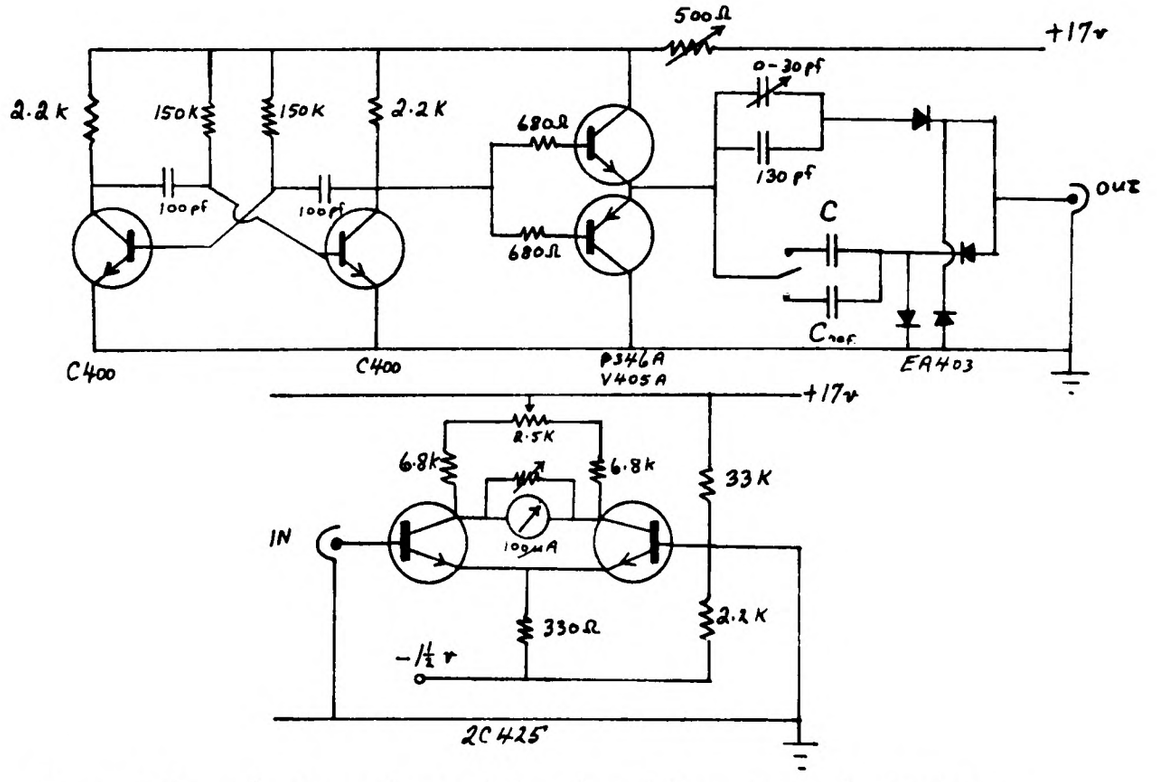


Figure 2.9 A) Capacitance tubes for Helium Level Indicator
B) Circuit for Helium Level Indicator

Chapter 3. The Magnet :- Experiments.

3.1 Introduction

At the inception of this project in February, 1963, very little was known about the construction and handling problems of high homogeneity superconducting solenoids. Varian Associates had demonstrated at a meeting of the N.Y. American Physical Society in January, 1964, a magnet operating at 47 kilogauss and the same magnet complete with 200 MHz, ^{1}H spectrometer at Pittsburgh in March of the same year.

The Oxford Instrument Co., Ltd., had experience of building small superconducting solenoids but had no accurate data on their field homogeneity or stability in the persistent mode.

It was naively assumed that the magnet could be used much like a conventional iron core electromagnet, the only difference being that it had first to be cooled to liquid helium temperature. Initial tests soon proved this assumption wrong. Cooling the magnet to $4.2^{o}K$ is a fairly lengthy procedure (described in Section 3.2) and consumes an appreciable quantity of liquid helium. In addition, after energizing the solenoid the magnetic field drifts and requires a period of at least a few days to reach a reasonably constant value. Initial field drift for the first few hours after being put into the persistent mode is quite rapid (Figure 3.1). After several weeks this drift falls to less than several parts in 10^{7} per week.

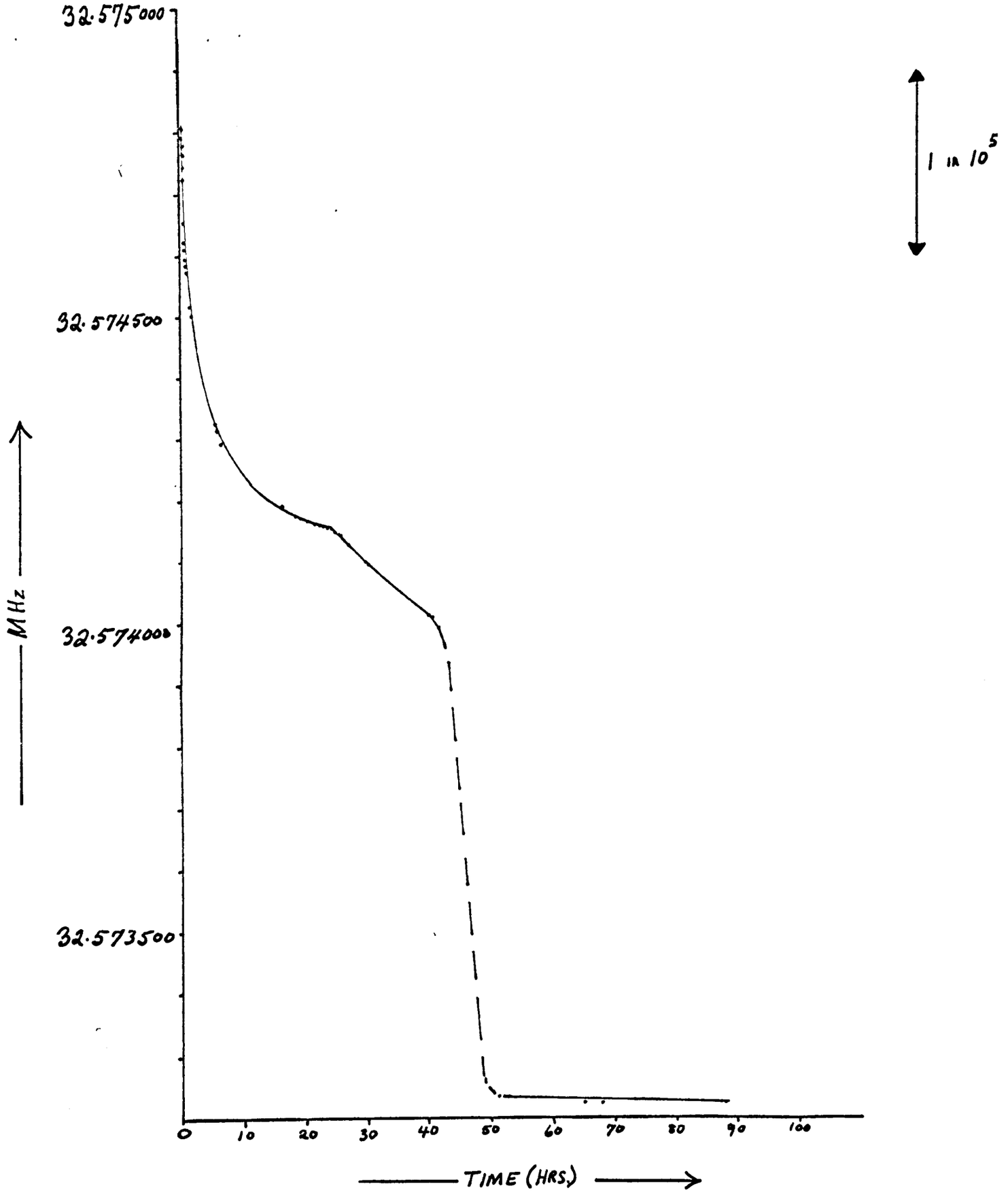


Figure 3.1 Initial Field Drift

Since the initial drift lessens with time it cannot be caused by a resistance. The most likely explanation is a rearrangement of the flux due in part to changes in the solenoid while reaching its new thermal equilibrium geometric configuration after being cooled to 4.2°K. This postulate is confirmed in part by the fact that the drift is usually less the longer the solenoid is left at 4.2°K before being energized.

3.2 Operation of the solenoid.

3.2.1. Pre-cooling

Liquid helium is a very inefficient and expensive coolant due to its low latent heat of vaporization (82 joule mole $^{-1}$). Helium gas at 4.2°K has a high enthalpy, but since it is difficult to optimize the gas flow rate about the solenoid, not very efficient use can even be made of this. Consequently it has been found most economical to cool the solenoid to 77°K with liquid nitrogen before attempting to cool with liquid helium.

Liquid nitrogen is poured on to the solenoid through the siphon inlet in the top plate of the magnet support system. It is added until the magnet is immersed. The liquid nitrogen is left surrounding the solenoid for several hours, usually overnight, to ensure complete cooling to 77°K.

It is doubtful if the marginal gain of a few °K is worth the effort of pumping on the nitrogen and so this has not been tried.

The liquid nitrogen remaining after the magnet has reached thermal equilibrium is blown out with helium gas through a thin-wall, narrow-bore tube inserted to the bottom of the dewar. It is essential, due to the high heat capacity of liquid nitrogen, that none is left in the dewar prior to filling with liquid helium.

3.2.2 Cooling with liquid helium.

As mentioned, the effective coolant is the gas from the vaporization of the liquid helium. To ensure that most of this gas comes into contact with the magnet and walls of the dewar the liquid helium is transferred from the storage vessel to the bottom of the dewar. A siphon extension is permanently attached to the outside of the solenoid for this purpose (Figure 2.5c). For complete heat exchange the liquid helium must be passed over very slowly. With a correctly controlled flow rate the magnet can be cooled to 4.2°K from 77°K in approximately one hour with the use of about four litres of liquid helium.

3.2.3 Replenishment of liquid helium in the cryostat.

It is worth noting here the procedure adopted for topping up the liquid helium in the dewar so that the magnet can be maintained in the persistant mode for extended periods. Great care has to be taken to ensure that no warm gas is allowed to come into

contact with the liquid helium in the dewar. To prevent this the helium purged siphon is inserted about six inches into the top of the dewar or so that it does not extend beyond the second baffle (Figure 2.7). The siphon is lowered to the top of the helium reservoir only when liquid helium is flowing through it. It is never pushed into the helium in the reservoir. The helium transport dewars are raised and lowered by means of an electrically operated fork lift truck built by the Littlemore Scientific Engineering Co., Oxford.

3.2.4 Replenishment of liquid nitrogen.

Since the liquid nitrogen in the radiation shield reservoir (capacity 20 litres) has a loss rate of approximately $\frac{1}{2}$ litre/hour, daily replenishment is required.

There are three equispaced access tubes to the nitrogen can and filling can be accomplished from any one. However, it was found that the filling tube must not be kept blocked after the addition of the liquid nitrogen. If it is that tube reaches a higher equilibrium temperature that the other two. There is sufficient expansion and contraction to marginally twist the nitrogen can, including the attached radiation shield, to one side and cause a touch between the radiation shield and the room temperature insert. This is only temporary and disappears immediately after the outlet is unblocked.

3.2.5 Energising the solenoid.

The current to the solenoid is measured by the voltage drop across a $7.86 \times 10^{-3}\,\Omega$ resistor outside the dewar in series with the magnet. The inductive voltage across the superconducting switches as the current is increased is monitored with a fast response voltmeter. The sweep rate of the current is adjusted to keep this $< 0.5V$. Any instabilities of the current in the solenoid, such as flux jumps, can be observed as a sudden change in the inductive voltage.

The power supply has a magnet protection cutout circuit that operates if it senses voltage changes $\geqslant 3V$. However, voltage spikes on the 3 phase mains occasionally exceed this and cause the power supply to shut down. The resulting rapid decay of the current in the solenoid causes sufficient joule heating to bring the solenoid above its transition temperature and therefore quench. However, much of the current is dumped into the power supply before the magnet quenches and very little helium is lost.

When the desired field is reached (50 kilogauss, determined by ^2H resonance in ^2H_2O) sufficient time is allowed for the inductive voltage to decay to zero(several minutes) and the magnet is switched to persistent mode by closing the superconducting switches. The power supply is no longer necessary to maintain the field and it can be wound down. Because the power supply contains a resistor into which current from the solenoid can be dumped in the case of a quench, it is left connected to the magnet but with no current flowing.

3.2.6 Observations.

It has been found that trying to energize the solenoid to 50 kilogauss immediately after cooling with helium inevitably leads to trouble. The solenoid quenches quite erratically. The procedure adopted is to increase the field until a proton resonance is found at 30 MHz. The solenoid is then put into persistent mode and left for ~12 hours (usually overnight). After this the solenoid can be brought up to 50 kgauss (^{2}H resonance at 32.8 MHz) with very little likelihood of a quench.

The most probable reason for the increased stability after running at low field for 12 hours is that the entire coil has come to thermal equilibrium at 4.2°K. Since the transition temperature for Nb/Zr is ~11°K the heat conduction from the centre is reduced once the superconducting wire becomes superconducting (a superconductor is a thermal insulator). Thus it is very unlikely that immediately after cooling the innermost windings are as cold as the outer ones. This means that should a flux jump occur much less joule heat would be required to raise a section of the wire above its transition temperature and become resistive.

Having the coil running at low field may help to remove current loops (vortex currents, the collapse of which can cause joule heating) and establish current paths in the superconductor.

3.3 Initial difficulties.

3.3.1 The solenoid

The solenoid when first tested in this laboratory would not produce a field >25 kilogauss. It would quench at the same current, 10 amps, every time. The solenoid was unwound and the innermost section of wire was found charred in places. This damage must have occured when the magnet was quenched in its initial maximum field test at the Oxford Instrument Co., Ltd. Using new wire the solenoid was rewound by them. Initial tests showed it capable of producing 60 kilogauss. However, when installed the magnet quenched erratically between 20-40 kilogauss. It was not possible to attain a 50 kilogauss field. Once again the wire was removed. This time it was found that large sections of the copper sheath were not adhering to the superconductor core. This explained the erratic behaviour. The copper sheath, as mentioned previously, is essential to conduct heat away from the superconductor on the occurance of flux jumps and also to carry temporarily the current about a resistive spot in the wire.

Special lengths of new wire were selected by Supercon, the American manufacturers, who admitted they were having trouble producing the wire, and the magnet rewound for the second time.

A maximum field test was not performed this time. The solenoid was brought to 50 kilogauss and then run down without a quench. The

magnet is now being operated at 50 kilogauss and has been brought to 52.4 kgauss, but its critical field has not been determined.

3.3.2 The Dewar

The dewar in present use (described in Section 2.5) is the third that has been employed with the solenoid.

Mark 1.

This was of conventional design with a capacity of 2 litres above the magnet. To increase the room temperature working space the radiation shield was left out of the tail. This proved unwise because the radiation input at the tail induced oscillations in the helium and this increased the boil-off until it reached an unacceptable rate (Figure 3.2).

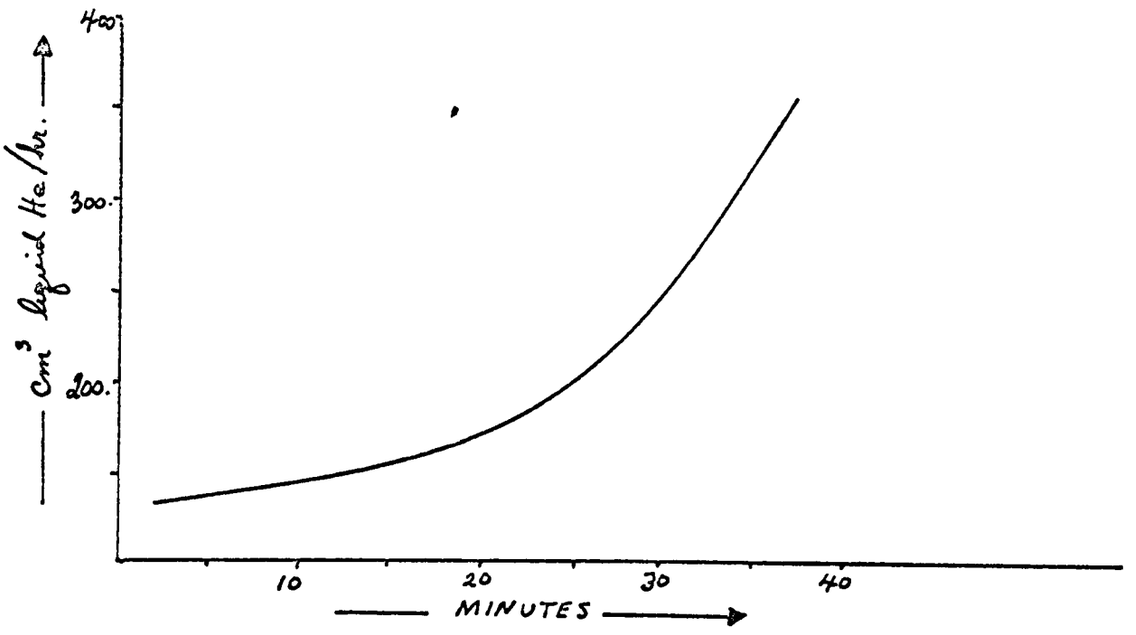


Figure 3.2 Instability in the helium boil-off rate from Mark 1 dewar.

With the inclusion of a radiation shield, narrowing the roomtemperature access to 7/8" from 1", the boil-off was reduced to < 200 cm^3 liquid helium/hour. This allowed about 10 hours operation. However, as was mentioned earlier, it was soon found that continuous operation was required and so a larger dewar was ordered.

Mark 11.

This dewar was similar to the present Mark 111. The major differences being that it was approximately six inches shorter, had a shorter but wider helium reservoir (all copper to the top of the reservoir) to hold 10 litres liquid helium, and a re-entrant section in the wall to provide an increase in the path length to the helium reservoir.

When tested it proved impossible to keep helium in this dewar. After filling, the boil-off rate would be reasonably constant for a few minutes, then it would start to increase rapidly. After a short time oscillations in the gas, so violent that they could be felt in the helium recovery line as beats, would boil off litres of liquid helium in a few minutes.

Studies of spontaneous oscillations occuring in gas columns (27) have been carried out, but all of these have been in tubes $\ll$6" diameter. The only advice people experienced in handling helium in large dewars could give was to fill most of the space above the reservoir with a bung, preferably of 'Styrofoam'. Experiments of this type were tried but no effective bung was found. The oscillations could be

damped for a few minutes but would build up again. The Oxford Instrument Co., Ltd., had built longer dewars with much narrower reservoirs than this that worked perfectly, so the oscillatory problem was connected in some way with the unusual shape of the helium can. Why this should cause such large oscillations to be formed is not readily understood.

Also, the attempt at increasing the path length in the dewar by using a re-entrant section in the wall proved abortive because the helium gas effectively shorted it out.

It was finally decided, after the loss of several months and many litres of liquid helium, to have a third dewar built, the present Mark 111.

3.4 Reducing the liquid helium boil-off.

The total liquid helium boil-off rate from the dewar is due to heat inputs from various sources: radiation, conduction along the walls of the dewar, magnet support system, and the various current leads.

These leads need to be as fine as is consistent with the maximum current they have to carry. By the use of minimum thickness leads, the rather large boil-off rate while the current is on is offset by the much reduced boil-off after all the power supplies have been shut off, and the coils are running in the persistent mode. To further reduce the heat input to the dewar the main current leads are made of superconducting wire from the top of the helium reservoir to the solenoid.

By reducing the size of the supplied leads the boil-off rate was lowered from $\sim$ 180 cm^3 liquid helium/hour. to $\leq$ 120 cm^3/hour. This

rate actually varies from $< 95 cm^3$/hour when the helium level is just above the magnet to $\sim 120 cm^3$/hour when the reservoir is full.

3.5 Field Homogeneity Tests.

Since the superconducting solenoid was a novel source of a magnetic field for nuclear magnetic resonance experiments it was necessary to fully assess its ability to produce a highly homogeneous H_o. The field values chosen for these tests were 7, 18, and 50 kilogauss, the respective resonance fields for ^1H, ^7Li, and ^2H at $\sim$30MHz.

3.5.1 Probe for Field Plotting.

To measure the field an n.m.r. single coil probe (Anderson Bridge, Figure 3.3) was used. To make the probe sensitive to small changes in position it was necessary to use a coil as small as possible, in this case ~ 0.05 cm^3. The maximum filling factor was obtained by sealing the ends of the coil with paper and coating the entire assembly with 'Durofix' adhesive. The sample was then injected into the coil and the small needle hole sealed.

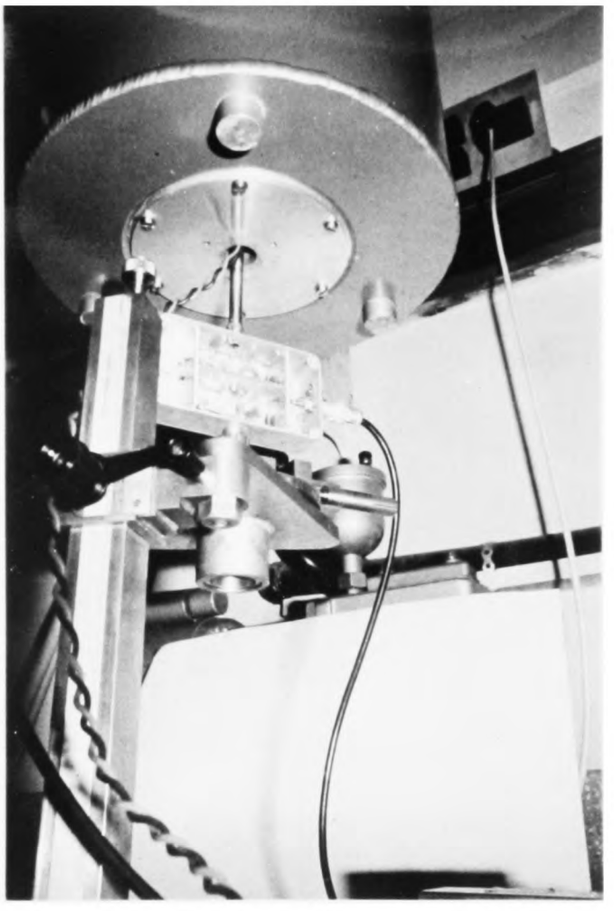
The samples used were:

H_2O - 0.01M $MnCl_2$

LiCl - Sat. sol.

^2H_2O - 0.01M $MnCl_2$

The probe was mounted on a modified cathetometer (Figure 3.3a) that permitted the probe to be offset and rotated to permit off-axis field measurements. To ensure coil alignment in the dewar tail a



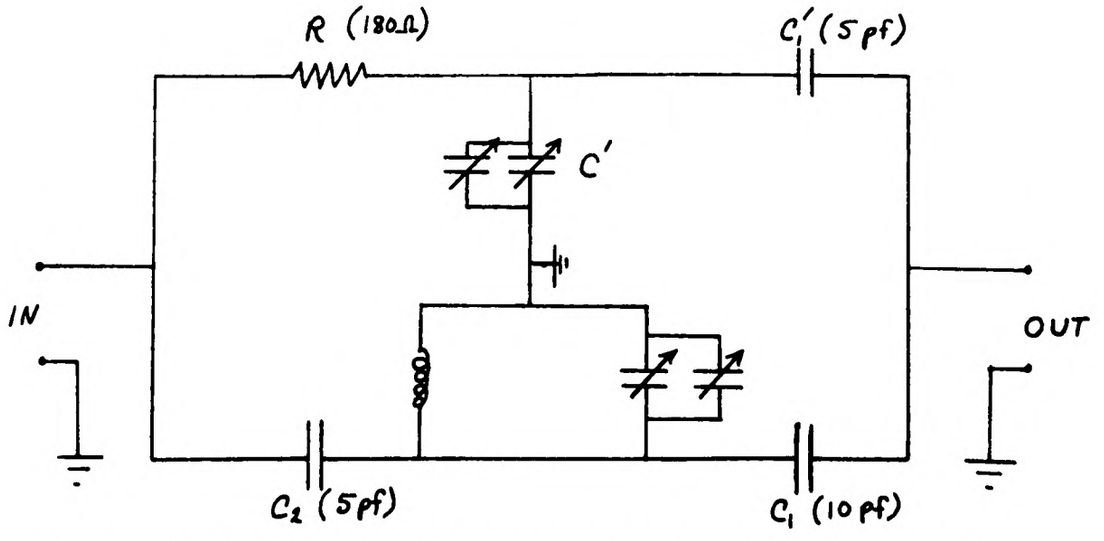


Figure 3.3 A) Anderson Bridge on cathetometer for field plotting experiments

B) Anderson Bridge circuit for 30 MHz operation

'Teflon' disc was fixed to the top of the probe head. This disc could be offset by the same amount as the probe. The sample height could be measured to 0.001 cm.

30 Hz modulation was employed and the n.m.r. signal from the probe fed via a diode detector and filter to the oscilloscope, the time base of which was derived from the modulation frequency. The resonance frequency was determined by adjusting the phase of the trace displayed on the oscilloscope to provide a cross-over point (Figure 3.4) and this was then centred on the oscilloscope by varying the frequency of the Schlumberger FS30 frequency synthesiser. Field measurements were made by measuring the change in resonance frequency of the sample. By this method changes of 1 in 10^6 were detectable under the most favourable conditions.

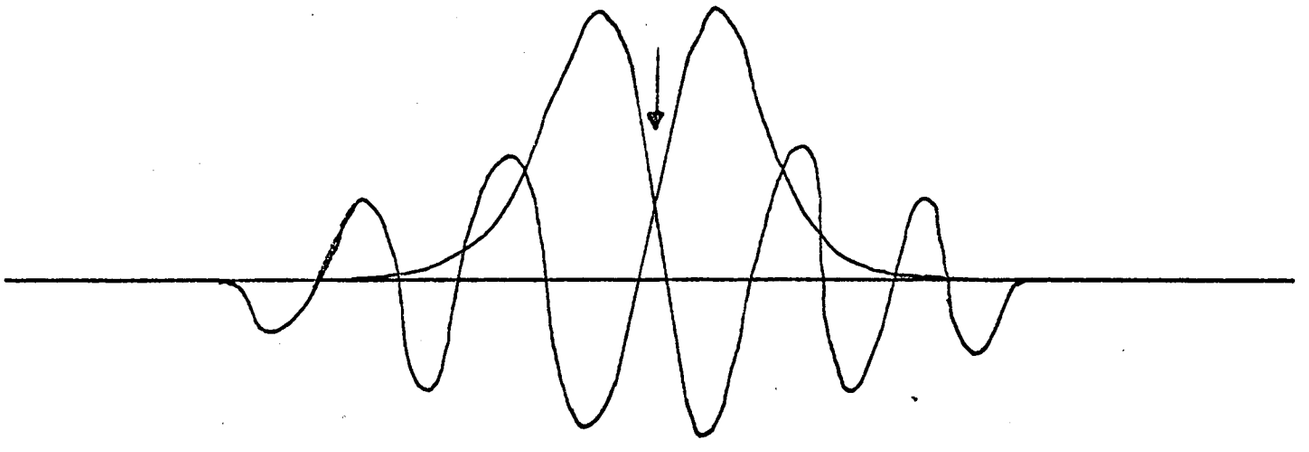


Figure 3.4 Oscilloscope trace observed with field plotting probe.

3.5.2 Remanent Fields.

It had been reported that strong remanent fields, $\leq$300 gauss, could be present in Nb/Zr solenoids (28). These are caused by vortex currents in the wire and are present even after the driving current has been reduced to zero. It was thought that the completely unpredictable distribution of these currents would make the attainment of a sufficiently high homogeneous field difficult.

Tests were carried out to determine the effect of remanent fields in our solenoid.

An ^{1}H resonance was located at $\sim$36MHz. The current to the solenoid was then varied about this point and the effect on the homogeneity of the field noted as the sample went back and forth through resonance. The resonance line was broadened and the point of best homogeneity varied, indicating changes in the field profile. Thus remanent fields were present.

To see if these fields could be removed without raising the magnet above its transition temperature, 'cycling' was attempted. The resonance was located and the point of best homogeneity found. The current was reduced to zero and the polarity of the current leads changed. The current was then brought to the same value as before. This procedure was repeated several times and each time a different field was obtained (Table 3.1). This indicated remanent fields of $\sim$283 gauss (difference between maximum and minimum resonance frequencies in table).

At high fields this effect is less serious, the percentage of the total field due to remanent fields being small.

To minimize remanent field effects the solenoid is energized slowly and when the desired field is reached the main coil is put into the persistent mode. The current is not varied about this point to obtain an exact field. Using this method the reproducibility of the field is within ~.03%.

Table 3.1

Effect of cycling solenoid

Lead Connections	Current (Measured as voltage drop across series resistor)	Frequency	Position	Comments
+	26.689mV	35.8610MHz	12.735cm.	Best homogenity
-	26.689	34.730	12.735	Poor "
			13.022	Best "
+	26.689	35.412	13.022	Poor "
			12.585	Best "
-	26.689	35.046	12.585	Poor "
			12.753	Best "

3.5.3 Field profiles.

After these initial remanent field tests the field profiles for the solenoid at 7, 18, and 50 kilogauss were determined. The axial field homogeneity was measured by raising the probe in small increments and determining the change in resonance frequency of the sample, as previously described.

Typical axial field plots, with the currents in the main and end coils equal, are shown in figure 3.5. The homogeneity improves at each of the turnover points 1, 2, 3 in the graph.

Radial field profiles, although extensively made, are not shown here. Actual gradients across the axis are quoted but the profiles can be misleading since the room temperature insert is not necessarily centred in the bore of the solenoid.

Extensive tests were made to obtain the best homogeneity at 50 kilogauss. All three turnover points were investigated. The experiments were carried out by varying the currents in the end coils with the main coil in the persistent mode.

The effect of lowering the currents in the end coils is illustrated in figure 3.6. This had the effect of improving the homogeneity at point 1, figure 3.5. However, the best axial homogeneity attained, several parts in 10^5 over 1 cm., was not sufficient for our purposes.

Very little improvement at the magnetic centre was possible. Measured radial gradients here were as high as 5 gauss across the room temperature gap.

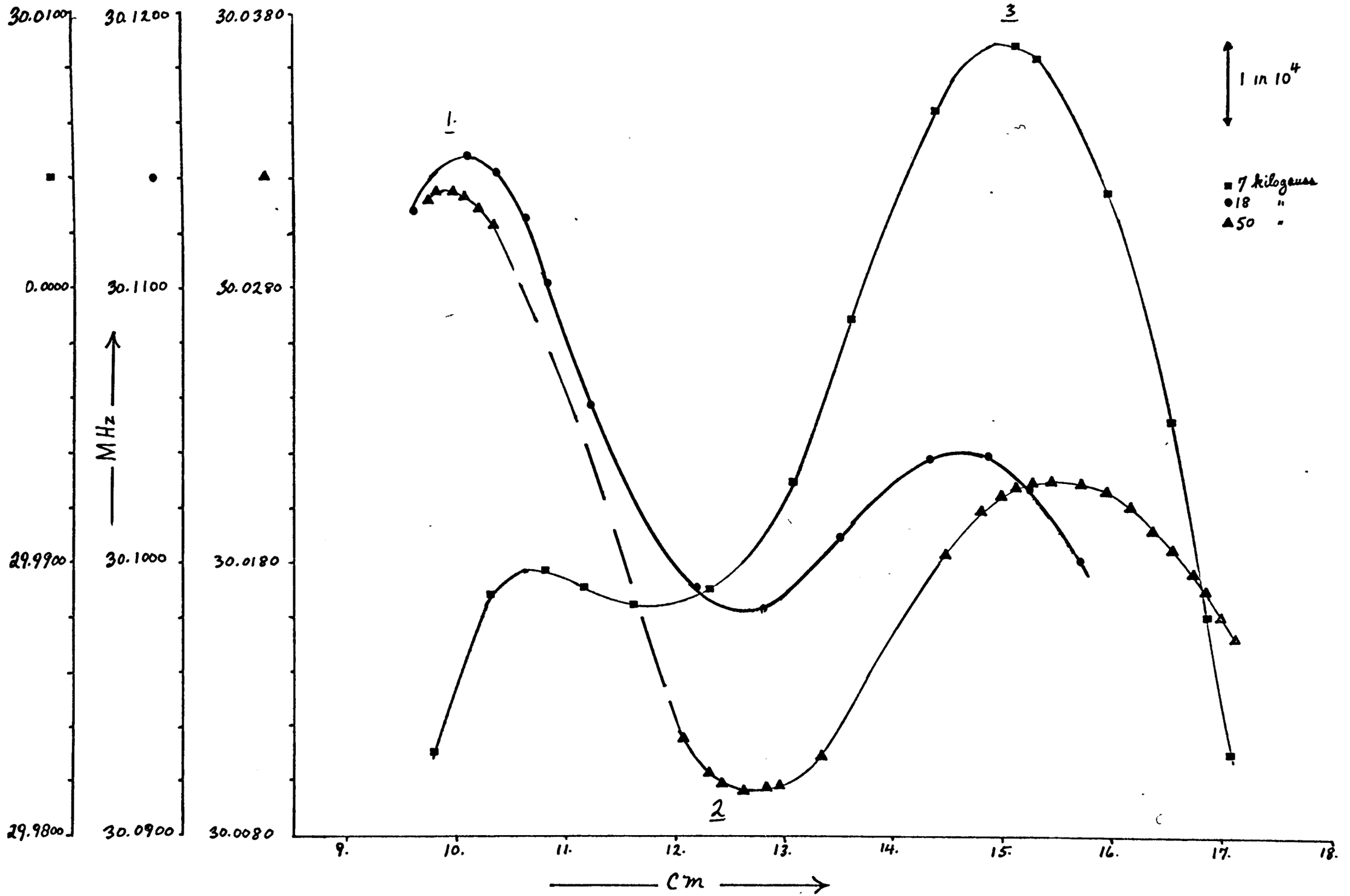


Figure 3.5 Typical axial field plots for 7, 18, and 50 kilogauss

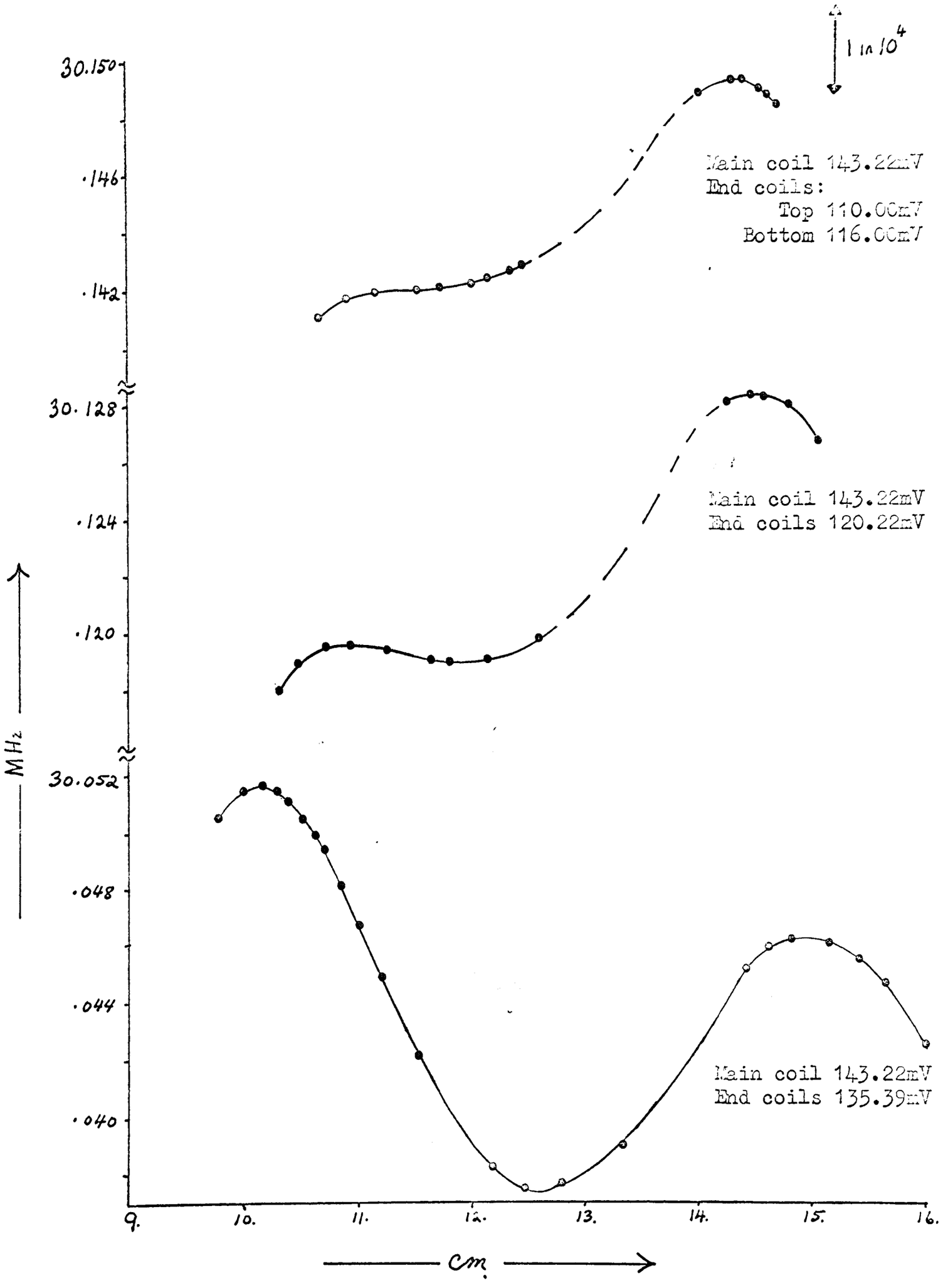


Figure 3.6 Effect of lowering the current in the end coils.

By increasing the currents in the end coils it was possible to improve the homogeneity at point 3, figure 3.5 to > 1 in 10^5 over 1 cm. axially and about 1 in 10^5 radially. These experiments are shown in figure 3.7. Although this position provided the best homogeneity it was still not really suitable for our n.m.r. experiments.

It was hoped that the homogeneity at the magnetic centre of the solenoid could be improved by moving the end correcting coils. To determine the distance these coils should be moved, the field profiles of the main coil and the end coils were needed.

The arrangement of the current leads prevented the energizing of the main coil independently of the end coils. If the two end coils were placed in the persistent mode at zero current, transformer coupling (50,000 : 700) would have induced large currents in them when the main coil was energized. The procedure adopted was to take all three coils to the current needed for 50 kilogauss ($\sim$ 20 amps), put the main coil into the persistent mode, and then reduce the currents in the end coils. This increased the field in the main coil, but only by a few per cent.

The homogeneity of the uncompensated solenoid was not good, so the field could be plotted over only a short distance (figure 3.8a). Subtracting this profile from that of the three coils gave the field produced by the end coils (figure 3.8b). This showed that the end coils were not positioned on the magnetic centre of the solenoid.

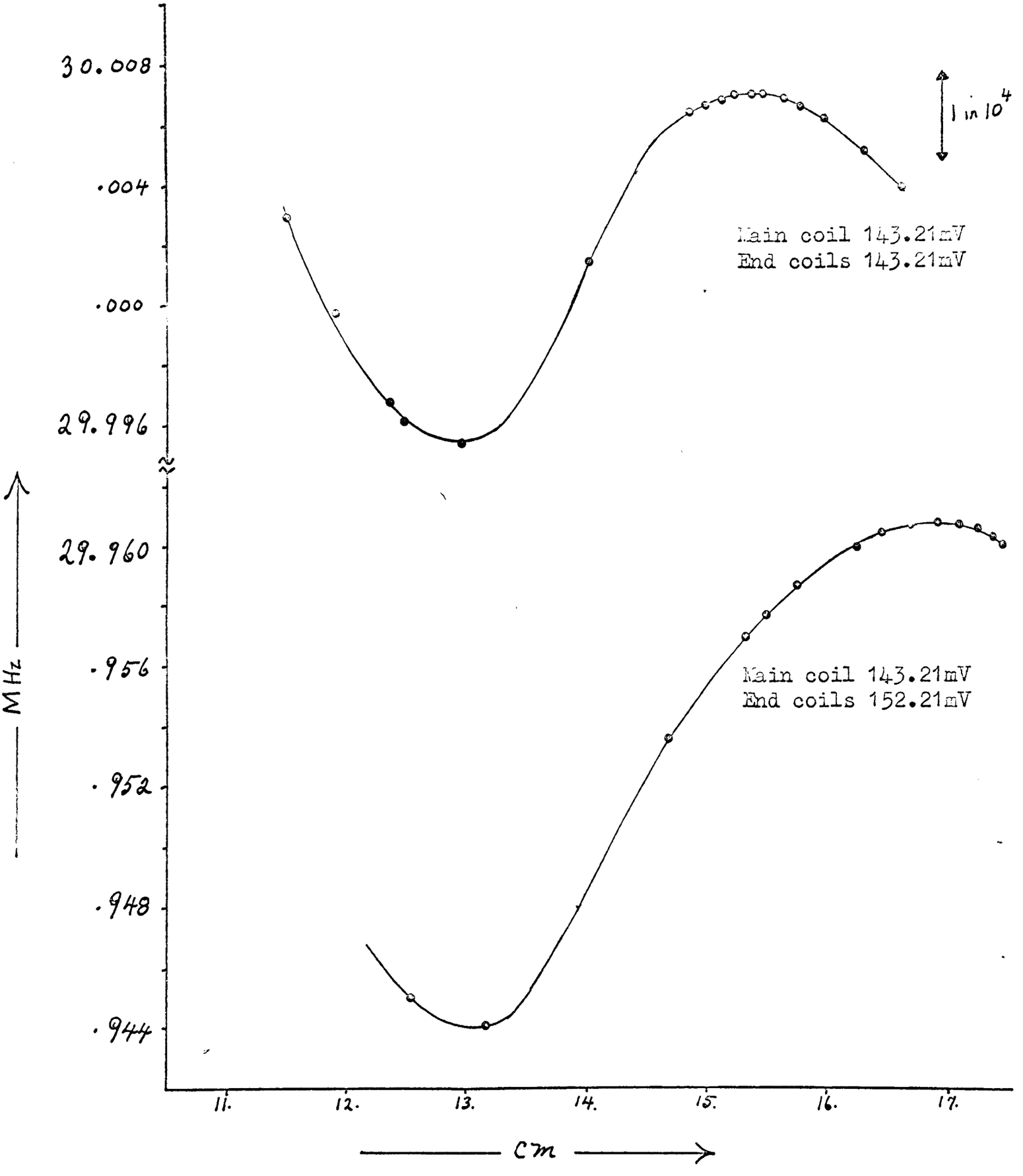


Figure 3.7 Effect of raising the current in the end coils.

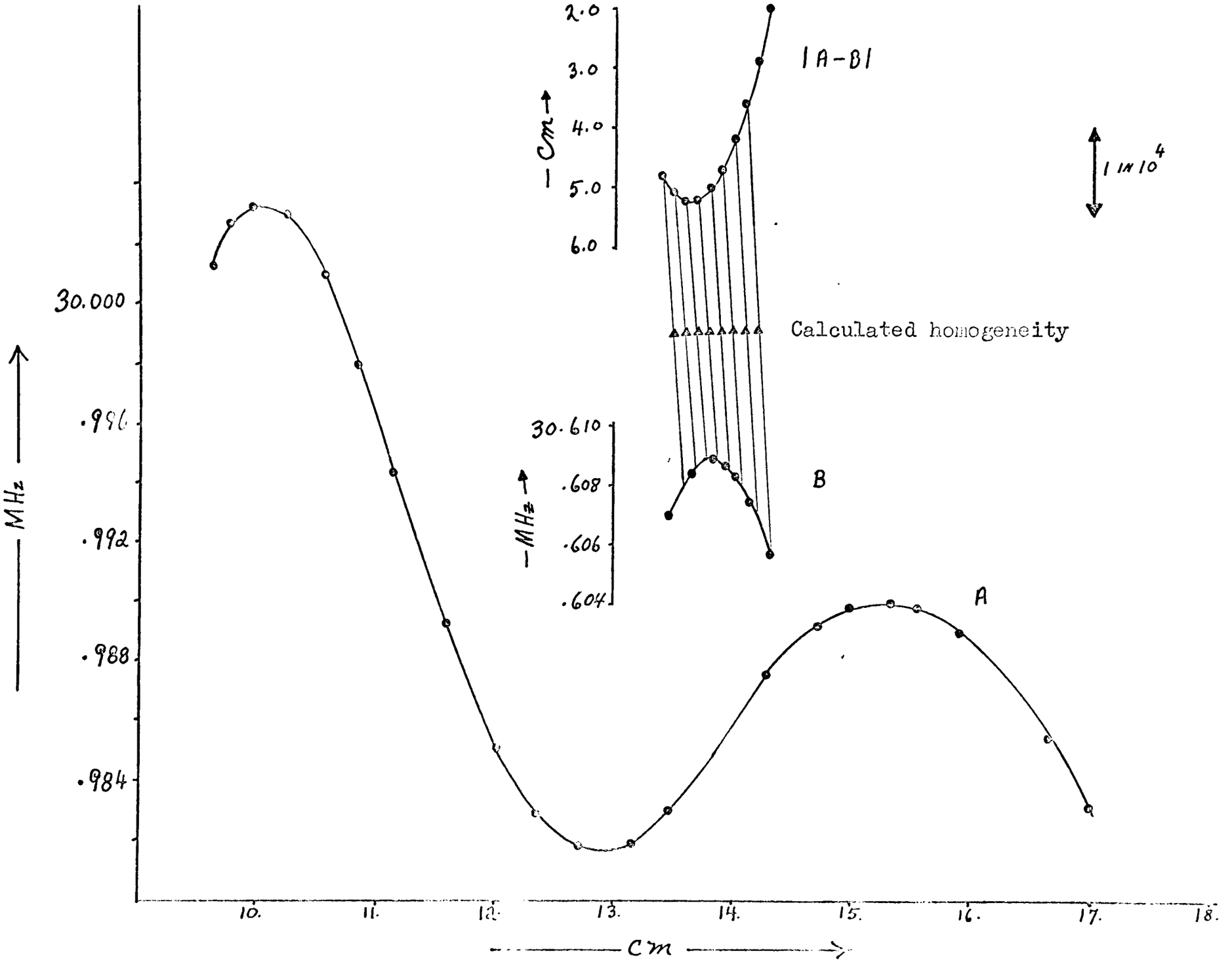


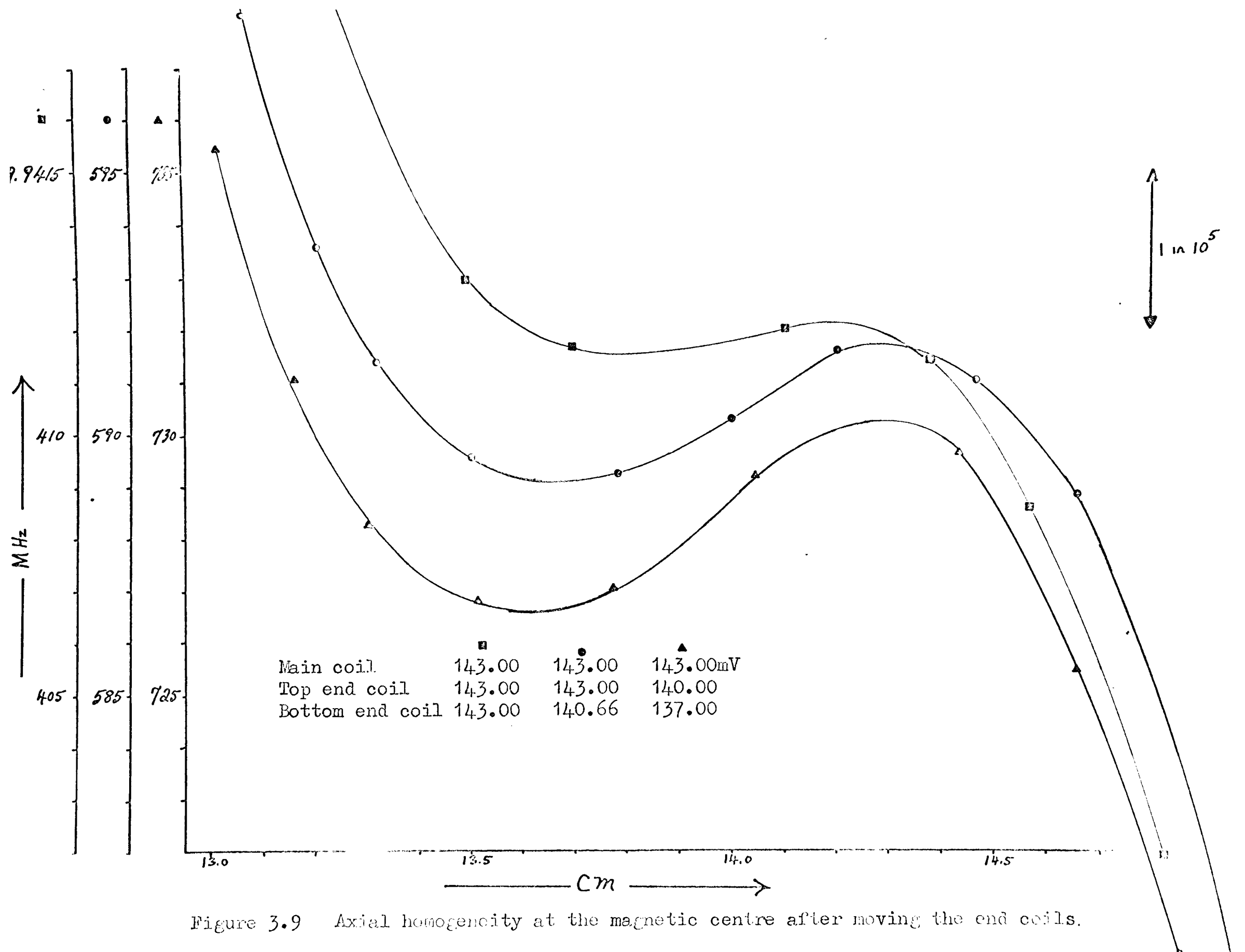
Figure 3.8 Calculated homogeneity attainable by moving end coils

Movement of the end coils, as indicated in figure 3.8c, showed that a reasonably flat region at the magnetic centre was possible. This was done and the region at the magnetic centre was flattened as predicted (Figure 3.9). However, while the axial homogeneity had been improved over the calculated distance, no appreciable improvement had been made to the radial gradients. A sharp fall-off in the axial homogenaity had also been introduced outside the calculated distance along the axis. The overall homogeneity over a large sample was very bad and no juggling of the currents in the end coils could improve this significantly.

After these measurements were made it was decided to try to improve the homogeneity at the upper turn over point (Figure 3.5, point 3). Fortunately the movement of the end coils had reduced the inhomogeneities here. Through judicious manipulation of the currents in the end coils an axial homogeneity of 1 in 10^6 over 0.5 cm. and radial gradients of approximately 3 in 10^6 were obtained (Figure 3.10).

Because of initial field drift, the homogeneity changes after a few days (Figure 3.11) and the end coils have to be readjusted. No change in the homogeneity is detectable after this.

The next stage in the improvement of the homogeneity is through the use of field gradient cancelling coils. A preliminary experiment was done employing a pair of opposed Helmholtz coils to apply a linear gradient along the z axis. With these an axial homogeneity of approximately 1 in 10^6 was achieved over a distance of 1.2 cm. (Figure 3.12).



	■	●	▲
Main coil	143.00	143.00	143.00mV
Top end coil	143.00	143.00	140.00
Bottom end coil	143.00	140.66	137.00

Figure 3.9 Axial homogeneity at the magnetic centre after moving the end coils.

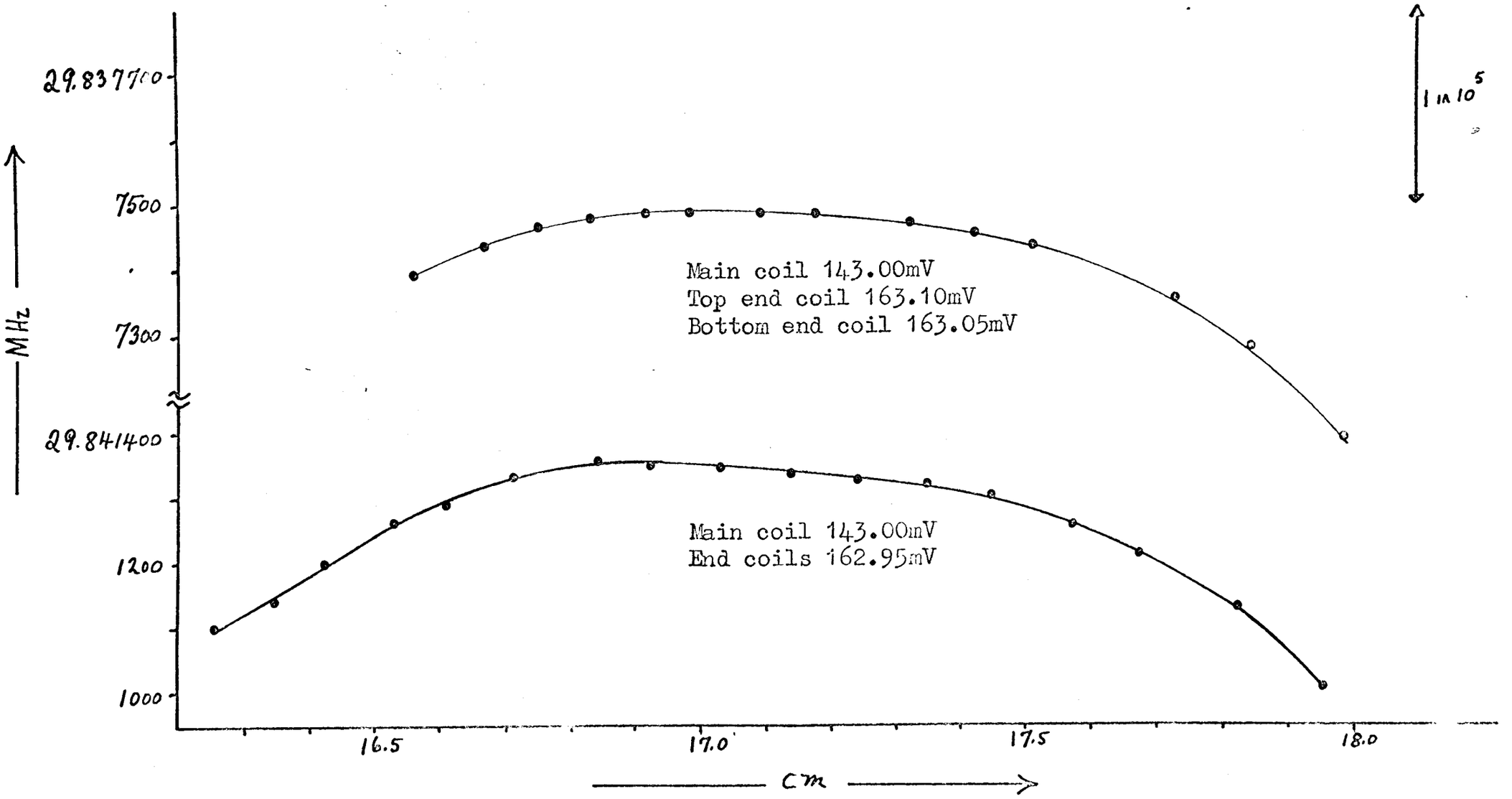


Figure 3.10 The best homogeneity attained after the end coils were moved.

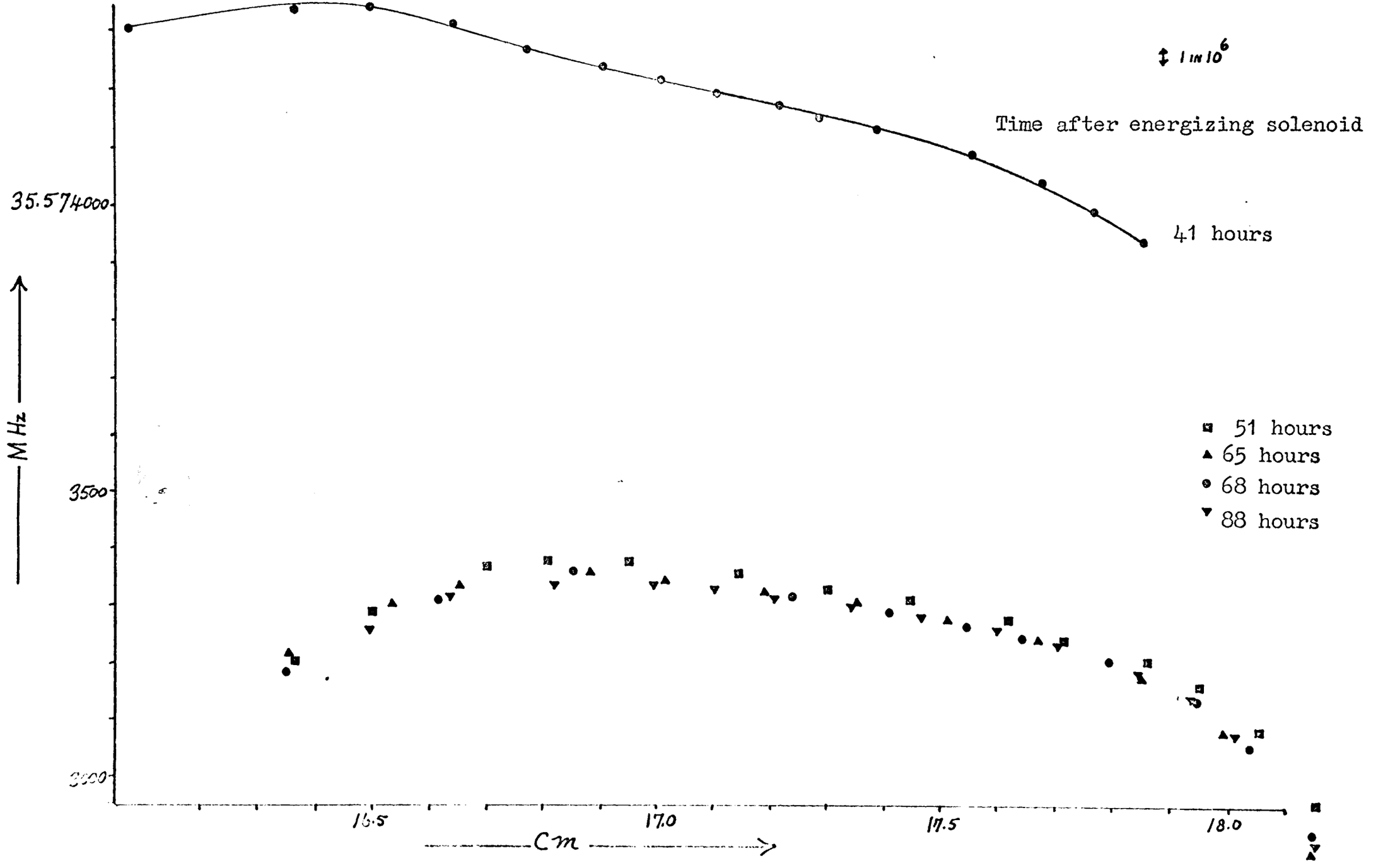


Figure 3.11 Change in homogeneity caused by initial field drift

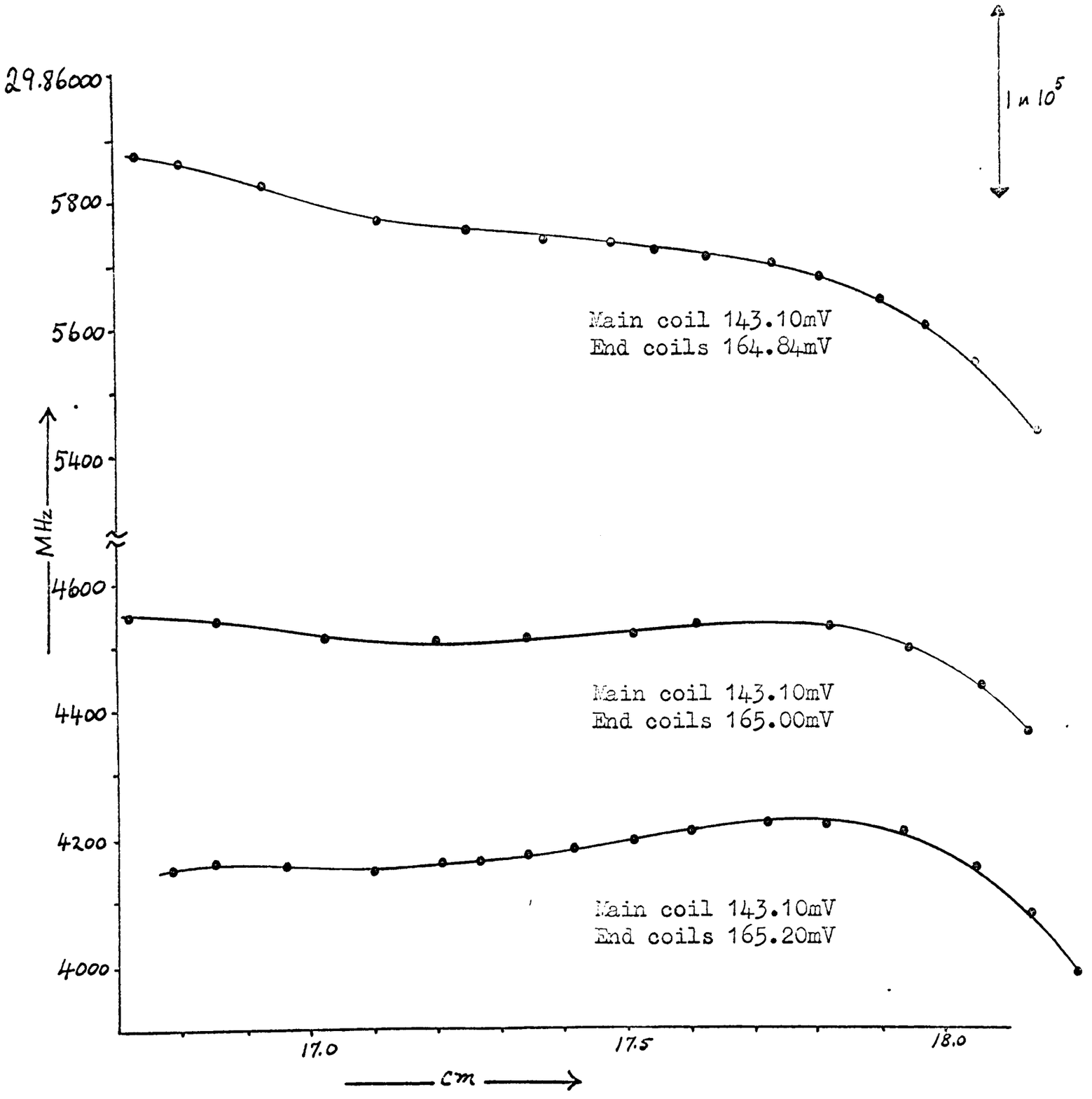


Figure 3.12 Homogeneity attained with the aid of a supplementary Z gradient coil

3.6 Homogeneity Improvement with Gradient Cancelling Coils.

3.6.1 Superconducting gradient cancelling coils.

Although the solenoid is theoretically corrected to sixth order, gradients of all orders and degree, both zonal and tesseral, are present due to winding imperfections, distortions from interleaving materials, etc. The large radial gradient at the centre is probably caused by a small distortion of the main solenoid toward barrel shape. This may be due to thefact that the ends of the copper former were annealed when its flanges were hard soldered in place.

M. Golay (29) has produced designs for a set of orthogonal gradient cancelling coils. These are based on the fact that an inhomogeneity at a point in the magnetic field can be expressed as the sum of incremental fields at the point, each of which is representable by a spherical harmonic. These coils are each designed to produce a particular spherical harmonic of degree and order and thus are essentially orthogonal.

The first four of these coils, producing linear gradients in the x, y plane and linear and quadratic gradients along the z axis (in M. Golay's terminology 21, 21′, 20, 30) have been manufactured from superconducting wire and are mounted on a thin stainless steel cylinder surrounding the magnet (Figure 2.5c). Each coil has 23 turns. To prevent multiple crossovers M. Golay's design for the 21, 21′ coils has been modified as shown in figure 3.13. These coils produce the same gradients as the original design (Figure 3.14).

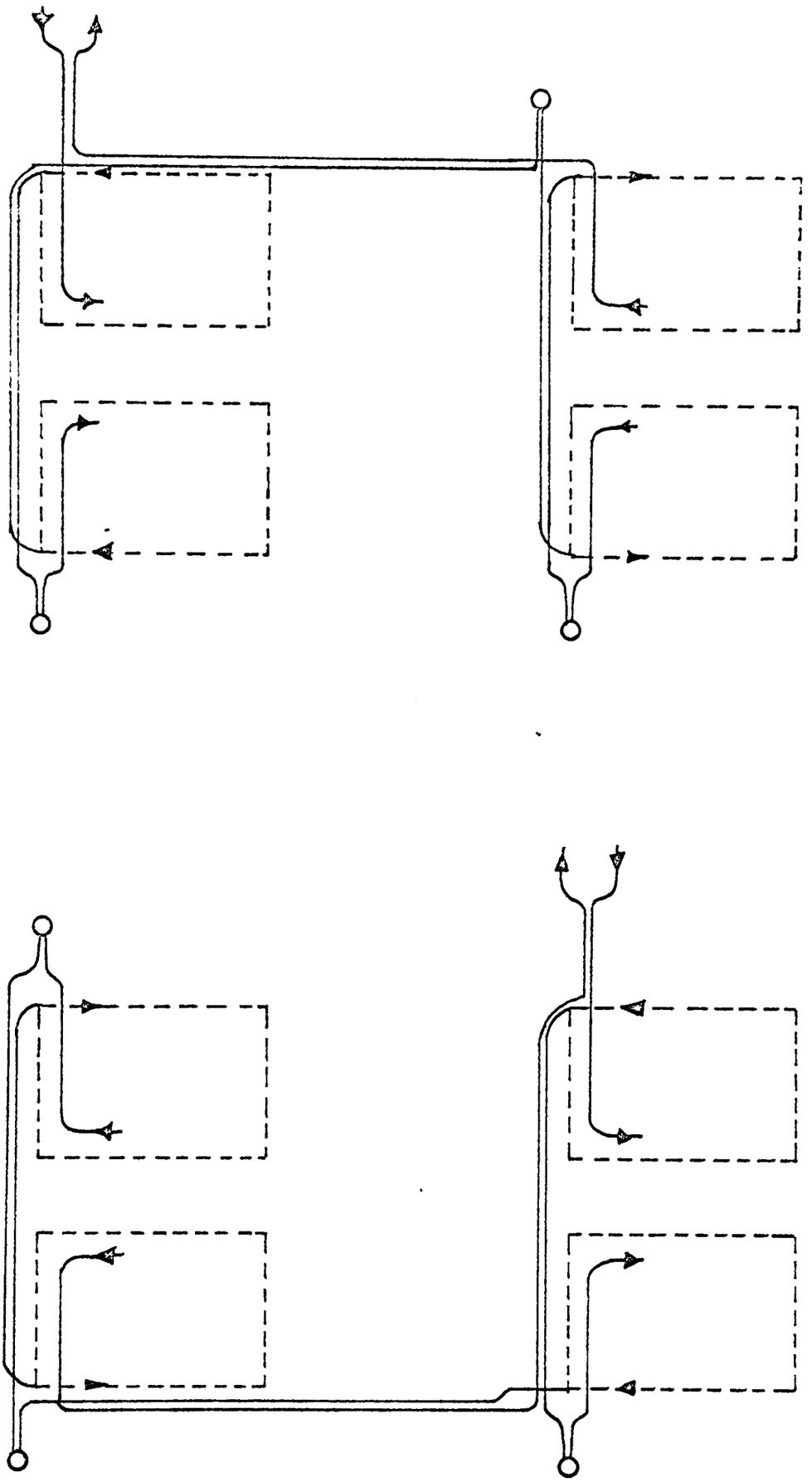
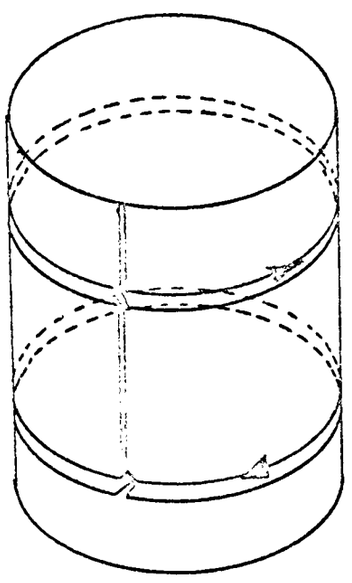
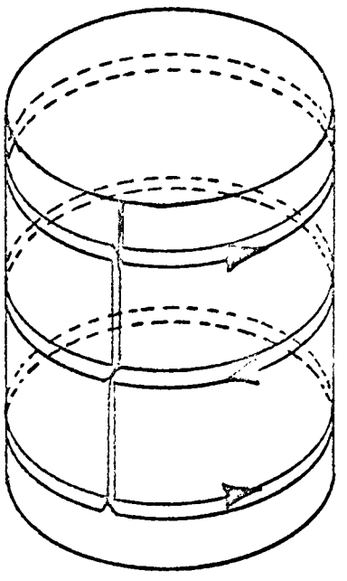


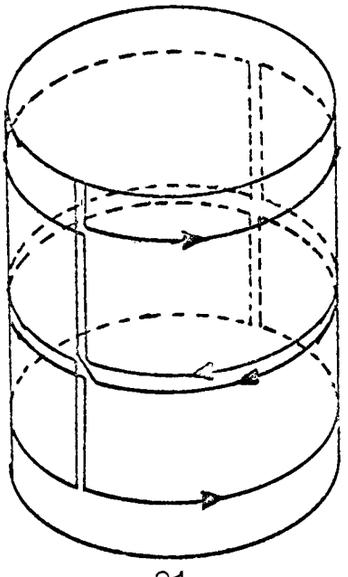
Figure 3.13 Diagram of the '21' superconducting Golay correcting coils. Each coil has 23 turns.



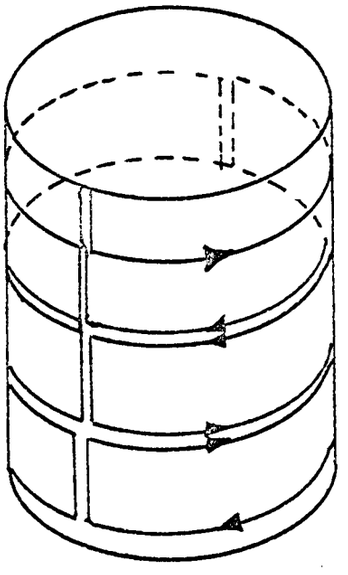
20



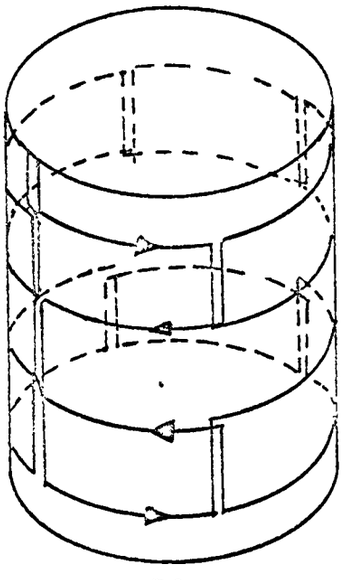
30



21



31



32

Figure 3.14 Field gradient cancelling coils, designed by Golay.

With the incorporation of these Golay correcting coils the small sample field plotting probe was abandoned and a probe capable of using 10 mm diameter tubes constructed (described in section 4.3). It was easier to detect small changes in homogeneity by observing the linewidth of the larger sample.

3.6.2. Room temperature gradient cancelling coils.

The superconducting correcting coils allowed sufficient improvement in the magnet homogeneity to make a further set of eight room temperature coils wound on the probe effective. These Golay correcting coils include the 20, 21, 21', 30 coils as well as 31, 31', 32 and 32' coils. They are wound on a 'Perspex' former that fits on to the probe. They are illustrated schematically in figure 3.14 and figure 3.15 is a photograph of a complete set ready to be mounted on a probe.

These coils are designed to correct at the centre only. Consequently the room temperature coils cannot correct completely over a sample of 1 cm^3 and so there are rather large wings on resonance lines of nuclei that have line widths smaller than the magnet inhomogeneity.

The magnet homogeneity over a 9 mm diameter sphere is shown in figure 3.16. The continuous line is a computer calculated Lorentzian line of the same line width at half height, 6 Hz at 28.013 MHz, as the experimental curve.

All the correcting coils are adjusted to give the maximum

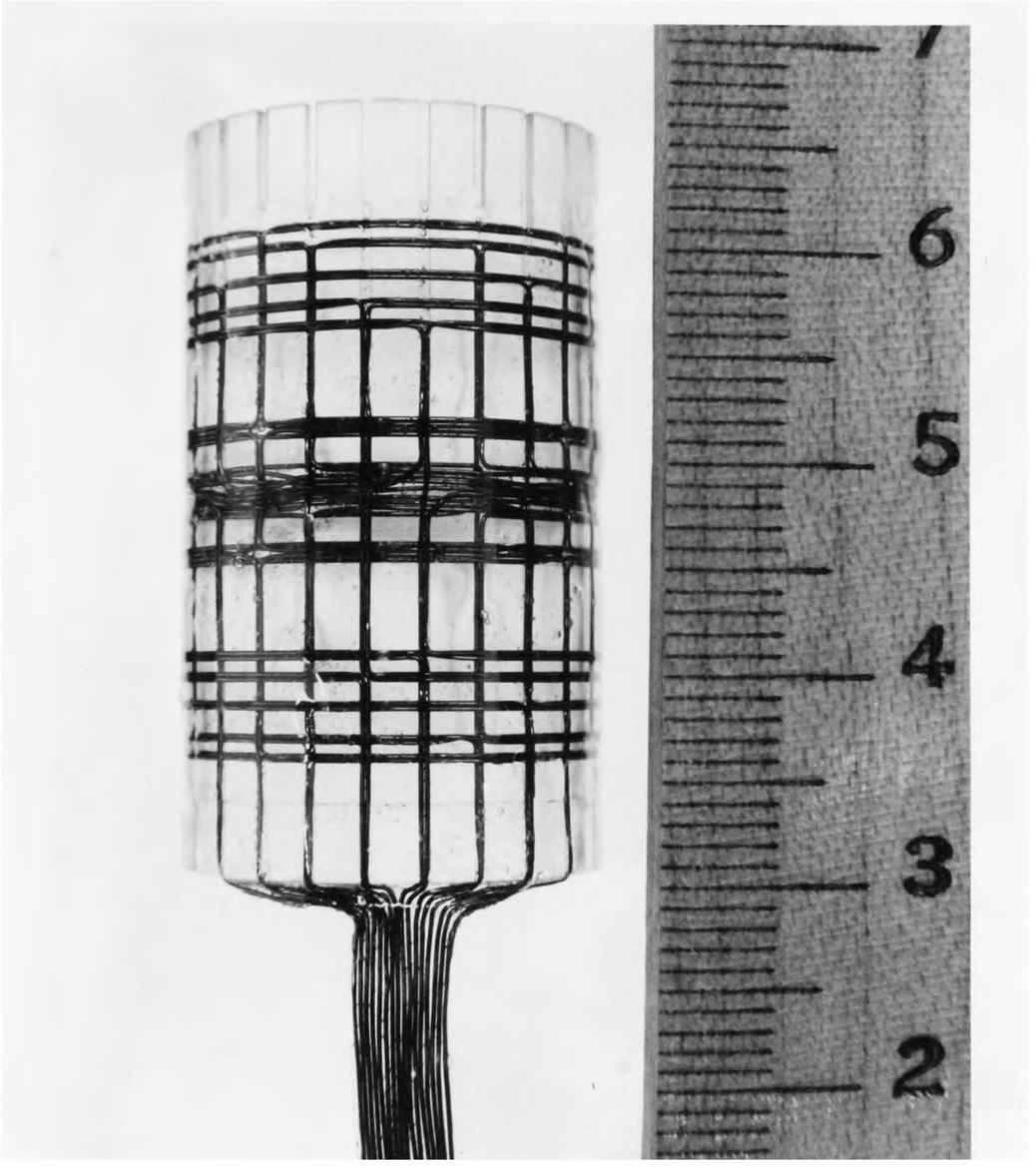


Figure 3.15 Photograph of complete Golay correcting coil set wound on a 'Perspex' former for use on the probe.

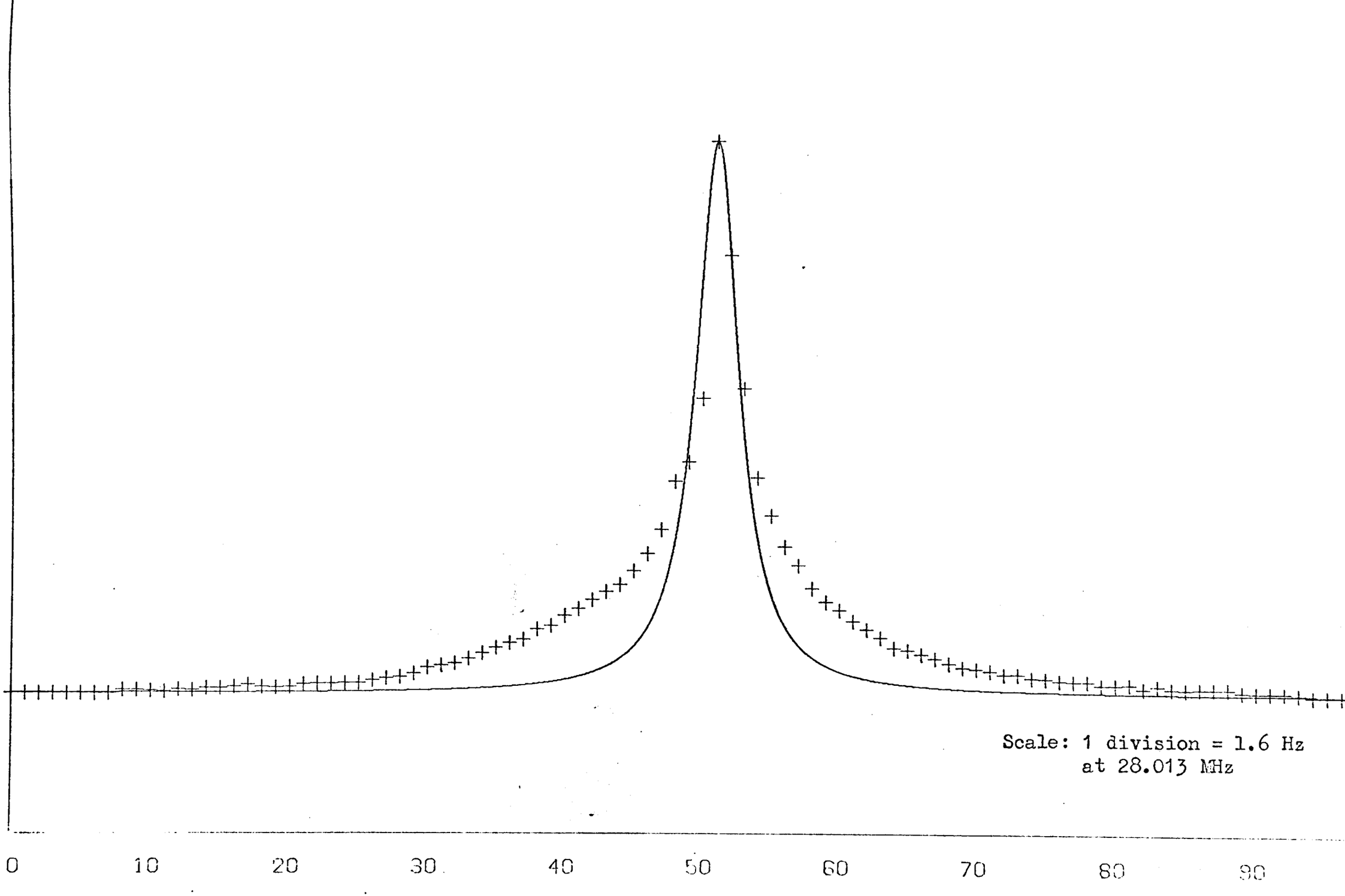


Figure 3.16 Illustration of the magnet homogeneity over a 9mm diameter spherical sample.

homogeneity by observing a strong narrow resonance on the oscilloscope. Golay correcting coils are adjusted to give the best signal with the probe coils off. After the superconducting coils are switched to the persistent mode the probe correcting coils are adjusted.

Once set in the persistent mode the superconducting Golay correcting coils need not be adjusted again. Small changes in homogeneity are corrected with the probe coils.

A current of up to $2\frac{1}{2}$ amps (at 6 volts) may be used in each Golay correcting coil, both superconducting and probe. The driving circuit is shown in figure 3.17. To avoid fluctuations in the coils' corrections stabilized 6 volt power supplies are used.

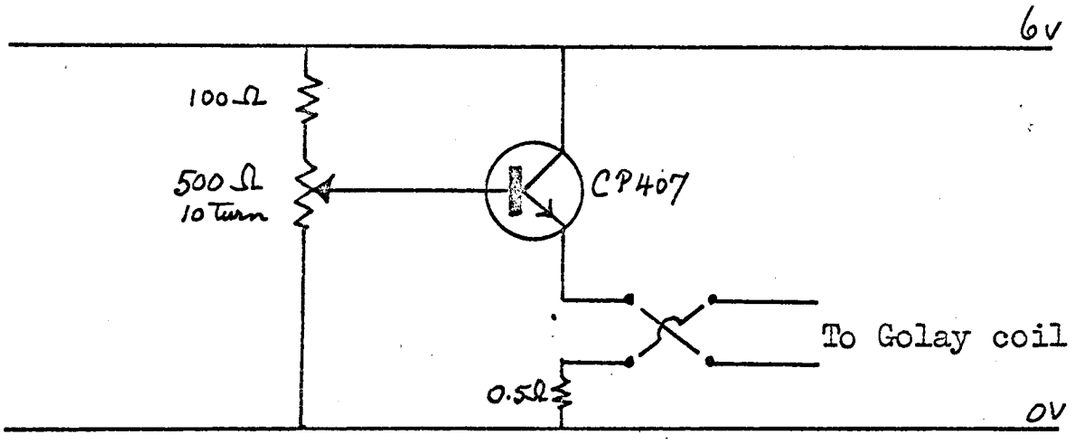


Figure 3.17 Driving circuit for Golay coils.

It should be noted that the homogeneity along the z axis, is sufficiently good to make spinning a possibility for improvement of the homogeneity of the solenoid.

Sample spinning has not been attempted, though should proton resonance investigations be contemplated, the construction of a spinning assembly would be mandatory.

Chapter 4. The Spectrometer.

4.1 Introduction.

The spectrometer to be described is capable of measuring nuclear resonances of a very wide range of nuclei (excluding ^{1}H, ^{19}F) with considerable precision. To take full advantage of the remarkable stability of the superconducting magnet operating in the persistent mode, frequency sweep is provided. Provision is made to be able to sweep over any frequency from 10 to 100 MHz in crystal locked steps as small as 1 Hz.

The spectrometer is assembled mainly from commercially available components.

The block diagram of the spectrometer is shown in figure 4.1 and figure 4.2 is a photograph of the complete spectrometer.

4.2 Description.

The r.f. source is a Schlumberger FSX3005 frequency synthesiser which has been provided with remote switching capability in crystal locked steps down to 1 Hz. The minimum switching time is 200 msec.

The programming unit which was built in this laboratory by Dr. H.D.W. Hill operates digitally from a clock frequency. The unit can be programmed to scan the synthesiser over any selected frequency range (up to four decades) in preselected steps at speeds from the fastest 0.5 sec./step to the slowest 128 sec./step. Frequency increments are selected in the series 1, 2, 4, 5 from any one of the

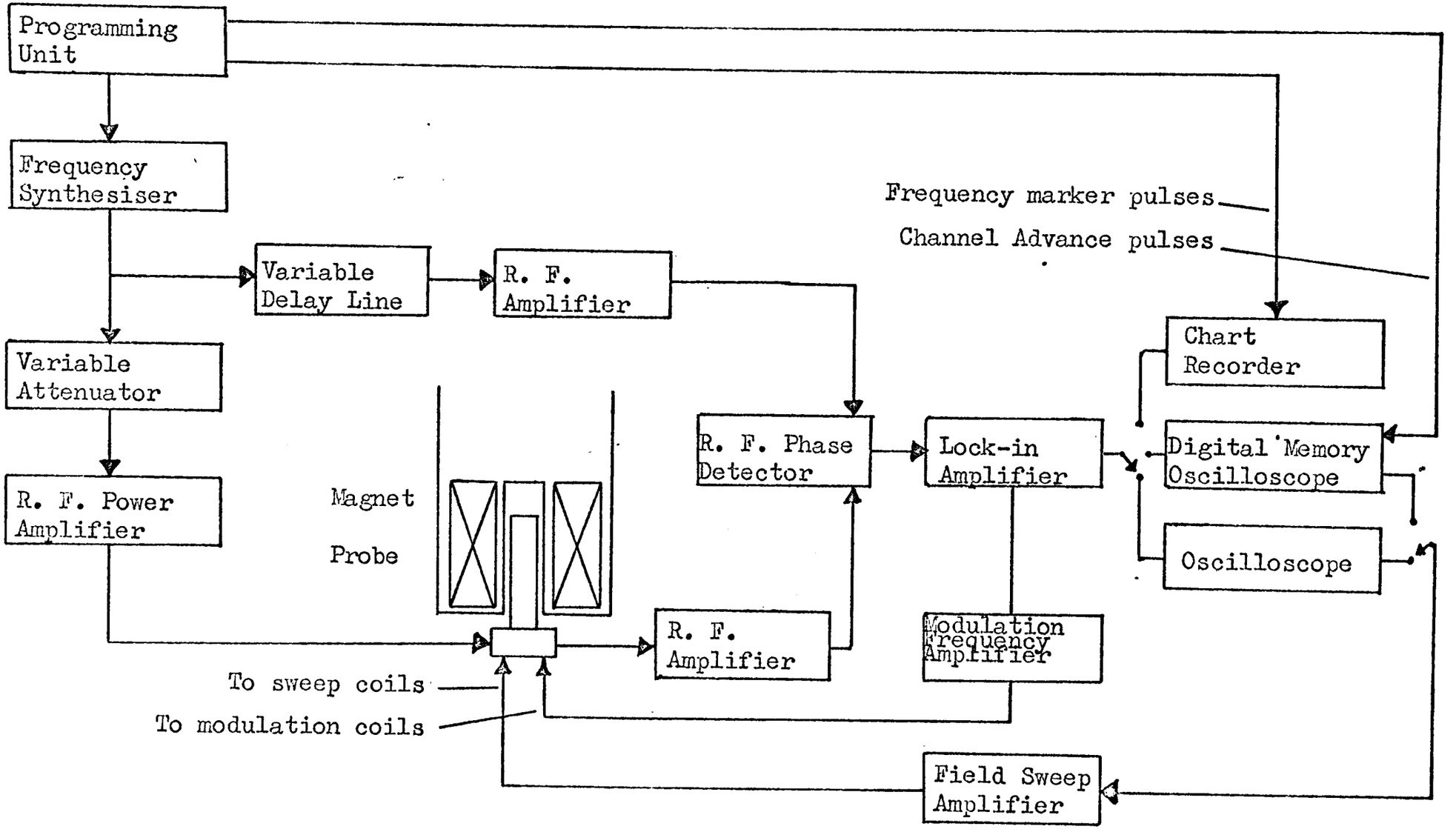
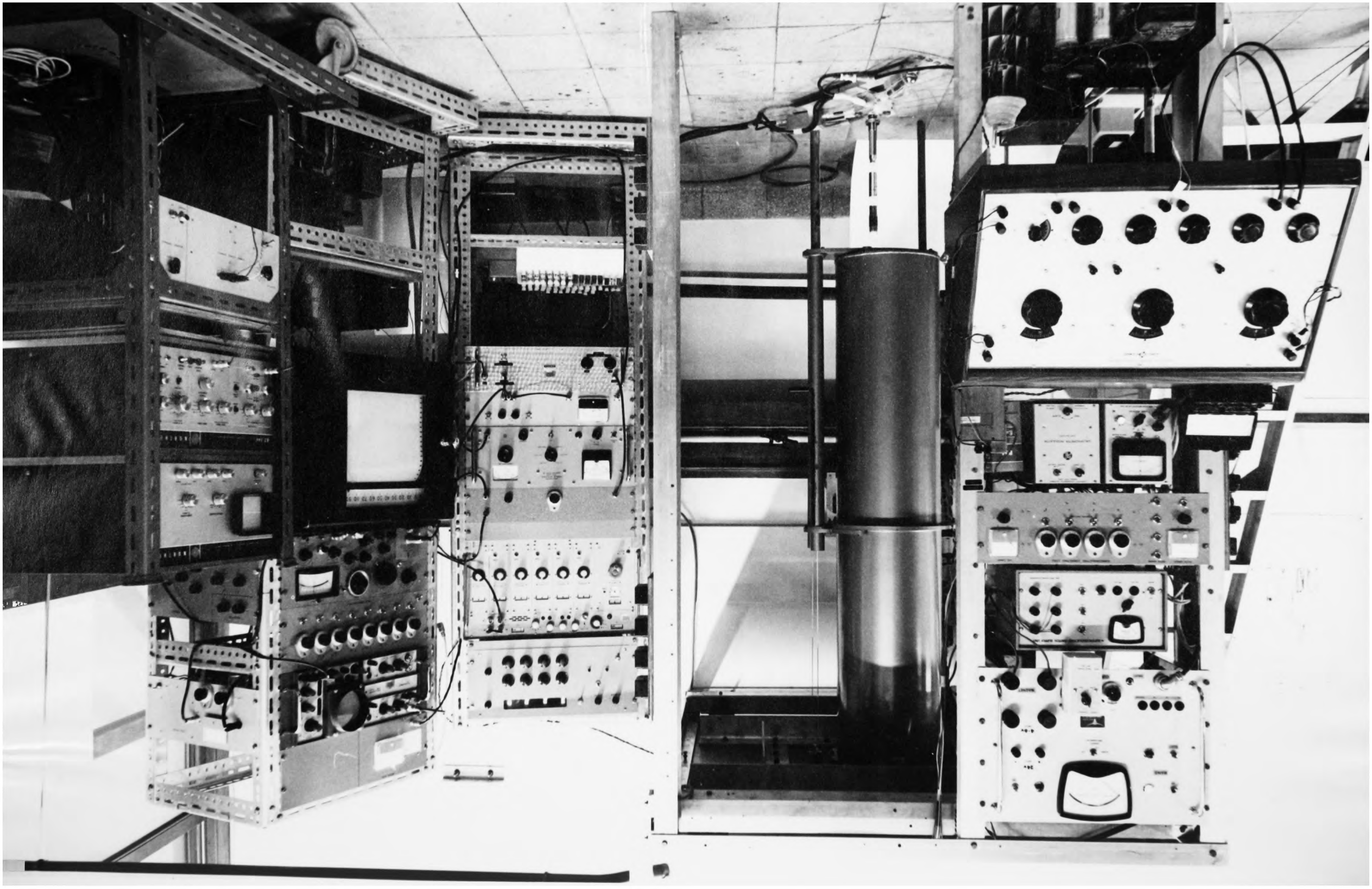


Figure 4.1 Block diagram of spectrometer.



1, 10, 100 Hz decades.

The programming unit also provides pulses to frequency calibrate the recorded spectra and to address the digital memory oscilloscope so that each channel corresponds to a precise frequency.

The output from the frequency synthesiser can be amplified up to five watts when necessary to achieve a large H_1 field in the probe by a Boonton 230A Signal Generator Power amplifier. This power amplifier has no gain control so its output is controlled by an attenuator in the output of the frequency synthesiser. This is made from a Hatfield MD3 balanced modulator.

The signal from the probe, described in Section 4.3, is amplified with a transistorized r.f. amplifier (Decca Radar Ltd.). There are 6 of these amplifiers to cover the frequency range from 10 to 100 MHz.

Centre frequency	Band Width to - 3db.	Max. gain
12	7 MHz	58db
20	14 MHz	56db
30	15 MHz	56db
40	14 MHz	52db
60	30 MHz	48db
80	25 MHz	39db

The pre-amplifiers are mounted next to the probe under the magnet. This enables a short coaxial cable to be used from the receiving coil,

thus keeping the noise figure for the pre-amplifiers to a minimum, $\lesssim$ 3db. The stray field from the nagnet at this point is $\sim$ 500 gauss and does not seem to affect the performance of the pre-amplifiers.

The amplified signal is r.f. phase detected in a wide band balanced modulator (Hatfield Instruments, MD4, 0.5 to 300 MHz). The reference frequency is derived from the synthesiser, and passed through a variable delay line and amplifier to provide an r.f. phase shift.

The output from the r.f. phase detector is passed to an audio amplifier and phase detector (Princeton Applied Research, HR-8) which also provides the audio frequency for the field modulating coils on the probe. This frequency is amplified with a Quad Mark 11 power amplifier.

The output from the HR-8 can be fed to an oscilloscope, to a chart recorder (AEI), or to a digital memory oscilloscope (Northern Scientific NS544, 1024 channels) for accumulation of repetitive scans. Other components of the spectrometer are: Field Sweep Unit (Figure 4.3).

A small field sweep (0.5 to 2.5 gauss) can be applied from a coil wound on the probe head. The sweep is derived from the time base of the Telequipment D43R oscilloscope built into the spectrometer.

The field sweep is normally only used to facilitate setting up the spectrometer since the spectra obtained do not have the precise calibration of those obtained by frequency sweeping. The sweep can be quite fast and allows display of the resonance on the oscilloscope,

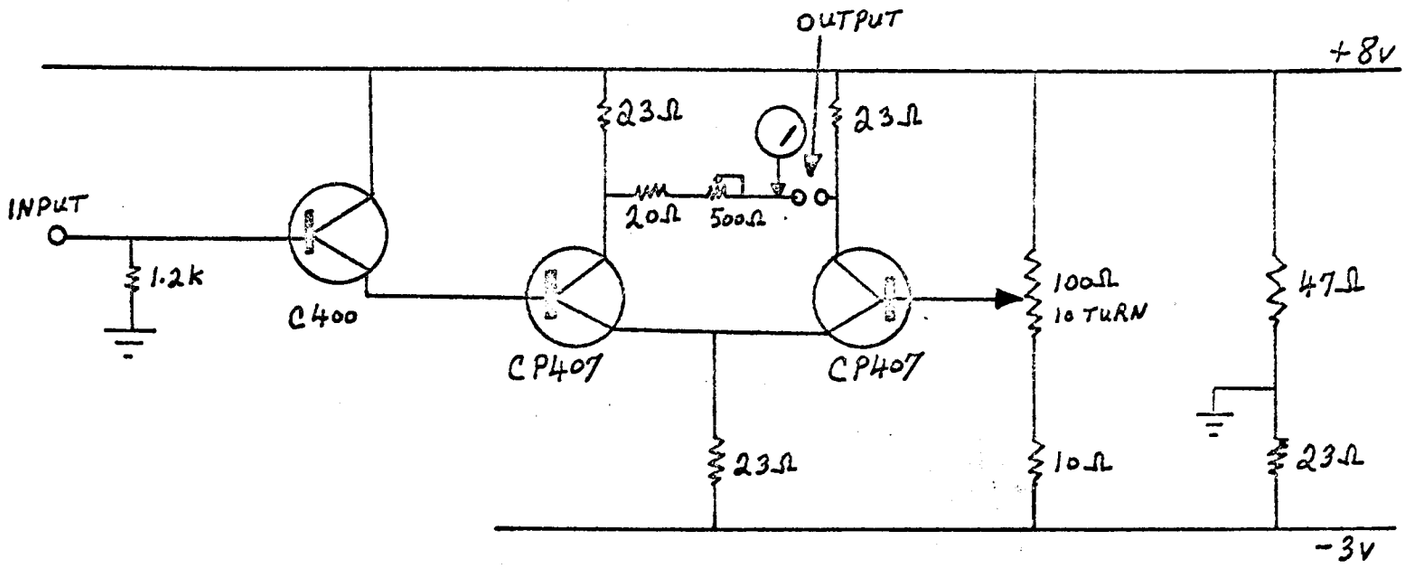


Figure 4.3 Field Sweep Unit.

whereas the frequency sweep is limited by the rather long switching time of the synthesiser.

Recorder Interface (Figure 4.4).

This includes the controlsfor the frequency calibration marks, recorder off-set, and signal potential divider for the outputs of the HR-8 lock-in amplifier and the digital memory oscilloscope to the recorder.

The spectra are calibrated by taking pulses from the programming unit after every 5, 10, 50, or 100 Hz and sending them via a pulse shaping unit to the recorder as the spectrum is being scanned. When the digital memory oscilloscope is used the readout is calibrated by taking pulses every 8, 16, or 32 channels and using these to mark the spectrum.

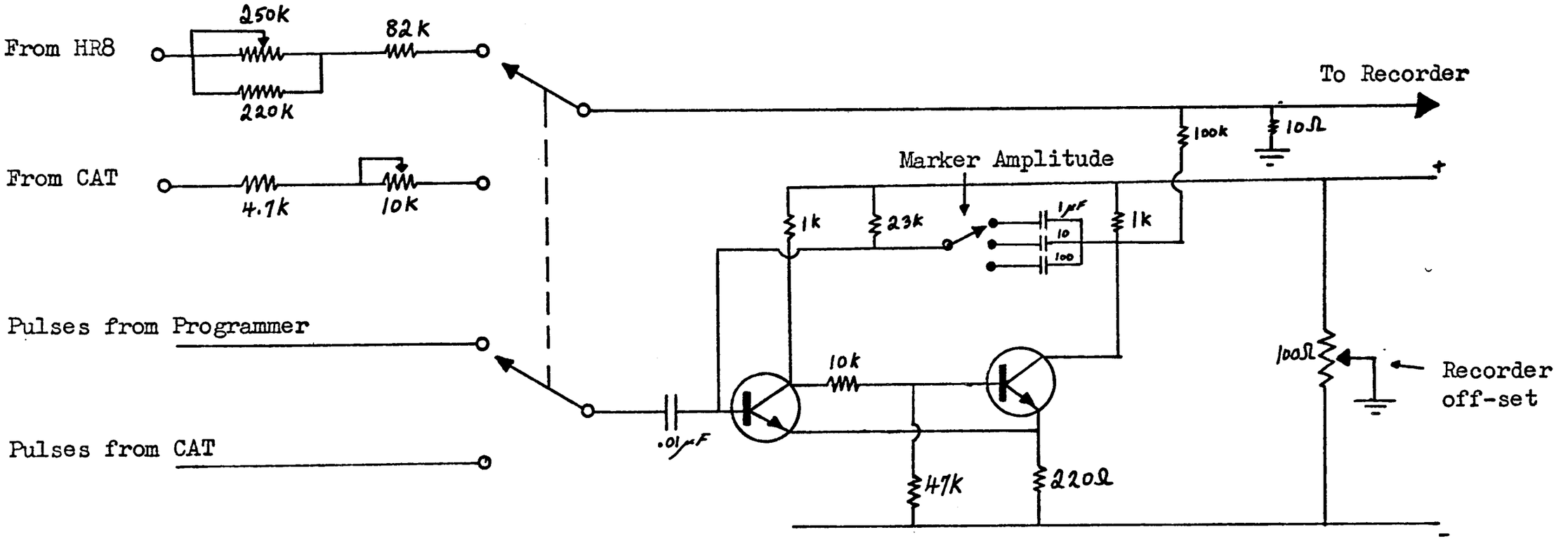


Figure 4.4 Recorder Interface

The recorder pen may be off-set by varying the d.c. level of its input.

In addition, full scale recorded spectra can always be obtained when necessary by attenuating slightly the output of the potential divider.

4.3 The Probes.

One of the most difficult parts in the construction of the spectrometer was the design and manufacture of the probes. Since frequency sweep was to be used a crossed-coil system was required. In addition the geometry of the magnet imposed some problems.

To excite magnetic resonance the radiofrequency field H_1 has to be perpendicular to the axis of the solenoid. For convenience the sample access should be along this axis as well. To achieve this for our magnet a method used is an extension of a design by Redfield (30) and is shown in figure 4.5.

Two similar solenoids are mounted perpendicularly to each other and to the axis of the sample in a copper tube with cutouts as shown. The arrangments of these cut-outs is such that both the transmitting coil and the receiving coil are coupled to the sample space by a copper loop acting as a single turn transformer. Magnetic coupling between the two coils is small because of their relative orientation and electric coupling is minimized by placing a metallic screen between the two coils. This screen is slotted to coincide with the slots in

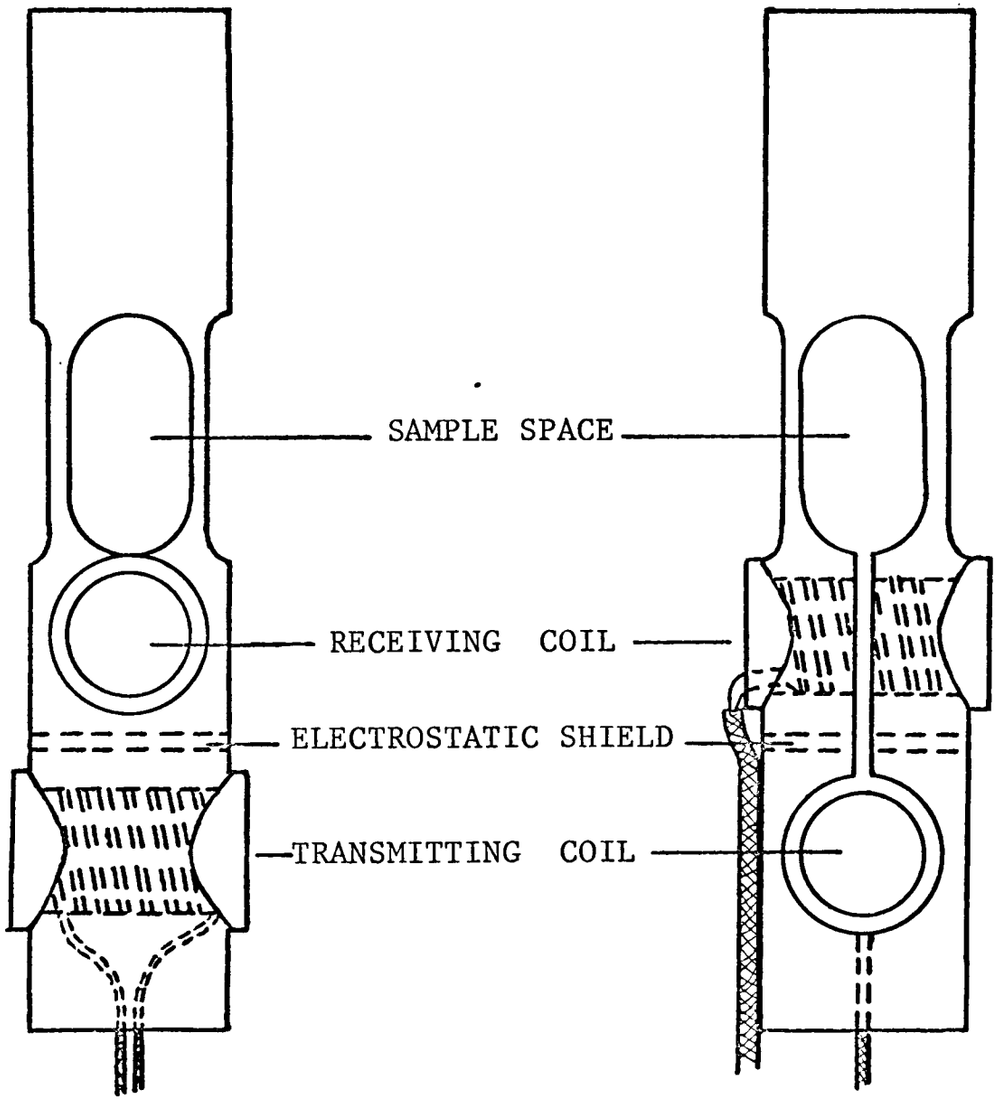


Figure 4.5 Diagram of probe head

the copper tube. Concentric with the slotted copper tube is a larger copper tube which acts as an earthed screen and upon which are wound the modulation and sweep coils. The field homogeneity coils are fitted on a separate 'Perspex' former.

The two coils are tuned and matched to 50 Ω by capacitors mounted in two separate compartments of an aluminium tube attached to the probe head. The circuit for tuning and matching is shown in Figure 4.6 with typical values for 30 MHz operation. Figure 4.7 shows the complete probe for use with a 10 mm. diameter sample.

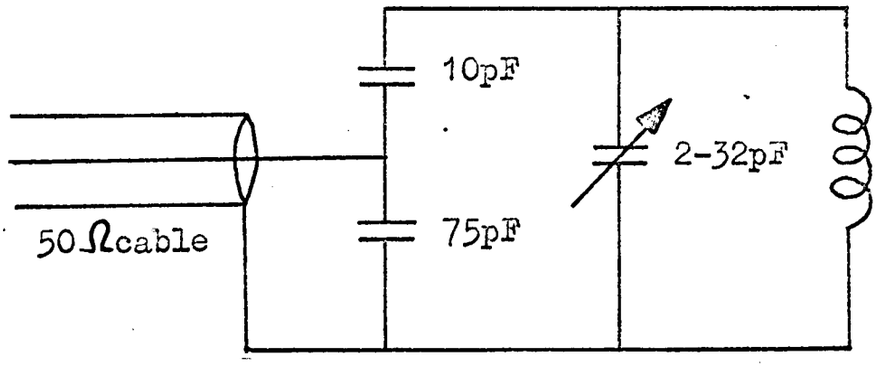


Figure 4.6 Circuit for tuning and matching the probe


31
30
29
28
27
26
25
24
23
22
21
20
19
18
17
16
15
14
13
12

The transmitting coil is connected to the capacitors in the upper compartment of the aluminium tube. The receiving coil is connected to the capacitors in the lower compartment via a length of screened cable. Much of the residual coupling between the transmitting and receiving coils is due to this cable and its connection to the receiving coil. This coupling can be minimized by rotating the receiving coil about its own axis before fixing it into position. In this way a decoupling of about 70 dB between the input and output leads of the probe can be achieved.

The decoupling is improved with adjustable 'paddles' around the sample space. Two paddles are mounted on a pair of semi-cylindrical perspex formers between the two tubes forming the probe head. One paddle is a loop of high conductivity copper to give a predominantly reactive coupling while the second is a sheet of gold foil, whose thickness is about equal to the skin depth to give a mainly resistive coupling. The paddles may be rotated in unison about the probe axis or moved independently in a longitudinal direction and can be adjusted to give an overall decoupling of about 100 dB between the input and output leads.

The sample is contained in a flat bottomed glass tube, or if the effect of sample susceptibility is important, in a spherical bulb which is located directly above the receiving coil. The effective sample volume is determined by the shape of the cut-out in the copper tube. Measurements with a search coil in the sample space show that the

coupling to the receiving coil is very tight so that a good filling factor is obtained. Coupling between the transmitting coil and the sample space is not so strong, H_1 being reduced by a factor of about 3 from the field in the transmitting coil.

The tuning range of each probe is about a factor of 1.5 in frequency so that 6 probes are needed to cover the whole frequency range.

A more conventional crossed coil probe has recently been used in which two Helmholtz coils, separated by a Faraday shield, are wound directly around the sample (Figure 4.8). The coils are embedded in epoxy resin (Araldite MY 750) to keep the thickness of the structure to a minimum, but even so the outside diameter is close to that of the shield carrying the modulation and sweep coils. There is insufficient room to use a set of paddles as previously described. However, a 'Perspex' cylinder with a segment of gold foil(4mm x 10mm) attached can be slipped between the coils and the shield to act as single paddle.

The transmitter and receiver coils are first decoupled by rotation of the receiver coil relative to the transmitter coil. For the 80MHz probe with single turn coils this decoupling is very good, but for the lower frequency probes it lessens. With the gold foil paddle better overall decoupling can be achieved than with the previously described probes.

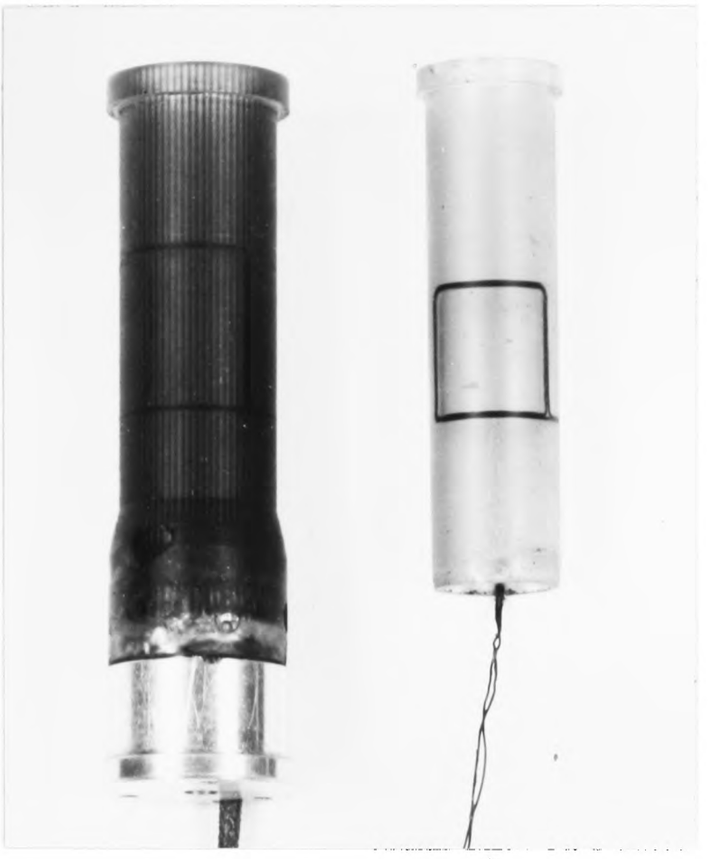


Figure 4.8 Crossed coil probe (Design 2) for superconducting magnet.

4.4 Sample Changing.

To change samples the entire probe must be removed from the dewar. To facilitate this the probe is mounted on a platform that can be lowered and then swung from under the dewar. (Figure 4.9). The platform is counterwighted to hold the probe in position when it is raised. To ensure accurate replacement of the probe (the Golay coil corrections are very critical, so they must be returned to the same point each time) a locating ring is fixed to it that sits flush with the base of the dewar when the probe is raised. This ring is threaded 40 turns/inch so very small height adjustments can be made to obtain the optimum position for the probe.

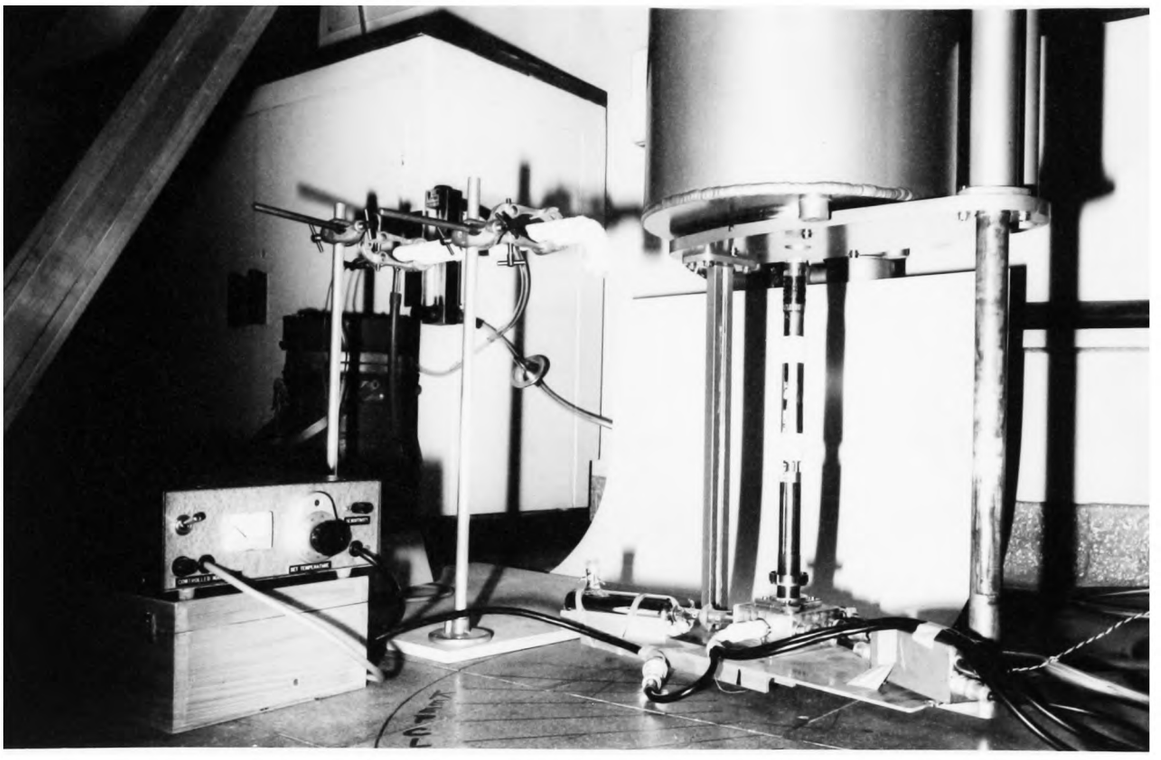


Figure 4.9 Platform for probe and pre-amplifier.

4.5 Sample temperature control.

To incorporate variable temperature capability it was necessary to change the aluminium room temperature dewar insert for a stainless steel one, to provide thermal isolation of the insert from room temperature. There is insufficient space in the insert to put a dewar around the sample so the entire probe head must be brought to the sample temperature. This puts an upper limit on the temperature range available, $\sim 100^{\circ}C$, as components in the probe start to soften above this. The sample temperature is controlled, by a unit built in this laboratory, within the range $-100^{\circ}C$ to $+100^{\circ}C$ by the heating of a gas that flows through the probe. The temperature sensing element

is a platinum resistance thermometer built into the probe head. For temperatures $>10^{\circ}C$ compressed air is used and for $<10^{\circ}C$ nitrogen gas boiled off from a 20 litre dewar of liquid nitrogen. The temperature can be maintained to better than $\pm 0.1^{\circ}C$ with this arrangement. Figure 4.9 shows the variable temperature apparatus.

4.6 Performance of the spectrometer.

A spectrometer may be judged by its sensitivity, precision, and ease of operation.

4.6.1 Sensitivity.

The sensitivity of the spectrometer is illustrated in figure 4.10 which shows an ^{2}H resonance from a sample of distilled water doped to 0.01M in $MnCl_2$. A field sweep derived from the digital memory oscilloscope was used. Sample volume 1 ml., sweep speed 0.512 msec./point, No. of channels 512, time constant 3 msec., total accumulating time for 1024 scans, 268 sec.

^{133}Cs resonances obtained with a frequency sweep from very dilute solutions are shown in figure 4.11.

4.6.2 Precision

The precision of the spectrometer may be judged from the experimental shifts recorded in Chapters 6 and 7. Measurements of the ^{133}Cs chemical shifts are reproducible to ± 0.05 ppm.

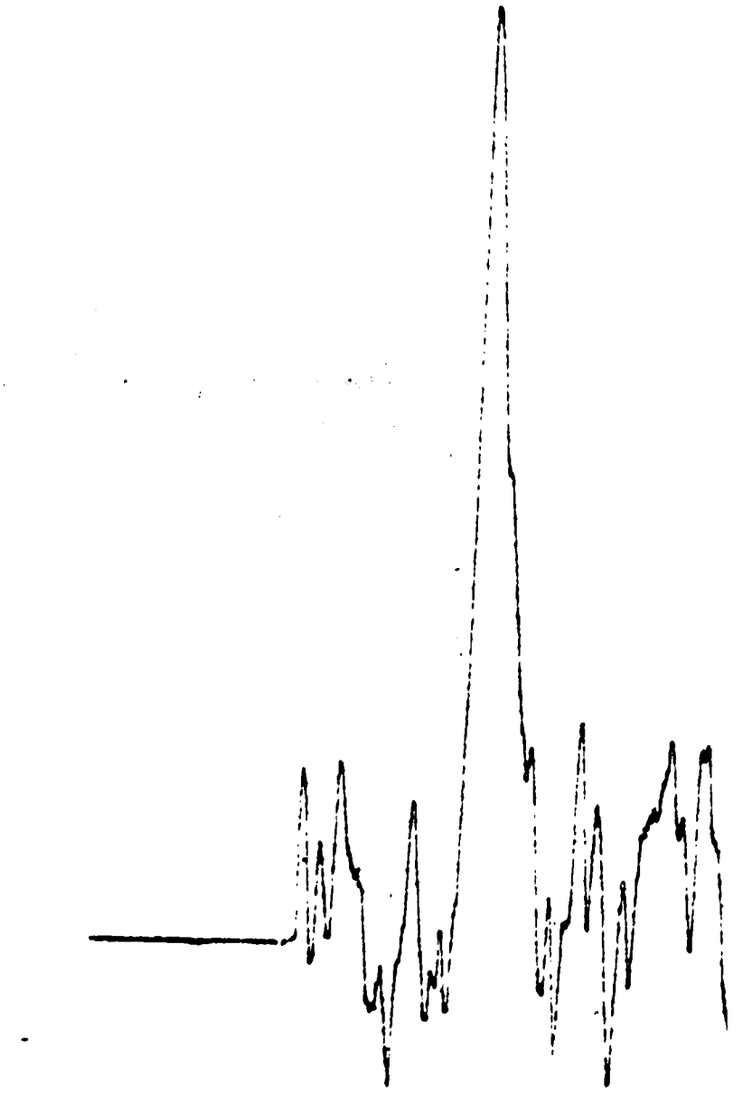
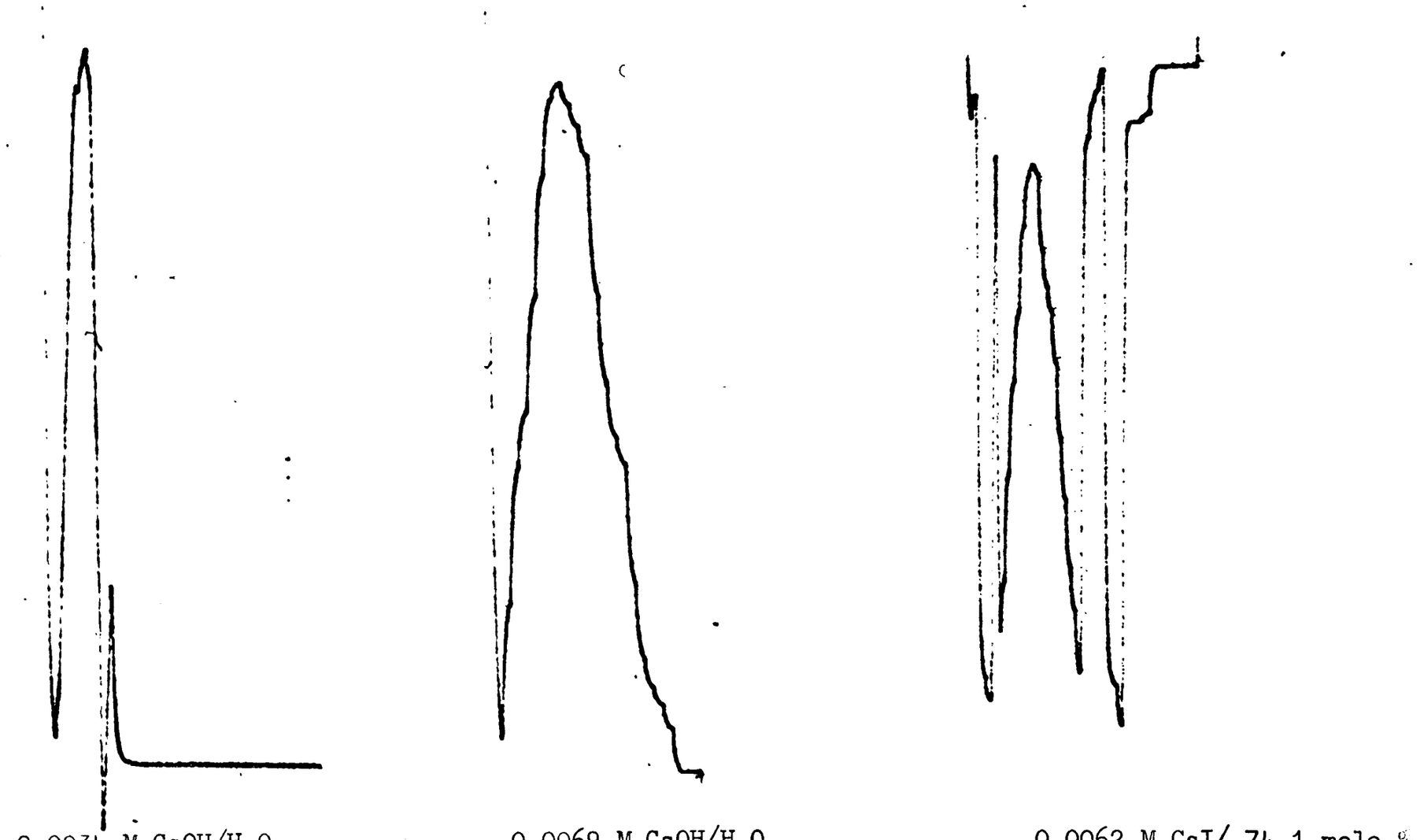


Figure 4.10 D_2O in natural abundance. Recording time 268 sec. Sample volume 1 ml., 1024 scans, time constant 3 msec.



0.0034 M $CsOH/H_2O$ 0.0069 M $CsOH/H_2O$ 0.0062 M CsI/ 74.1 mole % TETRAHYDROTHIOPHEN-1,1-dioxide

Figure 4.11 Examples of resonances obtained from very dilute solutions.

4.6.3 Ease of operation.

Features of the spectrometer that greatly aid the operator include:

1) Magnet Stability.

The magnetic field drift over a period of 24 hours is negligible so reference solutions do not have to be repeatedly run during a series of chemical shift measurements.

2) Frequency programming.

The frequency sweep may be programmed to scan repeatedly over a selected frequency range. Thus multiple recordings of a resonance may be made without the operator's constant presence.

3) Spectra calibration.

When frequency sweep is used the spectra can be automatically calibrated in frequency units. If frequency swept spectra are recorded on the digital memory oscilloscope, the resonance frequency may be read directly from the output trace displayed on the oscilloscope or the spectra calibrated in multiples of 8 channels when read out on a chart recorder.

4.7 Problems encountered with the spectrometer.

4.7.1 Low frequency noise.

When operated at low modulation frequencies, to observe the first derivative of a broad resonance, the noise level is higher than when operated at modulation frequencies $\geq$ 1 kHz.

After a careful investigation for the source of this low frequency noise that exonorated the transistorized pre-amps, it was found to come from the Schlumberger FSX3005 frequency synthesiser. Nothing can be done to remedy this short of replacing the FSX3005. However, above 200Hz this noise is not too significant. For most narrow lines, < 500Hz, modulation frequencies between 1 and 2 kHz are used and the centreband of the first a.c. component observed. As indicated in Chapter 1 this gives the optimum signal to noise.

4.7.2 Modulation pick-up

With probes of the modified Redfield type (figure 4.5) modulation pick-up under some conditions has proven troublesome. These are when modulation frequencies of 2-5 kHz are used and large modulation amplitudes are needed to obtain $\beta = 1.8$. Possible sources for this pick-up are 1) Vibrations induced in the copper shield holding the modulation coils, 2) Flexing of the thin sections of copper tube surrounding the sample volume and 3) Mechanical vibrations of the transmitter and receiver coils.

Modulation pick-up in the probes with the Helmholtz receiver and transmitter coils potted in epoxy resin (Figure 4.8) is much less. Here the transmitter and receiver coils are much more rigidly held.

4.7.3 Homogeneity degradation.

When probes of the second type described were tried

the best homogeneity that could be achieved was less than that previously attained using the modifield Redfield design probes. The epoxy resin introduces inhomogeneities into the field that cannot be fully corrected with the Golay correcting coils, either the superconducting or room temperature ones. The best homogeneity attainable over a 9 mm. diameter sphere is approximately 0.8 ppm.

Conclusion.

The spectrometer described in this chapter has been in use now for approximately one year and has indeed proven very versatile and reliable. The spectrometer has been used by members of this research group to measure resonances of many nuclei, including ^{2}H, ^{7}Li, ^{23}Na, ^{27}Al, ^{35}Cl, ^{81}Br, ^{133}Cs, and ^{139}La. In particular the author took advantage of the spectrometer's sensitivity and stability to measure cesium chemical shifts to a high accuracy in dilute solutions of cesium salts in aqueous and non-aqueous media. These measurements are discussed in Chapters 6 and 7 after a brief description in Chapter 5 of the theory of chemical shifts in electrolyte solutions.

Chapter 5. The Chemical Shift in Alkali Halide ions

In this chapter a brief survey is made of the factors affecting the shielding of alkali halide nuclei in crystals and in solutions. A theory to account for the shifts in solution is introduced.

5.1 Introduction.

A chemical shift is observed when an unperturbed closed shell ion is placed in an external magnetic field. This occurs because the entire spherical electron cloud rotates about the field direction as if it were a rotating rigid sphere of electricity. This sets up a field at the nucleus which both opposes and is proportional to the external field H. Therefore the effective magnetic field which acts on the nuclear moment can be expressed as

$$H_{eff.} = (1-\sigma)H \qquad 5.1$$

where σ is the screening (or shielding) constant. This shift was first described by Lamb (31) and bears his name. However if perturbations are produced in the spherical symmetry by some external force the electrons are no longer completely free to rotate about the direction of H and the theoretical expression for the shielding constant involves an additional term which opposes the Lamb term. Ramsay (32) considers this and calculates an expression for the shielding composed of two parts where

$$\sigma = \sigma_d + \sigma_p \qquad 5.2$$

σ_d - the diamagnetic term is equivalent to the Lamb shift and

σ_p - the paramagnetic term allows for the distortion of spherical symmetry and the consequent introduction of angular momentum into the ground state.

5.2 Chemical Shifts in Alkali Halide Crystals.

Before discussing chemical shifts obtained from aqueous solutions it is worth considering shifts in solid alkali halides, for here the ions are surrounded by a rigid lattice and most parameters affecting the shift are known.

Alkali halide crystals are predominantly ionic in character. If ionic crystals are considered simply as combinations of distinct positive and negative ions, each constituent ion having a spherically symmetric closed-shell electronic configuration the same as that expected for an isolated ion and the crystal is held together only by electrostatic forces, the shielding constant of the ionic nuclei is determined solely by the diamagnetic term of Ramsay's expression. However, for real crystals additional interactions present distort the symmetry of the electron distribution and introduce some net orbital angular momentum into the ground state of the ion giving rise to a paramagnetic contribution to the shift. This shift essentially arises from changes in the p-electron densities of the alkali or halide ions.

Three possible interactions that may cause chemical shifts in alkali halide crystals are:- 1) Electrostatic effects, 2) Covalency,

and 3) Overlap effects.

It has been shown that neither electrostatic nor reasonable estimates of the degree of covalency, especially for the larger ions in the alkali halides, can fully account for the magnitude of the shift observed (33,34). Kondo and Yamashita (35) proposed that short-range repulsive forces between the ions might be responsible for the chemical shifts. Calculations (33, 35-39) have shown that this mechanism can produce shifts of the magnitude observed. Mutual overlap of atomic wave functions of neighbouring ions produces a strong repulsive force mainly due to the Pauli exclusion principle. This force acts over a short range and competes with the electrostatic forces tending to reduce the separation of oppositely charged ions and produce equilibrium in the crystal.

Although the diamagnetic σ_d term is fairly large (about 5×10^{-3} for cesium ion) (45) only slight changes are introduced into it by these forces, usually 10^{-2} or 10^{-3} of the paramagnetic σ_p term (38). Therefore all changes introduced in the shielding of the nucleus can be considered as arising in the paramagnetic term of Ramsey's formula.

The complete expression for the shielding as derived by Ramsay (32) is

$$\sigma = \sigma_d + \sigma_p$$

$$= \frac{e^2}{2mc^2}\left[\langle\Psi_0|\sum_k \frac{r_k^2\hat{L}_k - \hat{r}_k\hat{r}_k}{r_k^3}|\Psi_0\rangle + \sum_m (E_0-E_m)^{-1}\left\{\right.\right. \qquad 5.3$$

$$\left.\left.\langle\Psi_0|\sum_k \hat{L}_k|\Psi_m\rangle\langle\Psi_m|\sum_k \frac{\hat{L}_k}{r_k^3}|\Psi_0\rangle + \langle\Psi_0|\sum_k \frac{\hat{L}_k}{r_k^3}|\Psi_m\rangle\langle\Psi_m|\sum_k \hat{L}_k|\Psi_0\rangle\right\}\right]$$

The first term represents the diamagnetic shielding while the second term corresponds to the paramagnetic shielding. Ψ_0 and Ψ_m correspond to the many electron ground and excited state wave functions, E_0 and E_m are the ground and excited state energies, L is the angular momentum operator and $L_z = \frac{\hbar}{i}\left(x\frac{\partial}{\partial y} - y\frac{\partial}{\partial x}\right)$, e and m are the electronic charge and mass, c is the velocity of light. However in this form equation 5.3 is not of much use since the excited state wave functions and energies are not known. If an average excitation energy, Δ, is introduced, this enables simplification of 5.3 to

$$\sigma = \frac{e^2}{2mc^2}\left\langle \Psi_0 \left| \sum_k \frac{r_k^2 \hat{L}_k - \hat{r}_k \hat{r}_k}{r_k^3} \right| \Psi_0 \right\rangle + \frac{e^2}{2\Delta m^2 c^2}\left\langle \Psi_0 \left| \sum_{kk'} \frac{\hat{L}_k \hat{L}_{k'}}{r_k^2} \right| \Psi_0 \right\rangle \qquad 5.4$$

where only ground state wave functions are involved. Here the summation is taken over all electrons in the crystal. L_k is the angular momentum of the K^{th} electron and r_k is the radial distance of the K^{th} electron from the origin at the nucleus. It is only necessary to consider overlap between the outermost s - and p orbitals of the central ion and neighbouring ions in deriving an expression for the paramagnetic shift of the resonance of the ionic nucleus in the crystals relative to the free ion. Inner core orbitals are tightly bound and do not extend far into the region between the ions so that they retain complete spherical symmetry and produce no contribution to the paramagnetic shielding constant.

The most exact derivation of the paramagnetic shift to be expected from overlap forces in alkali halide crystals is given by Ikenberry and Das (37) :

$$\sigma_p = \frac{-16\alpha^2}{\Delta} \langle r_i^{-3} \rangle_p \left[|S_{ij}^{\sigma s}|^2 + |S_{ij}^{\sigma\sigma}|^2 + |S_{ij}^{\pi\pi}|^2 - 2|S_{ij}^{\sigma\sigma} S_{ij}^{\pi\pi}| \right] \quad 5.5$$

where α is the fine-structure constant, $\left(\frac{e^2}{\hbar c}\right)$, $\langle r_i^{-3} \rangle_p$ is the expectation value of r_i^{-3} for an outer p-electron of the central ion, i, and Sij are the overlap integrals between the outer p-orbitals of the central ion, i, and the outermost s- and p-orbitals of other ions, j.

This overlap mechanism can make substantial contributions to magnetic shielding constants and is especially important for heavy atoms and ions having closed shell electronic configurations. Rubidium and cesium resonances show increasing shifts to low field as the size of the partner halide ion increases (40-42) and this is the qualitative behaviour one might expect if overlap effects make the main contribution to the shielding constant. Computed shifts for the solid alkali halides using equation 5.5 reproduce the qualitative features of the measured shielding constants (37).

However, it is not possible to make a direct comparison between calculated and experimental shifts since the former are expressed relative to a hypothetical "free ion" whereas the latter are measured relative to the shift of the ion in aqueous solution. There is a sizable contribution to the shielding from ion-solvent interactions.

The calculated and experimental shifts may be related by

$$\sigma_p = \sigma_{aqueous} + \delta_{expt.} \quad 5.6$$

Deverell (44) lists values of $\sigma_{aqueous}$ obtained by taking the difference between calculated and observed shifts. These are shown in Table 5.1.

Table 5.1

Shielding constants for the alkali halide nuclei at infinite dilution (14)

$aq.^{K^+} = -0.2 \times 10^{-4}$	$aq.^{Cl^-} = -2.25 \times 10^{-4}$
$aq^{Rb^+} = -0.2 \times 10^{-4}$	$aq.^{Br^-} = -4.3 \times 10^{-4}$
$aq.^{Cs^+} = -0.7 \times 10^{-4}$	$aq.^{I^-} = -6.0 \times 10^{-4}$

Although the above values are of limited accuracy they do show that large effects in the paramagnetic shift of the ionic nucleus occur in solution.

We now turn to a discussion of alkali halide shifts in solution.

5.3 Chemical Shifts of Alkali Halides in Solution.

The problem of calculating the chemical shifts of alkali and halide ions in solution is considerably more complex than when the ions are in a crystal. In the solid the relative positions and distances of separation of the ions in the lattice are known, but in solution the environment varies randomly with time as the ions and solvent molecules diffuse through the solution. The observed chemical shift results from an average of many instantaneous values corresponding to various short-lived environments in solution.

At infinite dilution the only interactions present are those between the ion and the solvent. As the concentration is increased the

shielding is altered 1) by modification of the original ion-solvent interactions and 2) by the presence of additional interionic processes. Therefore the observed chemical shift, $\sigma_{obs.}$, is, for cations

$$\sigma_{obs.} = \sigma_{ii}^{+-} + \sigma_{ii}^{++} + \sigma_{is}^{+o} \qquad 5.7$$

where σ_{ii}^{+-} is the contribution to the shift from cation-anion interactions

σ_{ii}^{++} " " " " " " " cation-cation "

σ_{is}^{+o} " " " " " " " cation-solvent "

A theory to explain these chemical shifts requires a knowledge of both the radial distribution function of other ions and solvent molecules about the central ion and the magnitude of the appropriate overlap integrals as a function of the separation. The necessary overlap integrals have been calculated by Hafemeister and Flygare (37) but the radial distribution functions are not available.

5.4 Calculation of the Ion-Ion Contribution to the Chemical Shift of Alkali halides in solution.

Dr. R.R. Sharp, a colleague of the author, has attempted the calculation of the ion-ion contribution to the chemical shift in solution. This necessitates the calculation of the radial dependence of the ions and solvent molecules about the central ion of interest.

The method used to calculate these shifts is outlined below.

The calculations discussed are for the $^{133}Cs^{+}$ ion.

5.4.1 The theory.

The ion-ion contribution to the chemical shift is a function of pairwise interactions between particles in solution. It can be obtained by integrating $\sigma_{ii}(R)$, the instantaneous shift due to the presence of a second ion a distance R from the ion of interest (Figure 5.1),

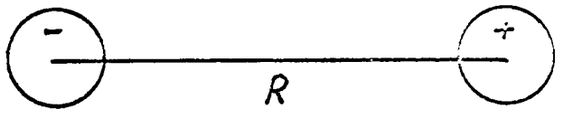


Figure 5.1 Presence of a counter-ion a distance R from the ion of interest.

weighted at each R by the ionic radial distribution function, over all R. Therefore

$$\sigma_{ii} = 4\pi \int_{R_1}^{R_2} \sigma_{ii}(R)\, n'(R,c)\, R^2 dR \qquad 5.8$$

where $n'(R,c)$ is the concentration (particles/cm^3) of oppositly charged ions a distance R from the ion of interest, when the bulk concentration (particles/cm^3) is $n(c)$ at C molar.

Difficulties arise in obtaining the expression for $n'(R,c)$ since

exact radial distribution functions for ions in solution are not known.

The Boltzmann expression for the local concentration of ions is given by

$$n'(R,c) = n(c) \exp\left(\frac{-z_i e \Psi_{el}(R,c)}{kT}\right) \qquad R > a \qquad 5.9$$

and

$$n'(R,c) = 0 \qquad R < a \qquad 5.10$$

where 'a' is the distance of closest approach.

In this case the function of $n'(R,c)$ appears as shown in figure 5.2A when the Debye-Huckel electrical potential (46), given by

$$\Psi_{el} = \frac{ze}{\varepsilon} \cdot \frac{\exp[K(a-R)]}{R(1+Ka)} \qquad 5.11$$

is used.

K = length of 'Debye-Atmosphere' (dimensions length $^{-1}$) and

$$K^2 = \frac{4\pi e^2 \sum n_i z_i^2}{\varepsilon kT}$$

This is not a good approximation for small R since it neglects the particle nature of the solvent in the first hydration sphere. The actual distribution is illustrated schematically in figure 5.2B.

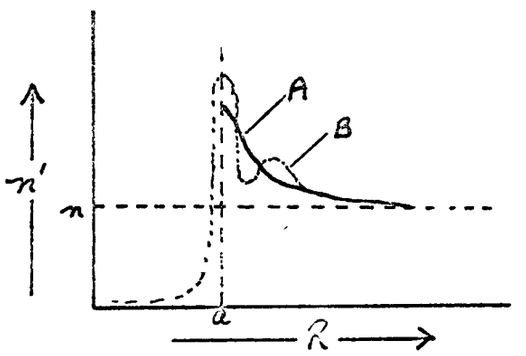


Figure 5.2 Distribution functions for

A) Boltzmann expression with Debye-Huckel potential
B) Actual distribution (Schematic)

An improvement in the Debye-Huckel potential for small R can be made. Consider the case for a cation, $^{133}Cs^{+}$ in particular. The dip in figure 5.2B is due to an instability in the position of the anion when it is anywhere in the region between the distance of closest approach, $r_c + r_a$, and $r_c + r_a + 2r_{H_2O}$ (Figure 5.3). The anion will either move to the distance of closest approach or hop out of the hydration sphere. If we make the assumption that whenever the anion is in the region between $r_c + r_a$ and $r_c + r_a + r_{H_2O}$ it can be treated as being at the distance of closest approach and anywhere outside this region it obeys the Debye-Huckel Boltzmann distribution then the expression for σ_{ii} can be divided into two components.

$$\sigma_{ii} = 4\pi \int_{r_c+r_a}^{r_c+r_a+r_{H_2O}} \sigma_{ii}(R)\, n'(R,c)\, R^2 dR + 4\pi \int_{r_c+r_a+r_{H_2O}}^{\infty} \sigma_{ii}(R)\, n'(R,c)\, R^2 dR \qquad 5.12$$

$\sigma_{ii}(R)$ in the first term is now a constant and the equation can be rewritten

$$\sigma_{ii} = 4\pi\, \sigma_{ii}(a) \int_{r_c+r_a}^{r_c+r_a+r_{H_2O}} n'(R,c)\, R^2 dR + 4\pi \int_{r_c+r_a+r_{H_2O}}^{\infty} \sigma_{ii}(R)\, n'(R,c)\, R^2 dR \qquad 5.13$$

where the first integral now determines the probability of the ion being in the region between $r_c + r_a$ and $r_c + r_a + r_{H_2O}$

The Debye-Huckel Boltzmann distribution in the first hydration sphere has approximately a 30% error when compared with more accurated potentials(50).

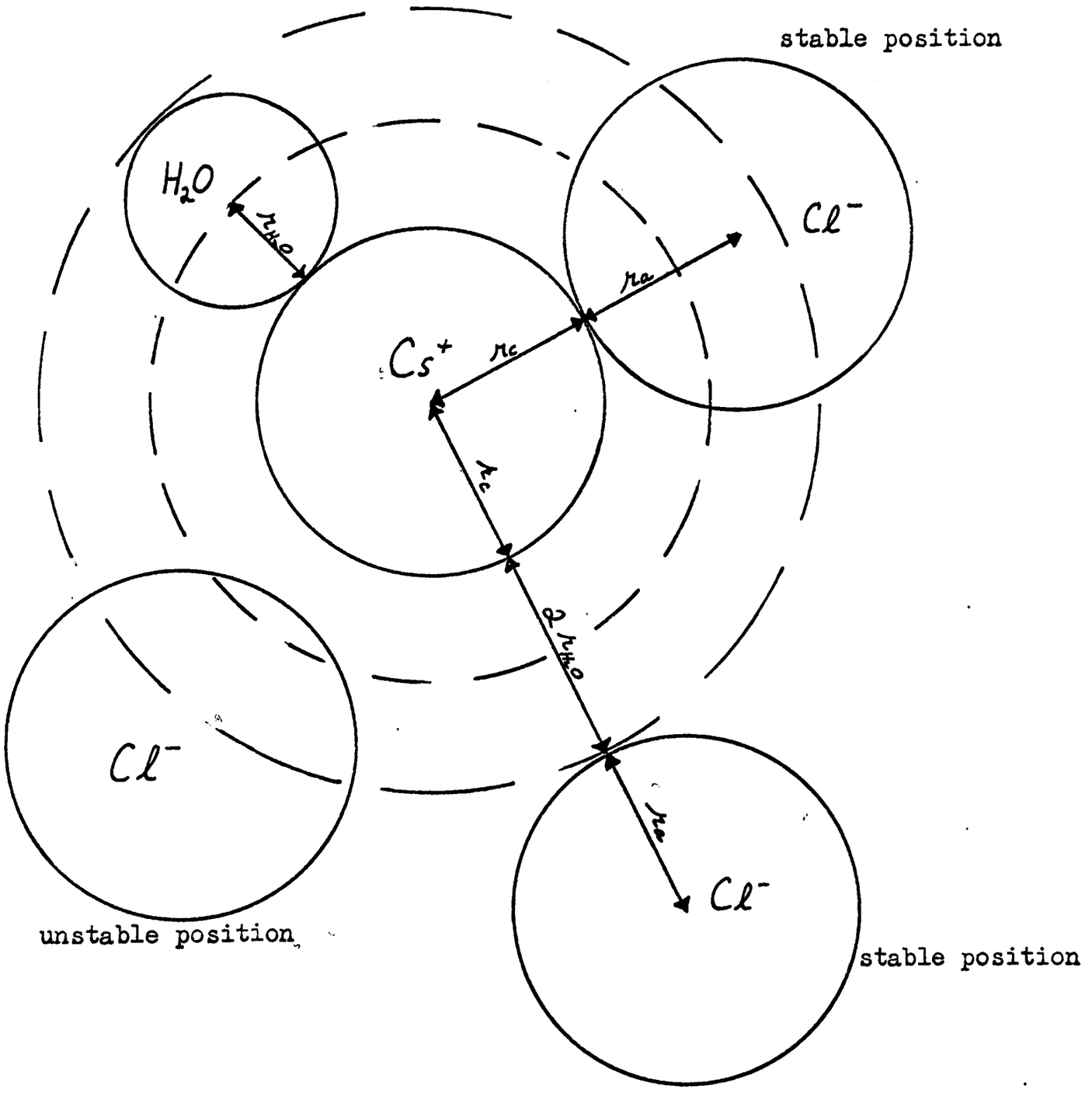


Figure 5.3 Model for the modification of the Debye-Huckel Boltzmann distribution, n (R,c), in the 1st hydration sphere

However this error is not too large since this is approximately an order of magnitude calculation, especially in the cases of ion-induced dipole and Van der Waals interactions. Other parameters that contribute to the overall error in the calculations are the distance of closest approach and in the case of the overlap calculations, errors in the tabulated overlap integrals.

Equation 5.8 cannot be integrated analytically but if the appropriate form of $\sigma_{ii}(R)$ is determined, it can be numerically integrated for any values of C, T, $\mathcal{E}$, and limits of integration R_1 and R_2.

5.4.2. Determination of form of $\sigma_{ii}(R)$.

The form of $\sigma_{ii}(R)$ depends on the type of interaction producing the chemical shift. As for the case of the calculation of the shift in solid alkali halides, the Ramsey formula is the starting point for the calculations. If it is assumed that the shifts due to ion-ion and ion-solvent interactions distort the closed-shell configuration of the ions and introduce solely a paramagnetic chemical shift, then only σ_p of the Ramsey formula need be considered.

$$\sigma_p = 2\left(\frac{eh}{2mc}\right)^2 \sum_{j,k,n_i} \frac{\langle 0|\frac{\hat{l}_k}{r_k}|n_i\rangle\langle n_i|\hat{l}_j|0\rangle}{(E_0 - E_i)} \qquad 5.14$$

where j, k are all electrons in orbitals about the nucleus of interest and the sum over n_i is a sum over excited states. Atomic units (a.u.) are used for these calculations. Therefore e=1, m=1, $c=\frac{1}{\alpha}$ (α is the fine structure constant), distances, r_k are in units of the Bohr radius (0.529A°), and energies

are in units of Rydbergs x 2.

If two closed shell ions a distance R apart in a dielectric continuum are considered, the following are possible interactions that may cause a distortion of the charge clouds and produce a chemical shift.

1) Electrical interactions.

These may be written as a multipole expansion (47) where

$$P.E. = -ec\left[\frac{1}{R} + \frac{r\cos\theta}{R^2} + \cdots\right]_{r<R} \qquad 5.15$$

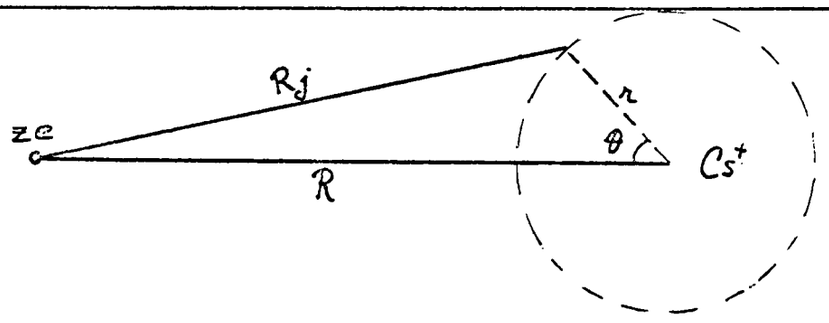


Figure 5.4 Interactions of point charge ze on 5p electrons of $^{133}Cs^+$.

The first term of 5.15 gives the potential energy between rigid spheres. The second term is the highest that considers charge cloud distortions, i.e. an ion-induced dipole term. The Hamiltonian is

$$\mathcal{H}_{\text{ion-induced dipole}} = -\sum_j \frac{ze^2 r\cos\theta}{R^2} \qquad 5.16$$

2) Polarization.

The lowest order interaction that considers mutual polarization

of the charge clouds is Vander Waals (48). The Hamiltonian is

$$\mathcal{H}_{\text{Van der Waals}} = \frac{e^2}{R^3} \sum_{ij} \left(-2 z_a^i z_b^j + X_a^i X_b^j + J_a^i J_b^j \right) \qquad 3.17$$

3) Overlap.

At very close-range wave functions overlap causing repulsion. Ordinarily it would be necessary to calculate the distortion in the orbitals caused by overlap by using an Orthogonalization technique. However, for the case of the alkali halides Hafemeister and Flygare (39) have calculated the overlap integrals as a function of distance. In addition Ikenberry and Das (37) have given the most exact derivation of the shift to be expected from alkali halide ions in crystals. In their case there were 6 anions surrounding the cation. Their expression has been reduced to the case of interaction with one halide ion and the explicit form of $\sigma_{ii}(R)$ obtained for the overlap mechanism.

It is necessary to solve the Ramsey expression for the cases of ion-induced dipole and Van der Waals interactions to obtain the explicit form of $\sigma_{ii}(R)$. The Hamiltonians calculated for these interactions are substituted into the Ramsey expression for σ_p and using 4th order perturbation theory the solution is obtained. Dr. R.R. Sharp has done these calculations where the following approximations are made:-

1) The ground state for the cesium ion is assumed to be a product of 5p orbitals. This is reasonable since the outer p states are most readily distorted in an electrical field.

2) The excited states in the Ramsey expression are replaced by an average excitation energy. This is an assignable parameter and can be any reasonable value between the 1st singlet level and the ionization energy of a 5p electron. For cesium these values are determined spectroscopically and are 1.11 and 1.84 Rydbergs respectively. For these calculations a value of 1.30 Rydbergs has been chosen.

The final expressions obtained for $\sigma_{ii}(R)$ using the three mechanisms mentioned are:-

1) Ion-induced dipole

$$\sigma_{SCALAR}^{\text{ion-induced dipole}} = \left(\frac{2}{3}\right)\left[-\frac{4\alpha^2}{\Delta^3}\left(\frac{ze^2}{\varepsilon R^2}\right)^2\right]\left\langle\frac{1}{r}\right\rangle_p \qquad 5.18$$

2) Van der Waals

$$\sigma_{SCALAR}^{\text{Van der Waal}} = \left(\frac{2}{3}\right)\left[-\frac{4\alpha^2}{\Delta^3}\left(\frac{ze^2}{\varepsilon R^3}\right)^2\right] 5'\left\langle\frac{1}{r}\right\rangle_p \left\langle r^2\right\rangle_{p'} \qquad 5.19$$

3) Overlap

$$\sigma_{SCALAR}^{\text{Overlap}} = \left(\frac{2}{3}\right)\left[-\frac{4\alpha^2}{2\Delta}\right]\left[\left|S_{ab}^{\sigma s}\right|^2 + \left|S_{ab}^{\sigma\sigma}\right|^2 + \left|S_{ab}^{\pi\pi}\right|^2 - 2\,S_{ab}^{\pi\pi}\cdot S_{ab}^{\sigma\sigma}\right]\left\langle\frac{1}{r^3}\right\rangle_p \qquad 5.20$$

The constants of 1 and 2 are known and the radial dependence (on R) is explicitly stated. The radial dependence of 3) is not explicit, although absolute values of all overlap integrals and their dependence on R have been tabulated by Hafemeister and Flygare (39). The R dependence is exponential and in convenient form for numerical integration. Substitution of 5.18, 5.19, and 5.20 into 5.8 gives the value for ion-ion shifts after numerical integration on an Elliott 903 computer.

The distance of closest approach has been taken as the sum of the ionic radii. These are in agreement with X-ray data on alkali halide solutions (49) and are used so as to have a self-consistent set of numbers. The limits of integration are taken from the distance of closest approach to 12 Å, beyond this the interactions discussed are negligible. For the case of the overlap calculations the second term of equation 5.8 is assumed to be zero.

The results obtained from these calculations, even assuming that $\mathcal{E} = 1$ (due to dielectric saturation) in the first term of the Ion-induced dipole and Van der Waals interactions, indicate that the overlap mechanism is the dominant interaction in the case of cesium ions but for the smaller ions other interactions may become more important. The detailed results from these calculations are discussed in Chapters 6 and 7 with reference to the cesium chemical shifts measured by the author.

Chapter 6. $^{133}Cs^+$ Chemical Shifts in Aqueous Solutions.

6.1 Introduction.

In the previous chapter theories for the chemical shifts of alkali halide nuclei were discussed. Deverell (9, 10) has made a survey of the shifts of $^{23}Na^+$, $^{39}K^+$, $^{87}Rb^+$, $^{133}Cs^+$, $^{35}Cl^-$, $^{81}Br^-$, and $^{127}I^-$ in aqueous solution and has interpreted the observed shifts in terms of any overlap mechanism. However he was limited in the concentration range he could study (>0.1 molal), the accuracy with which he could measure the shifts, and by the lack of a computer to make detailed calculations based on his theory.

It would be of interest to observe the shifts in solutions of much lower concentrations than 0.1M. At very low concentrations ion-ion interactions become less important and ion-solvent interactions predominate.

A thorough investigation of the effects of ion-solvent and ion-ion interactions on the shielding of the cesium ion has been made and the results compared with the theory proposed in Chapter 5. Cesium was chosen because 1) it gives the largest chemical shifts among the alkali metal ions, 2) the shifts show marked non-linearity at low concentrations (9), 3) the cesium ion, although it has a spin of

$^{7}/_{2}$, has a very small electric quadrupole moment and it is not quadrupolar broadened in solution. The recently measured line width by pulse techniques in this laboratory is approximately 0.03Hz in a 3.8M solution of $CsCl/H_2O$. Therefore the cesium ion is both chemically interesting in its interactions with solvent and other ions and it is most amenable in allowing accurate measurements of its chemical shift to be made at very low concentrations.

The spectrometer described in chapter 4 enabled the author to measure cesium chemical shifts in solutions with concentrations as low as 0.005M to an accuracy of $\pm$0.05ppm.

6.2 Experimental.

To obtain as much information as possible about $^{133}Cs^{+}$ interactions in solution the concentration, the anions, the isotopic composition of the solvent, and the temperature were varied.

$^{133}Cs^{+}$ chemical shifts were measured in solutions of CsI, CsBr, CsCl, CsOH, and $CsNO_3$ in three isotopes of water, H_2O, D_2O, and $H_2{}^{18}O$.

The solutions were made up by weight using a Stanton Unimatic balance (calibrated to read to 0.1mg.) and the concentrations expressed as moles/kilogram of solvent (Molality).

Unless otherwise stated measurements were made at 25°C ±0.1°C. The temperature was controlled by a temperature controlling unit built in this laboratory and the temperature checked with a calibrated copper/constantan thermocouple attached to the probe. This emf was read on a Cambridge Potentiometer sensitive to 1μV.

Spherical sample bulbs were used to eliminate errors caused by bulk susceptibility corrections. The probe design made the calculation of these corrections for cylindrical samples very difficult and imprecise. The effect of slight changes in sample height at the neck of the bulb was checked and found to be negligible.

The effect of dissolved oxygen in H_2O on the chemical shift was also investigated. Once again any effects observed were within the experimental error quoted for the measured shifts.

The main source of error in the measurements was in the positioning of the sample in the probe. A shift of from 0.5 to 1.5Hz. can be observed by removing the sample and replacing it. By the use of a snug fitting Teflon plug in the neck of the probe this error was reduced to less than 1Hz.

6.2.1 Solvents.

H_2O was distilled twice before use.

D_2O, 99.7 gms/100gms D_2O, was obtained in 25 gm. ampoules from Norsk Hydro-Elecktrisk and used without further purification.

$H_2{}^{18}O$, 2.135gms, 97.94% ^{18}O, 0.39% ^{17}O, normalized in ^2H was a sample kindly donated by Professor A. Lowenstein. This was recovered by vacuum distillation for reuse. The distillation apparatus used to provide minimum losses and contamination is illustrated in figure 6.1.

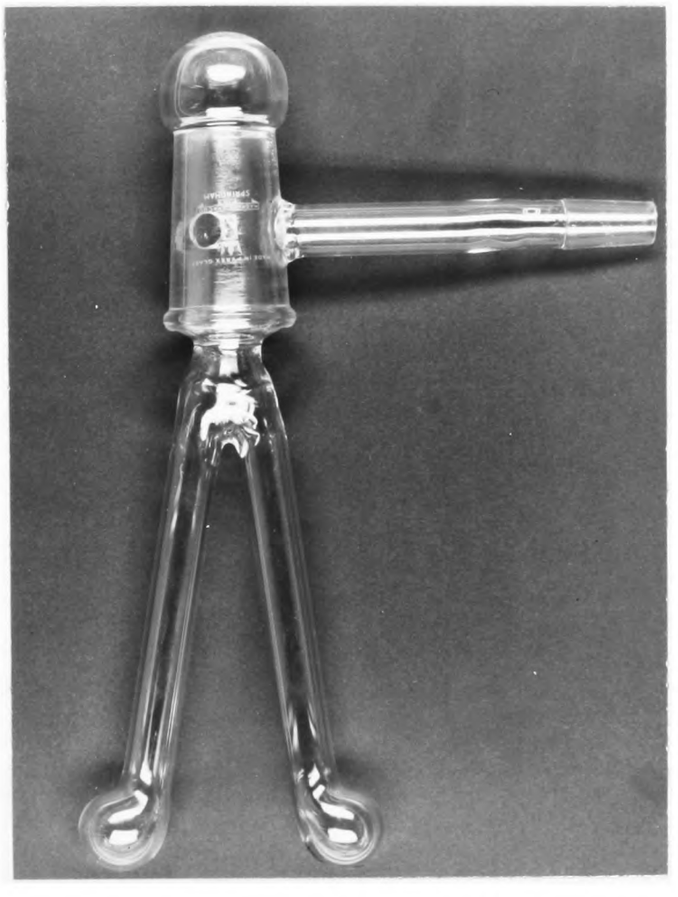


Figure 6.1 Distillation apparatus for $H_2{}^{18}O$

6.2.2 Salts

The cesium salts were obtained from the sources listed and were used without further purification.

CsCl	-	'Analar'	grade, quoted	99.9%	, obtained from	BDH.
CsBr	-	GPR	grade, quoted	99.5%	, obtained from	BDH.
CsI	-	"	" "	99.%	" "	"
CsOH	-	"	" "	99.9%	, " "	Koch-Light
$CsNO_3$	-	"	" "	97.%	, " "	BDH

Analysis of the halogen ion in CsCl, Br, I yielded

CsCl - 99.9% , CsBr - 99.9% , CsI - 101.4%

The salts, except CsOH, were dried for several hours at 120°C and kept in a dessicator except during the weighing operations. The CsOH, which is very deliquescent, was made up as a stock solution, ~1M, and the concentration determined by titration of the OH^- with HCl.

6.3 Results.

The chemical shifts measured are referenced to an external standard of 1.994M $CsCl/H_2O$. They have not been recalculated to shifts from infinite dilution for graphical presentation since this lowers

their accuracy. Multiple diagrams are employed to illustrate the shifts since the scale required for shifts over the entire concentration range is inadequate for detailed presentation of the effects at low concentrations. The shifts are reproducible to $\pm$0.05 ppm. and $\pm$0.015ppm. on any particular run. Most shifts are determined from 6 or more recordings of the resonance. For the lower concentrations when the C.A.T. was used, the average of 3 separate accumulations was taken.

The variation of the chemical shift of the $^{133}Cs^+$ ion as a function of concentration and anion is shown in figure 6.2a,b,c. Figure 6.3 shows the effect of varying concentration and anion in D_2O. The $^{133}Cs^+$ chemical shift as a function of concentration in H_2O, D_2O, $H_2{}^{18}O$ is shown in figures 6.4a, b. Figure 6.5 illustrates the absolute temperature variation of the $^{133}Cs^+$ shift as a function of concentration in H_2O and D_2O.

As an additional check for the theory presented in chapter 5 the $^{35}Cl^-$ chemical shifts in the $CsCl/H_2O$ solutions were also recorded. These are shown in figure 6.6.

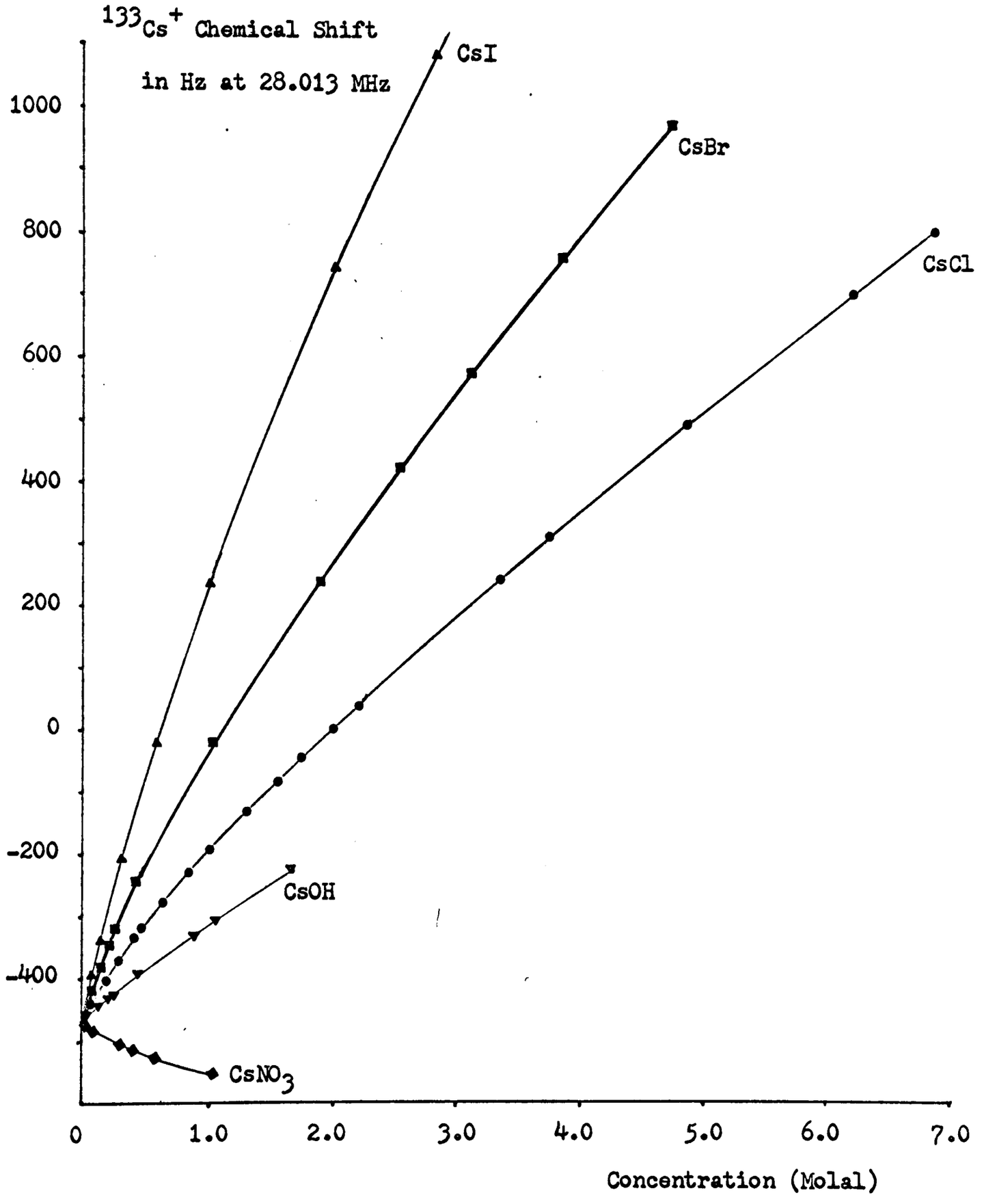


Figure 6.2a $^{133}Cs^+$ Chemical shifts vs Concentration (Molal) of Cesium salts in H_2O

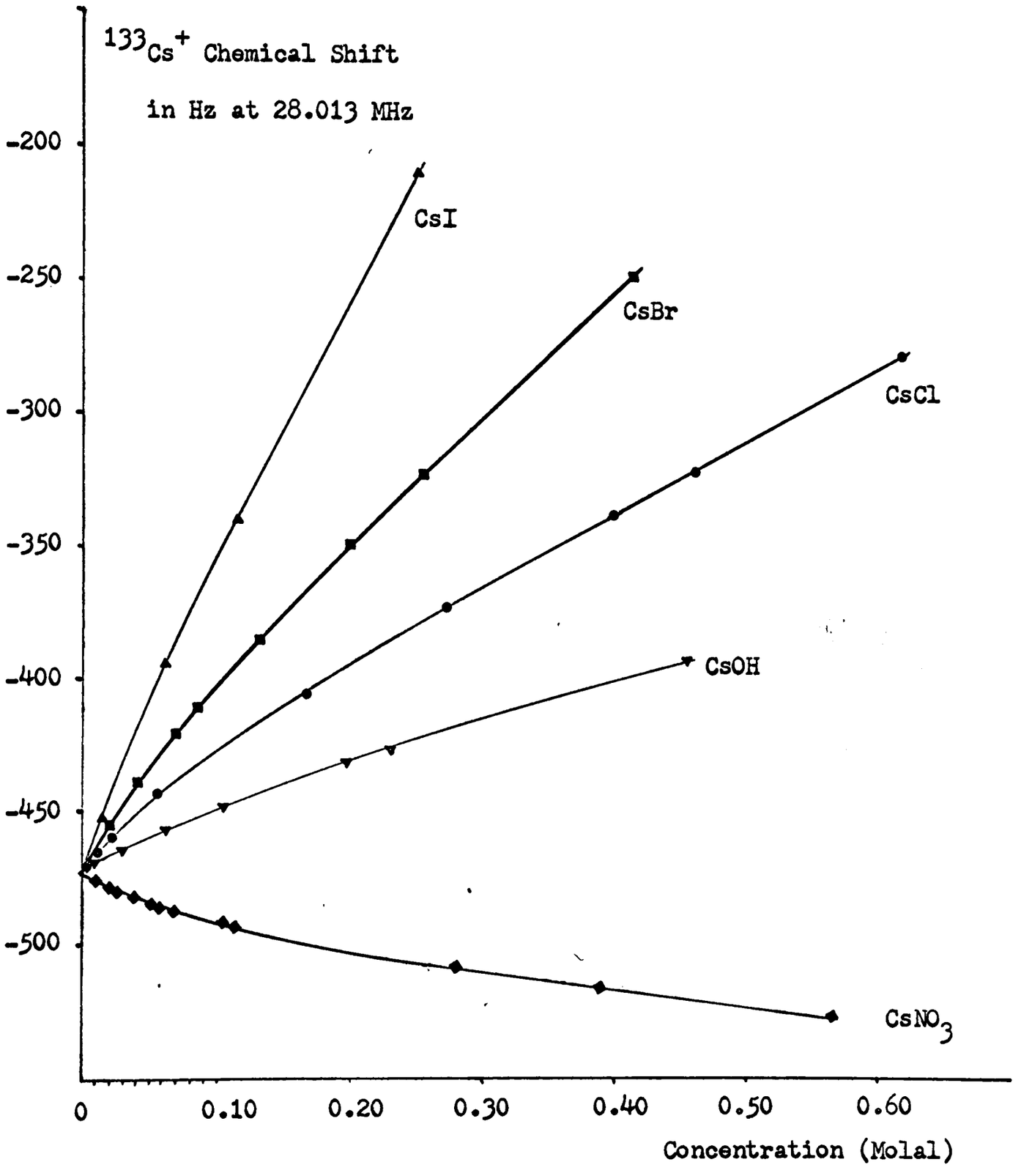


Figure 6.2b $^{133}Cs^+$ Chemical shifts vs Concentration (Molal) of Cesium salts in H_2O

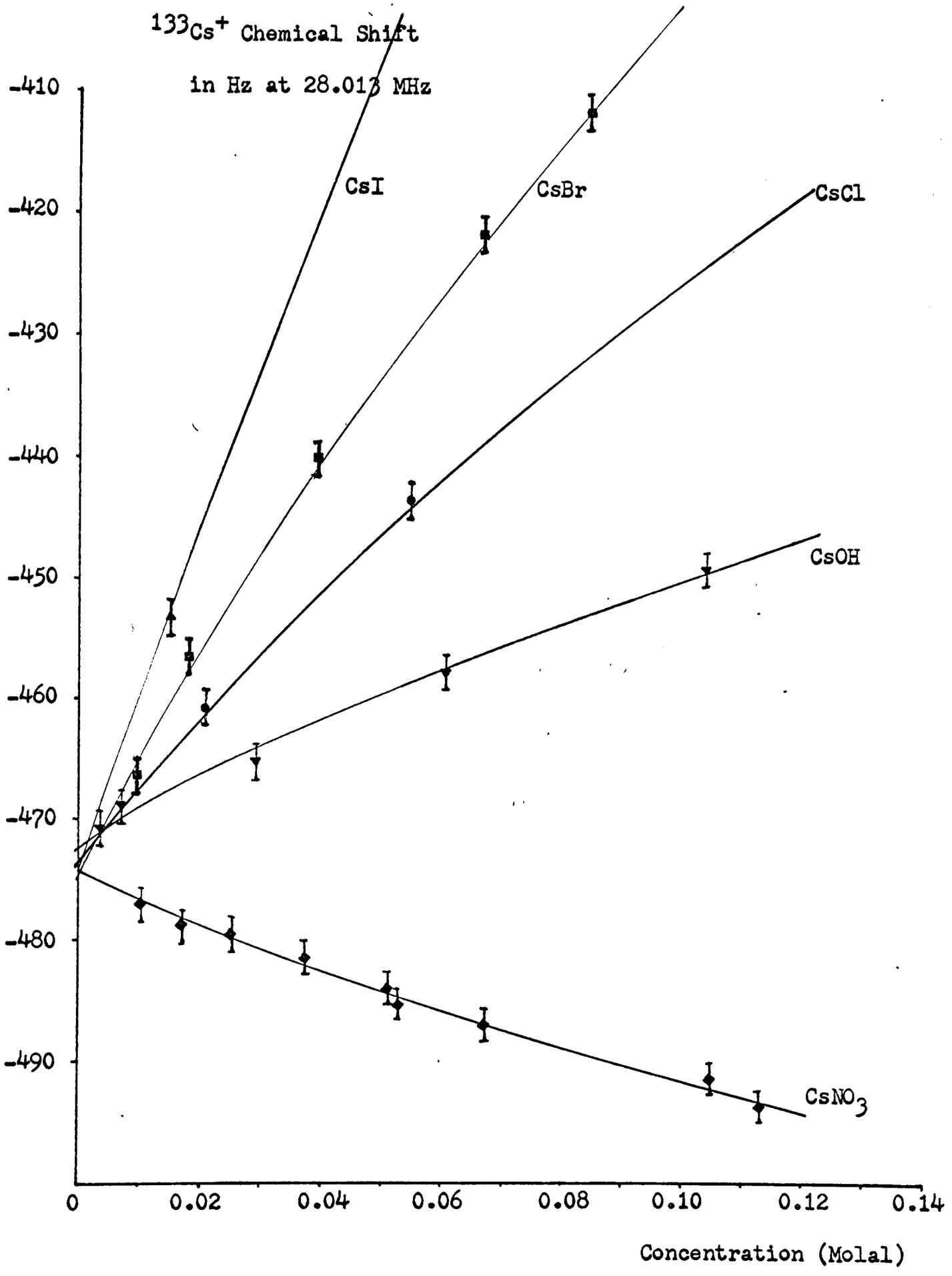


Figure 6.2c $^{133}Cs^+$ Chemical shifts vs Concentration (Molal) of Cesium salts in H_2O

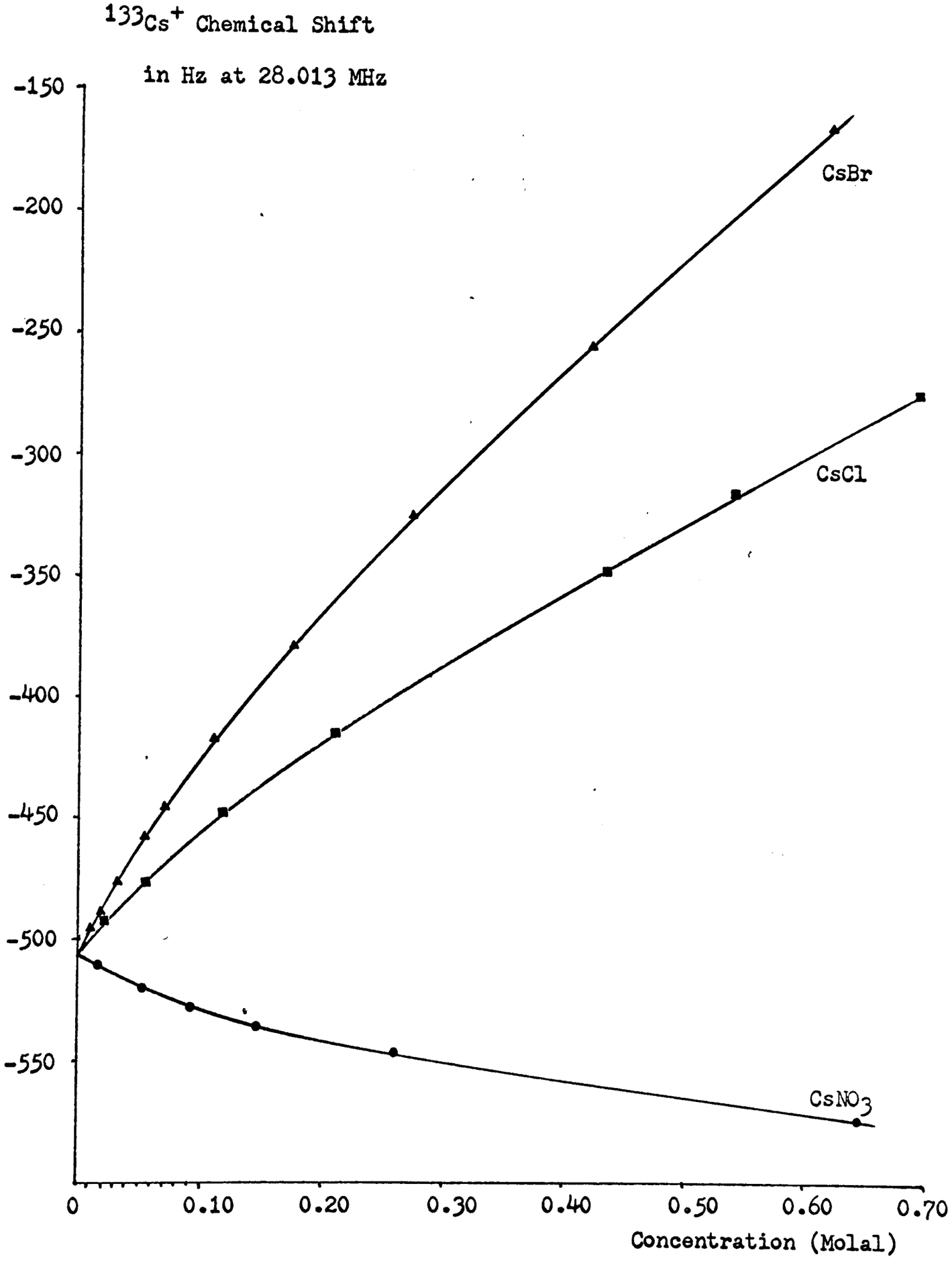


Figure 6.3 $^{133}Cs^{+}$ Chemical shifts vs Concentration (Molal) of Cesium salts in D_2O

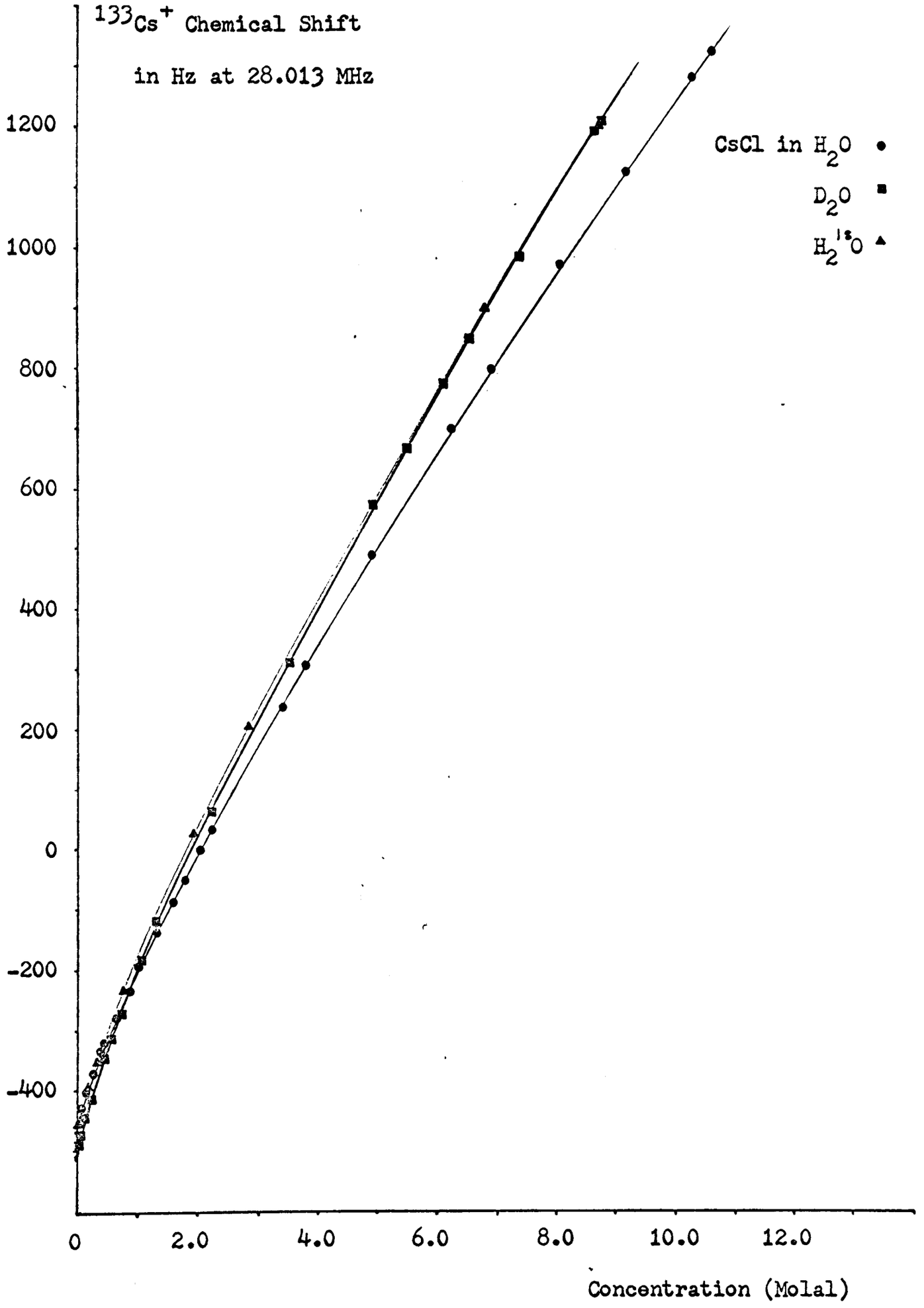


Figure 6.4a $^{133}Cs^+$ Chemical shifts vs Concentration (Molal) of CsCl in H_2O, D_2O, $H_2{}^{18}O$

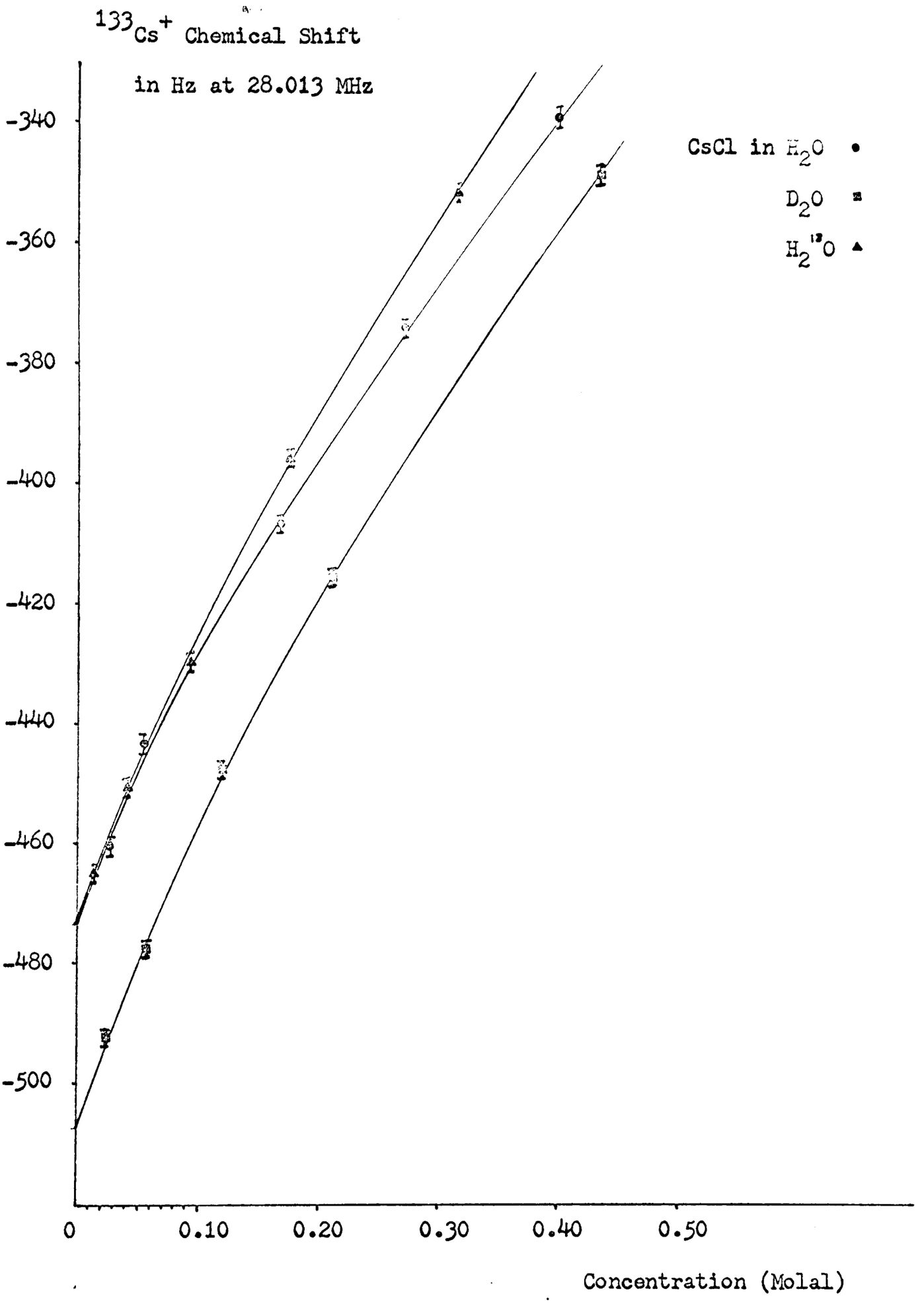


Figure 6.4b $^{133}Cs^+$ Chemical shifts vs Concentration (Molal) of CsCl in H_2O, D_2O, $H_2{}^{18}O$

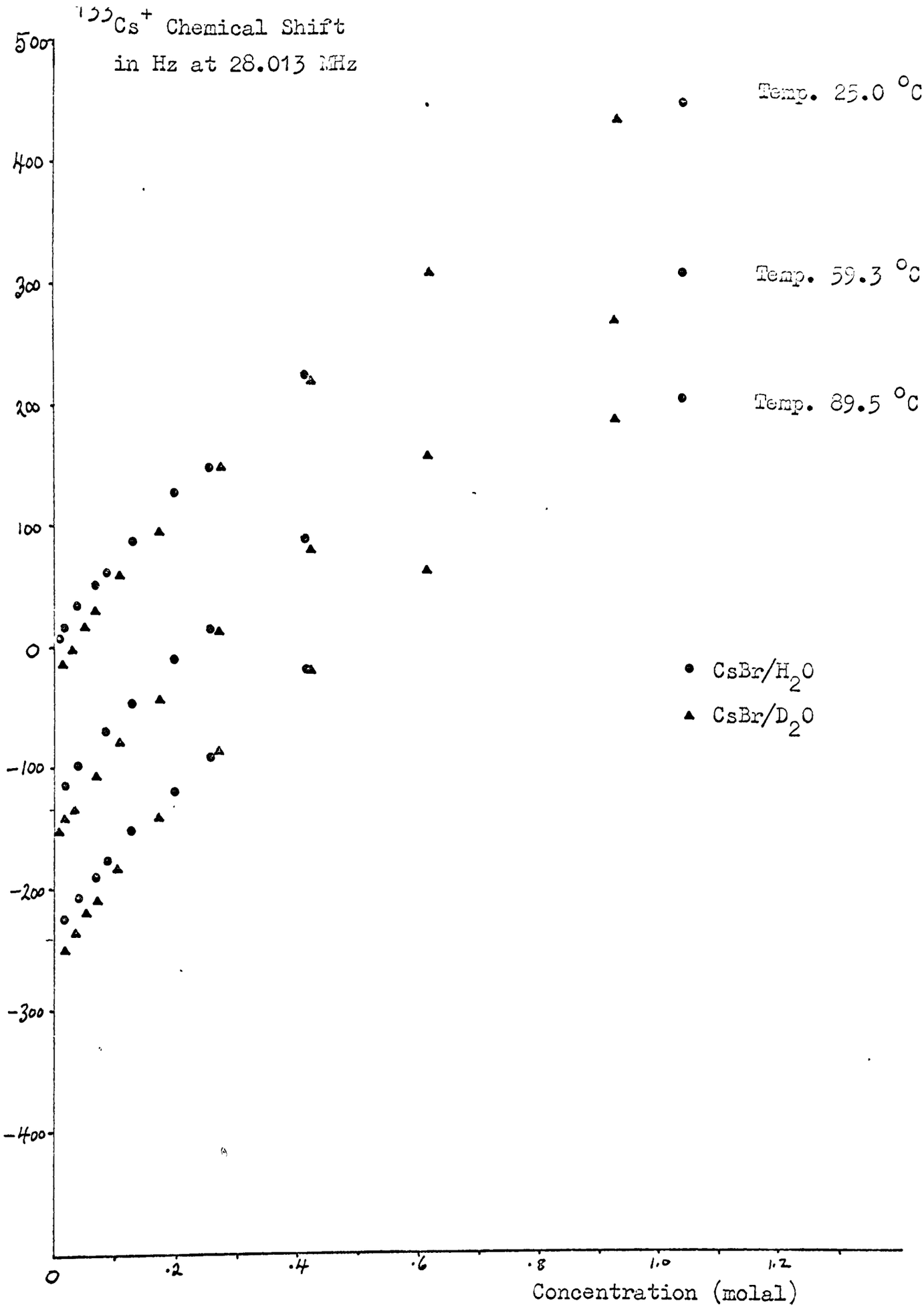


Figure 6.5 Temperature dependence of the $^{133}Cs^+$ shift relative to infinite dilution at 25.0 °C.

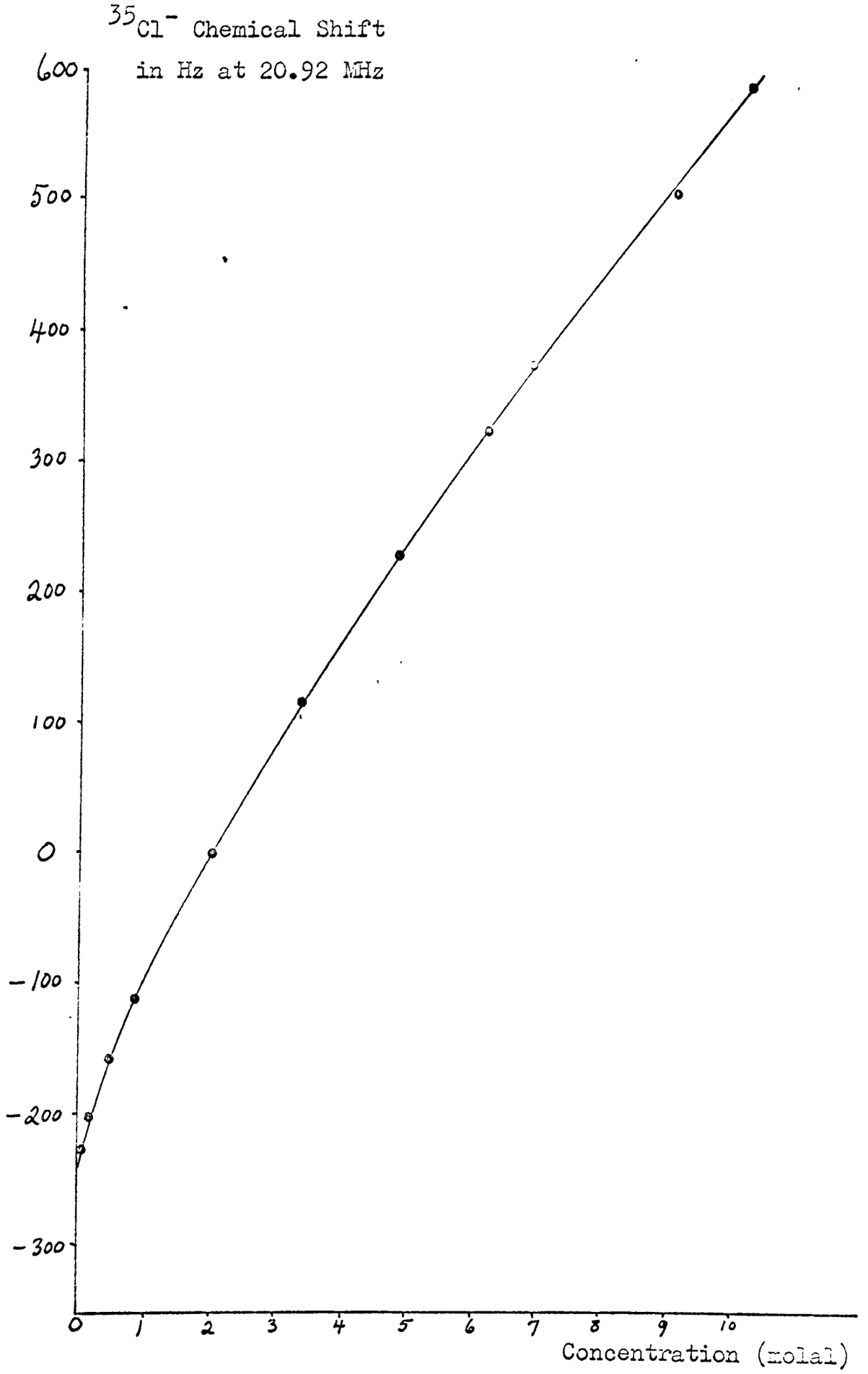


Figure 6.6 $^{35}Cl^-$ Chemical shift in $CsCl/H_2O$ vs concentration.

6.4 Discussion.

6.4.1 Introduction.

Cesium resonances in aqueous solution were measured to determine more accurately than before the concentration dependence of the shift due to the counter-ion, particularly at low concentrations. This was made possible through the use of the spectrometer described in chapter 4. The high field strength (50 kilogauss) increased the magnitude of the chemical shifts; the exceptional field stability permitted the attainment of very reproducible results; and through the use of a C.A.T. very low concentrations were observed.

Previous measurements (9) are reported as having a linear dependence of the shift with concentration (Molality) at concentrations above 4M and a linear dependence with activity at concentrations $< 4M$. The measurements made by the author shown in figures 6.2-6.5 do not show a linear dependence with concentration over any portion of the concentration range, up to the limits of solubility at 25°C. The concentrations were also converted to activities using tabulated activity coefficients (51). The correlation of the shift with activity is shown in figure 6.7. There appears to be a linear dependence with activity but only at low concentrations, $< 0.4M$.

In the course of attempting to find some explanation for the overall concentration dependence, it was discovered that the chemical shift depended linearly on the 0.8 power of the concentration. All the salts

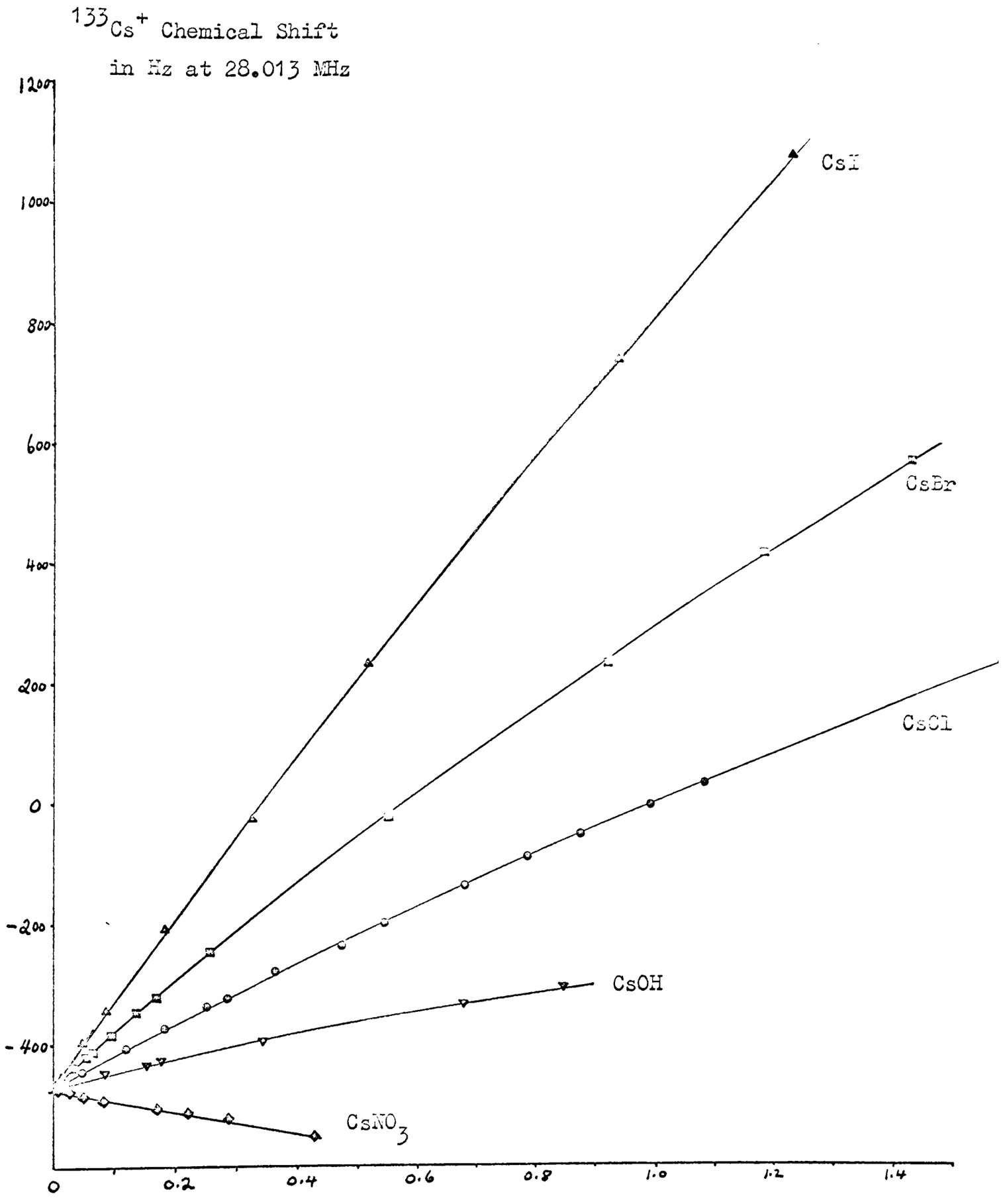


Figure 6.7 $^{133}Cs^+$ Chemical shifts vs Activity

measured give reasonably straight lines on a log-log plot of chemical shift (referenced to infinite dilution) vs. concentration (molality) with approximately 0.8 slope.

This observation started a new attack on a theory to explain the chemical shift in solution. Dr. R.R. Sharp proposed the theory described in chapter 5 and made calculations based on it for the cesium ion shifts, as a function of concentration, temperature, and dielectric constant.

6.4.2. Predictions of the proposed theory for ion-ion contribution to the chemical shift.

It is worth considering here the results obtained with this theory. The absolute shifts calculated for the three mechanisms proposed for the production of the chemical shift, i.e. ion-induced dipole, Van der Waals, and overlap, are shown in figure 6.8. It can readily be seen that even with an overestimation of the ion-induced dipole and Van der Waals interactions (due to the assumption that $\mathcal{E} = 1$ in the first hydration sphere) they are still several orders of magnitude smaller than the overlap contribution. Therefore the overlap mechanism is assumed predominant for the production of cesium ion shifts and all calculations are based on this. For the smaller ions though the other forces may become more important.

The magnitude of the calculated shifts is low by a factor of approximately 2 but considering the assumptions that have been made this agreement is quite good. The value assumed for the distance of closest

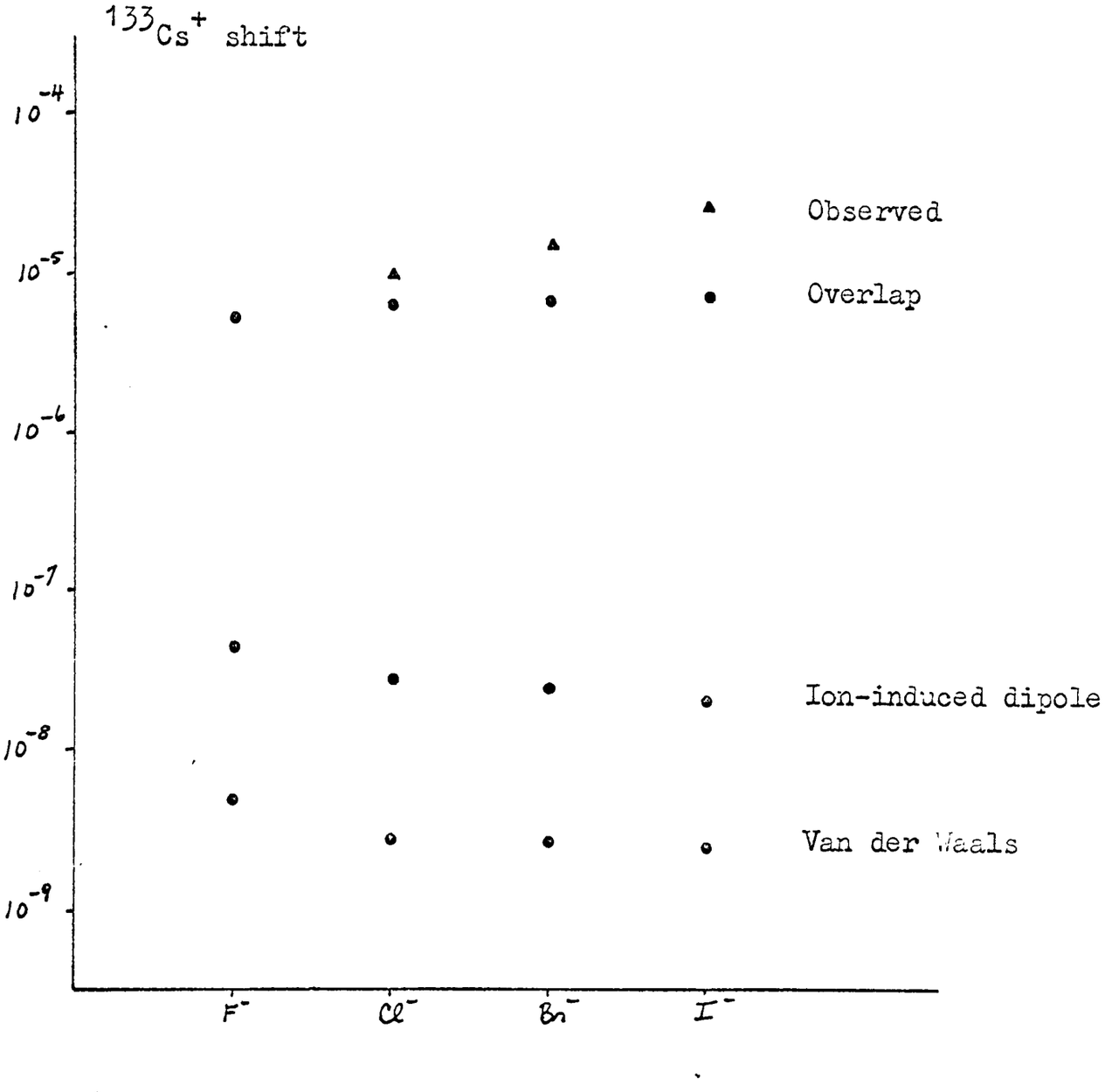


Figure 6.8 Calculated ion-ion shifts of $^{133}Cs^+ X^-$ for the mechanisms proposed.

approach is quite important. The effect of varying this distance from 3.4Å to 3.8Å for CsBr is illustrated in figure 6.9 and Table 6.1 shows the effect this has on the slope of the log shift vs. log concentration plot.

Table 6.1

Change of slope of log-log correlation of shift vs. concentration with distance of closest approach.

Distance of closest approach	slope
3.4	0.7910
3.6	0.8002
3.8	0.8068

Therefore, although the absolute magnitude of the shift may be in error the slope of the log-log correlation should be predicted quite accurately.

Since these calculations are based on concentration units of moles/litre of solution (molarity) the concentrations of the cesium salts used were converted from molality to molarity by the use of densities obtained in the International Critical tables (55).

A plot of the theoretical and observed shifts for CsBr and CsCl is shown in figure 6.10 (the calculated shifts are normalized to the observed ones). The slope is quite well predicted except at high concentrations where an upward deviation can be noted for the measured shifts. Calculations of the Cs^{*}-Cs^{+} interactions in solution indicate a much more sharply rising line than for Cs^{+}-X^{-} interactions at high concentrations. These like-ion interactions may account in part for

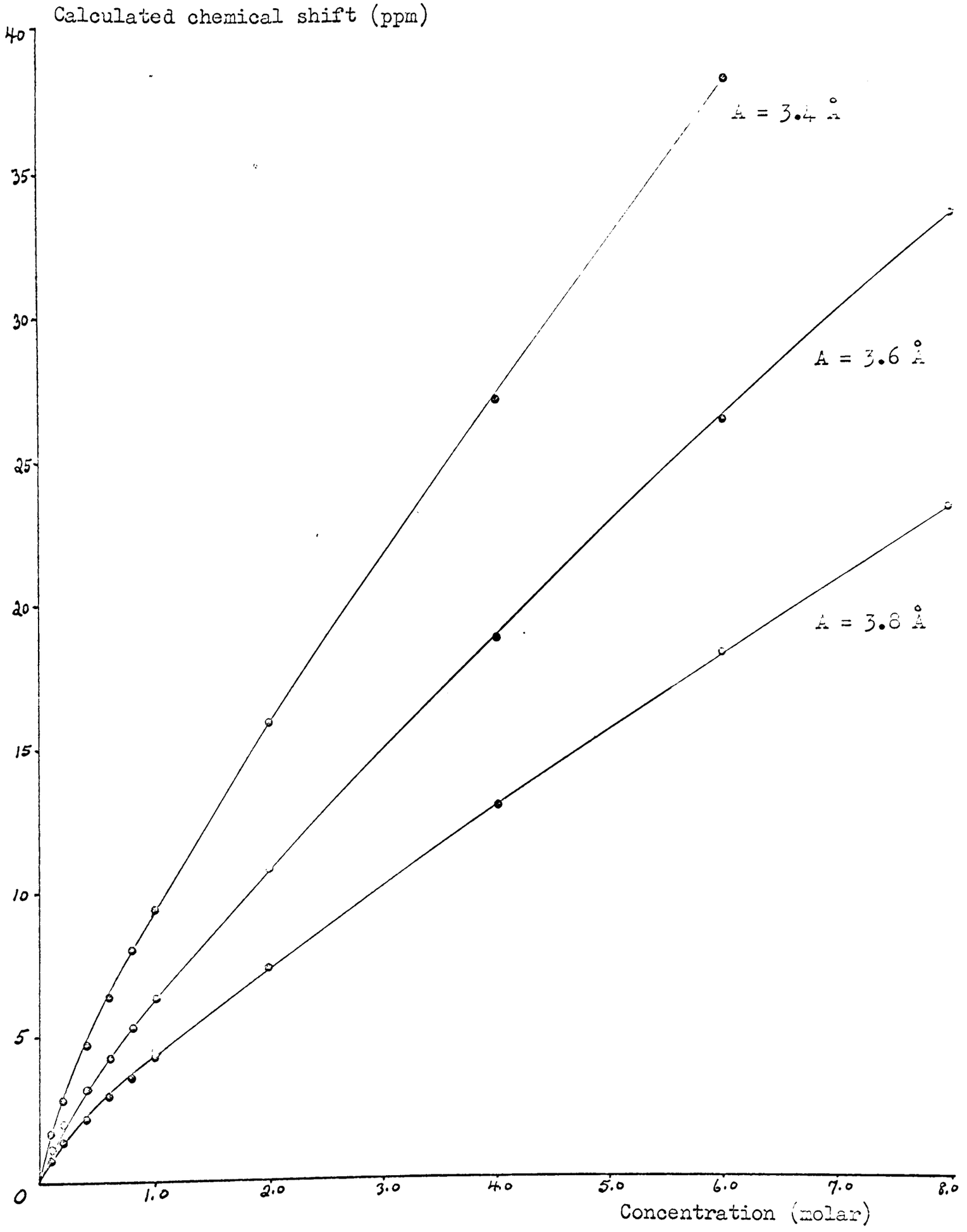


Figure 6.9 Calculated shifts for $CsBr/H_2O$ as a function of distance of closest approach.

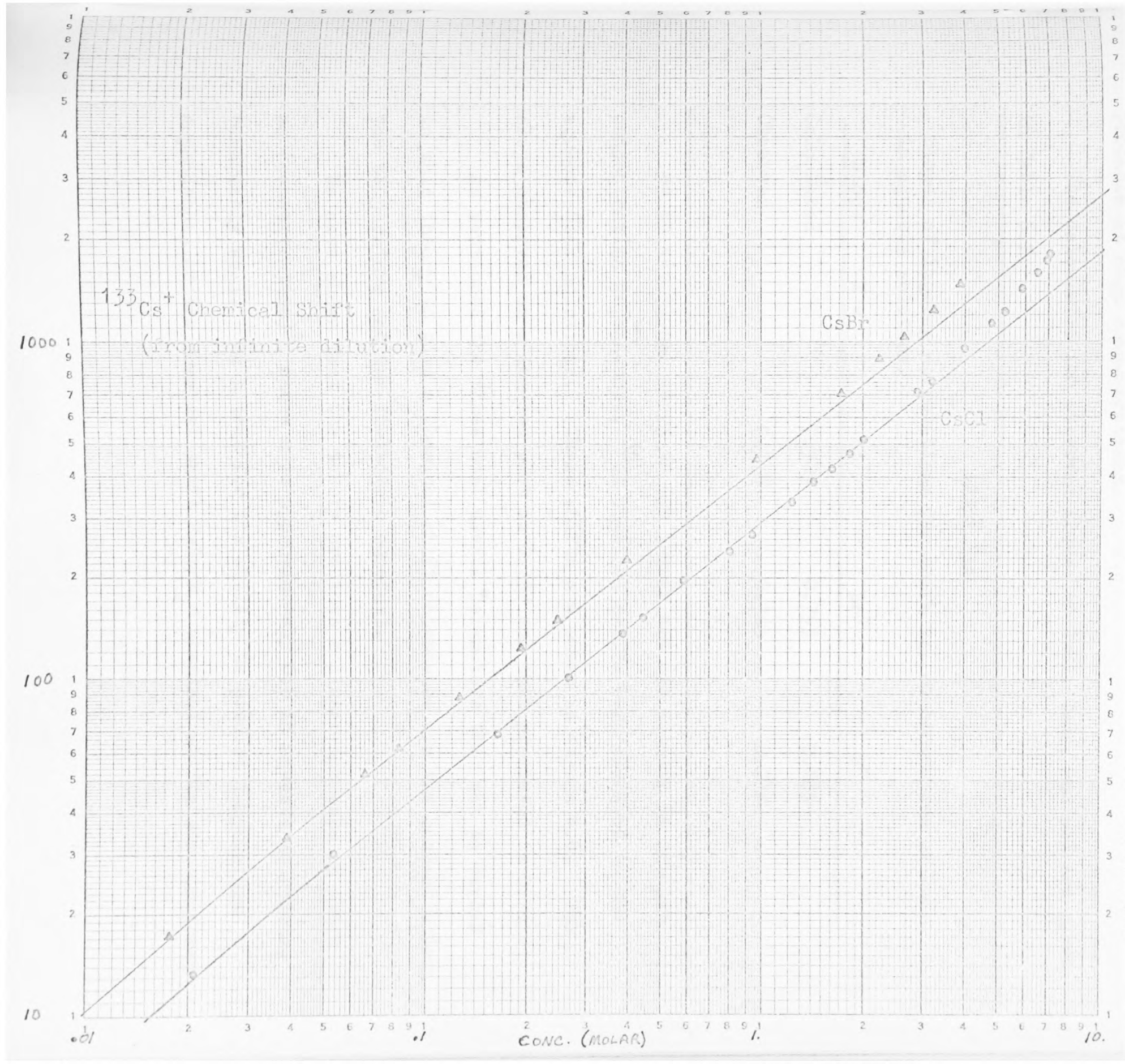


Figure 6.10

Calculated (continuous line) and experimental points for the cesium chemical shift in CsCl and CsBr aqueous solutions.

the deviation at high concentration. Another factor to take into account is that the theory assumes a binary interaction causing the shift. It will not hold for ternary interactions which become more probable at high concentrations.

The calculated and observed slopes of CsCl, CsBr, and CsI are given in Table 6.2.

Table 6.2

Slopes of log-log correlations for shift vs. concentration of CsX in aqueous solution.

Slope	X =	Cl^-	Br^-	I^-
Calculated		0.785	0.793	0.803
Observed		0.778	0.783	0.778

As an additional check on the theory and its ability to predict concentration dependences, ^{35}Cl chemical shifts were measured in the aqueous CsCl solutions. These shifts are shown in figure 6.6. The slope observed on a log-log plot is 0.757 and that predicted is 0.785.

As mentioned the three most useful parameters that can be varied in this theory to give a chemical shift dependence are the concentration, the temperature and the dielectric constant.

We have shown that the theory predicts a linear increase in shift as $(\text{concentration})^n$, where n is approximately 0.8 in aqueous solutions, remarkably well. As a test for its ability to predict temperature dependences of the chemical shift $CsBr/H_2O$ chemical shifts were measured

at 59.3°C and 89.5°C. The results are given in Table 6.3.

Table 6.3

Temperature Effects on Chemical Shifts of $CsBr/H_2O$.

Temperature °K	Shift at 0.1 molar (from infinite dilution)		Slope	
	Observed (ppm)	Calculated(ppm)	Observed(ppm)	Calculated(p.
278.0	[illegible]	1.03	-	.772
298.0	2.56	1.06	.783	.785
318.0	-	1.09	-	.798
332.3	2.56	1.11	.783	.806
362.5	2.67	1.17	.788	.820

The observed results show a slight trend in the direction of the calculated temperature dependence but it is not as great as predicted. However H_2O is a poor choice for a test of the temperature dependence since T occurs in the formula as εT and for H_2O this is nearly constant in the range 278°K to 362.5°K (see Table 6.4) so very little effect is to be expected.

Table 6.4

Variation of εT with increasing temperature for H_2O

Temperature °K	ε	εT
278.0	86.107	23938.
298.0	78.540	23405.
318.0	71.721	22807.
332.3	67.304	22365.
362.5	59.232	21472.

The large diamagnetic shift of the cesium ion with an increase in temperature (figure 6.5) can be explained by assuming that the statistical orientation of the oxygen atom of the water towards the cesium ion becomes smaller with an increase in temperature due to increased thermal motion. This reduces the overlap contribution from the oxygen atom contributing to the ion-solvent shift (assuming that the hydrogen atoms have a very small effect) producing the observed diamagnetic shift.

The effect of varying the dielectric constant will be discussed in chapter 7.

6.4.3 Solvent isotope effects.

During the course of the measurements of cesium shifts in aqueous solution the effect on the shift of varying the isotopic composition of the water was measured. The results of these measurements, presentedin figures 6.3 and 6.4 throw new light on the mechanism of the isotope shift. Measurements made by Lŏwenstein(43) on 1.0 and 0.5M solutions of CsCl in D_2O and $H_2{}^{18}O$ gave:

Table 6.5 from (43)

Concentration CsCl(Molar)	$(D_2O - H_2O)_{ppm}$	$(H_2{}^{18}O - H_2O)_{ppm}$
1.0	1.5 ± 0.2	0.8 ± 0.4
0.5	1.2 ± 0.2	-

The mechanism suggested for these shifts involves alterations in the interactions between the ions and their hydration spheres by the changes in molecular vibrational amplitudes caused by isotopic substitution. On this basis if there are no gross differences in the orientations of solvent molecules relative to different ions, the isotope shifts would be expected to be nearly constant fraction of the total aqueous solution shifts.

The author's results, measured over a wide concentration range (0.01 to 7 molar) do not fit this theory. At high concentrations on a molar concentration scale the shifts observed in H_2O, D_2O, and $H_2{}^{18}O$ converge above 4 molar (figure 6.11). At infinite dilution the $H_2{}^{18}O$ gives no isotope shift relative to H_2O but D_2O gives ~1ppm shift to high field (figure 6.4b). This infinite dilution shift was determined at 3 temperatures, 25°, 59.3°, and 89.5°C and found to be unchanged within experimental error. The slight trend towards a reduction in the shift, ~2Hz, is too small to place any reliance on. These results would suggest that a mass effect is not the source of the shift since $H_2{}^{18}O$ and D_2O have the same mass but give different isotope shifts and $H_2{}^{16}O$ and $H_2{}^{18}O$ have different masses but give the same shift.

The most likely explanation for the isotope effect at infinite dilution, since here it is strictly an ion-solvent effect, is that the overlap from the oxygen on the water molecules adjacent to the cesium ion is modified by changes in the solvent hydrogen bonds in passing

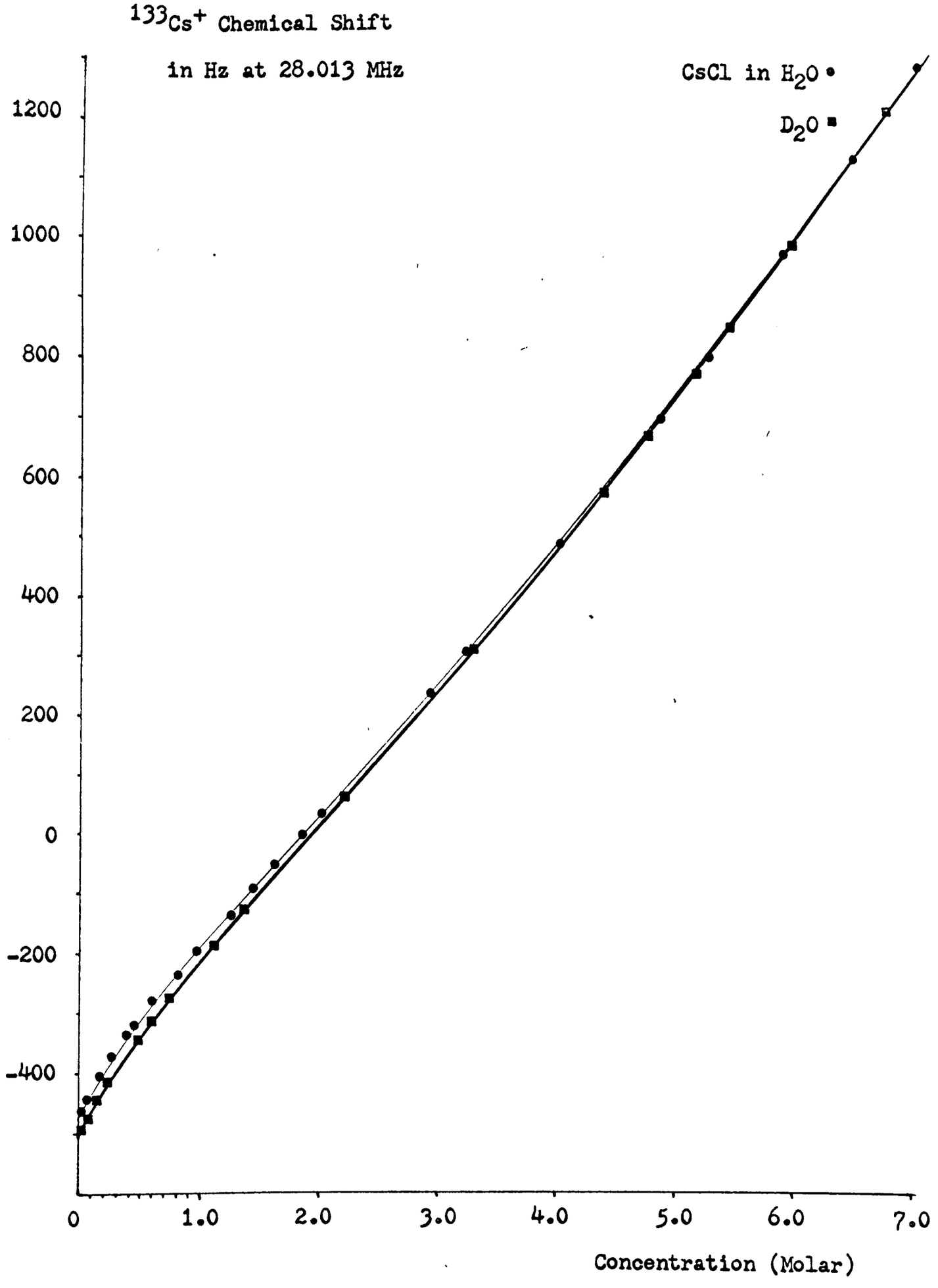


Figure 6.11 $^{133}Cs^+$ Chemical shifts vs Concentration (Molar) of CsCl in H_2O and D_2O

from H_2O to D_2O. The O-D hydrogen bonds are stronger (52) and thus reduce slightly the oxygen atom density about the cesium ion since the solvent is more structured. This reduces overlap causing a diamagnetic shift to be observed.

This theory also explains the convergence of the D_2O and H_2O lines at higher concentrations. Since cesium is a structure breaking ion the hydrogen bonding in the D_2O will be reduced upon the addition of cesium ions. Thus the oxygen atoms in the D_2O will become more available the greater the cesium concentration and eventually at ~ 4 molar have the same degree of overlap with the cesium as H_2O. The $H_2{}^{18}O$ shifts follow the $H_2{}^{16}O$ shifts since the electronic structures of ^{18}O and ^{16}O are the same.

Although this chapter purports to describe the aqueous solutions studied the measurements made in methanol, methanol-d_1, and methanol-d_4 are best described here. Figure 6.12 shows the shifts measured and figure 6.13 shows a plot of the shifts vs. the $\sqrt{\text{conc.}}$ This is linear for reasons that will be explained in the next chapter. For these three solutions there is no isotope shift within experimental error at infinite dilution. The sharp curvature of the concentration plot makes extrapolation to infinite dilution very imprecise, although concentrations as low as 0.005M were measured. The infinite dilution point chosen was taken from the square root of the concentration plot since this gave a linear relationship with shift. It is on the basis

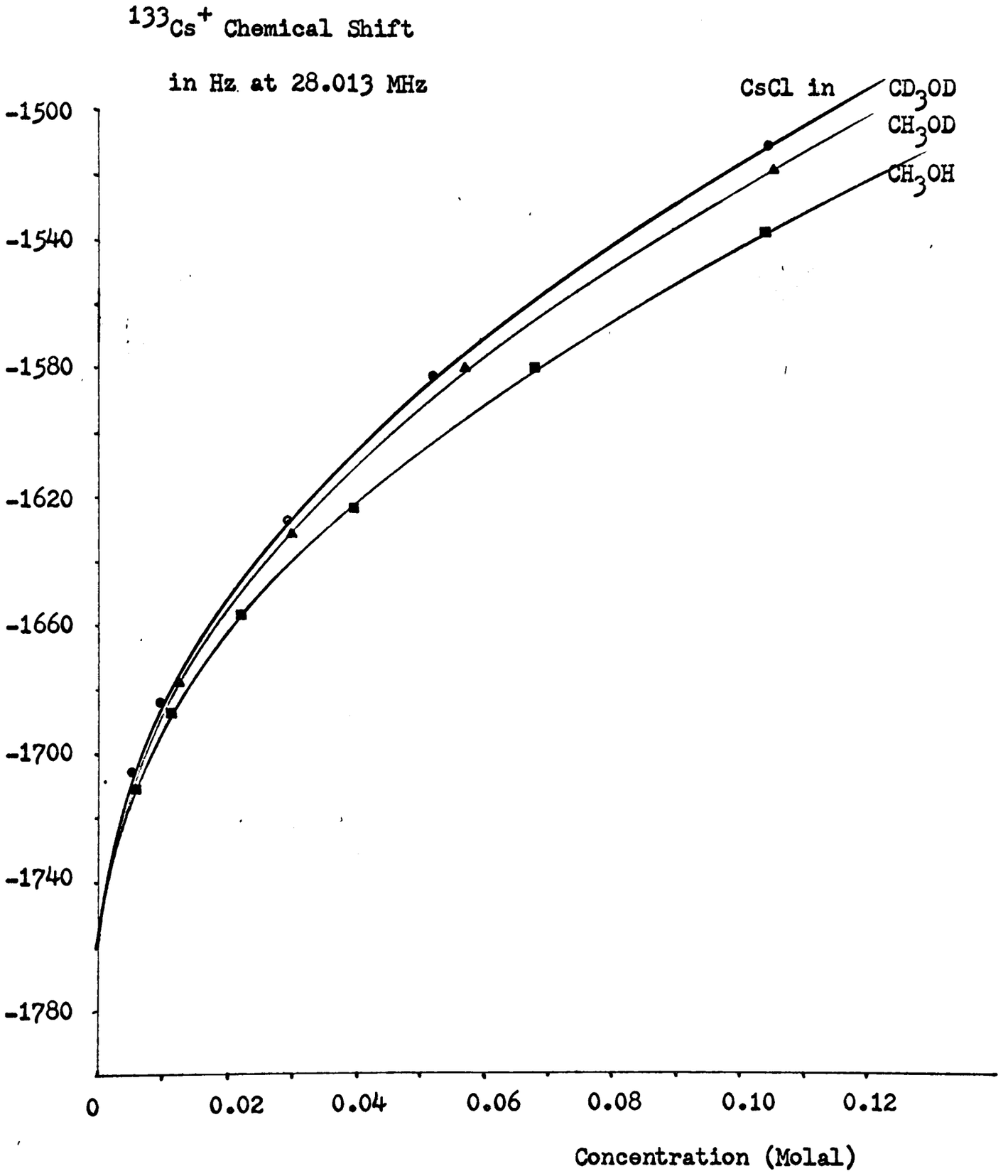


Figure 6.12 $^{133}Cs^{+}$ Chemical shifts of CsCl in CH_3OH, CH_3OD, CD_3OD vs Concentration (Molal)

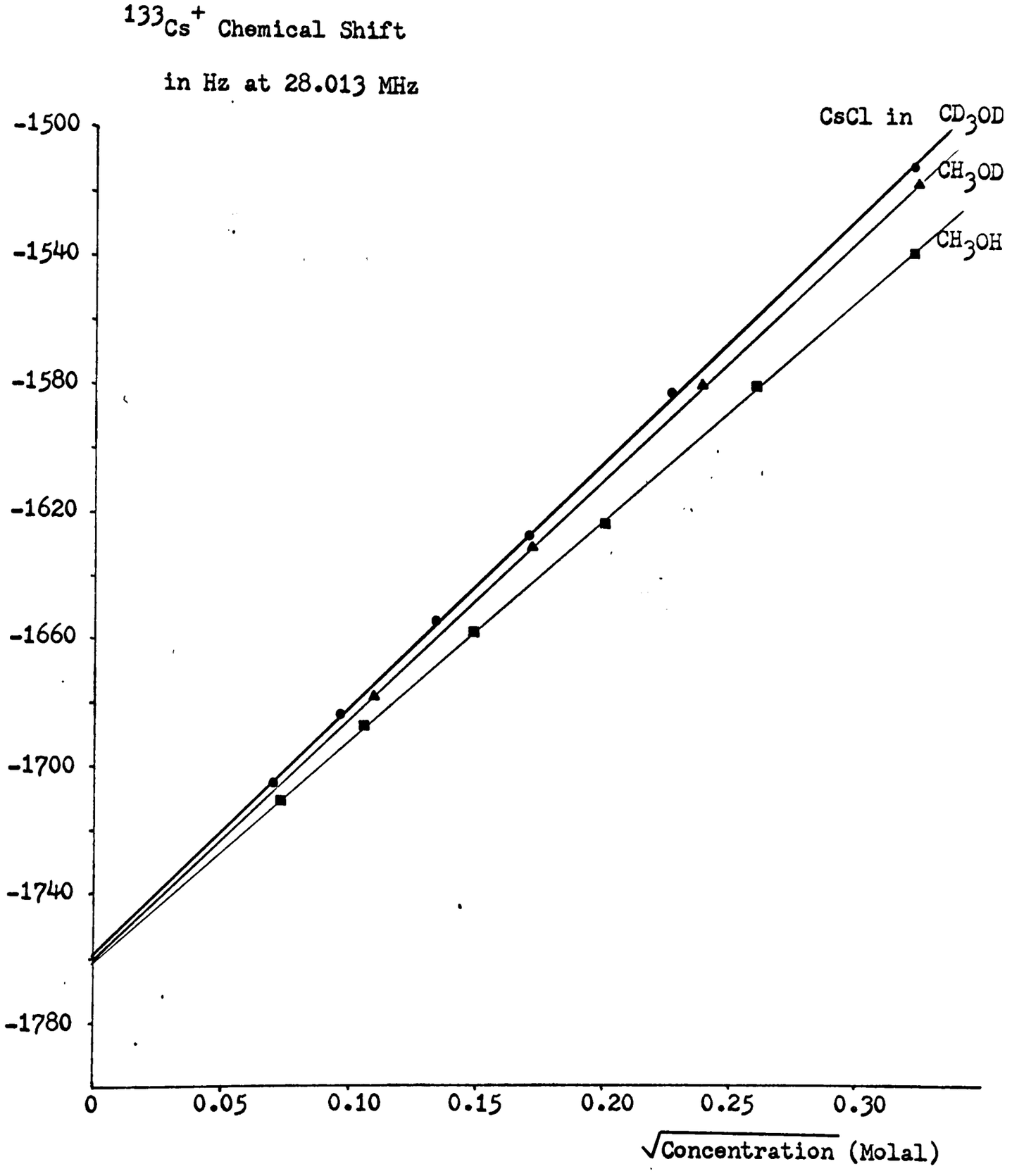


Figure 6.13 $^{133}Cs^{+}$ Chemical shifts of CsCl in CH_3OH, CH_3OD, CD_3OD vs $\sqrt{\text{Concentration}}$ (Molal)

of this plot that it is stated that there is no isotope shift at infinite dilution. Very little can be said about the apparent divergence of the lines in figures 6.12 and 6.13 since the concentrations are expressed in molality. The required densities of CsCl/MeOH solutions to convert these molalities to molarities are not available.

We shall next turn to the measurement of cesium chemical shifts in chapter 7. Here the theory for the chemical shift in solution proposed is further tested by the variation of the dielectric constant of the media.

Chapter 7. $^{133}Cs^+$ Chemical Shifts in mixed and non-aqueous solvents.

7.1 Introduction.

There have been remarkably few investigations into the effect of solvent on the chemical shift of the larger alkali metal ions. Among those the sensitivity of the chemical shift to solvent has been stated to decrease rapidly as ionic size increases (*53*) and for cesium the shift is practically unaffected (*54*). However, recent shifts of cesium in H_2O/D_2O have indicated a diamagnetic shift of 1.5ppm in 1 molar CsCl in D_2O with respect to H_2O (*43*). These measurements agree qualitatively with the shifts in H_2O/D_2O measured by the author and quoted in chapter 6.

It is clear from this that shifts of cesium in various organic solvents are not well documented and, while perhaps small, should be measurable. These shifts may be able to provide information on ion-solvent interactions.

7.2 Experimental.

There are many difficulties encountered in the measurement of chemical shifts of $^{133}Cs^+$ in organic solvents, the main one being solubility. To measure the chemical shift in a range of solvents with the same cesium ion concentration, this could not be greater than 0.1M. The solvents used are listed in section 7.2.1. A more detailed concentration dependence study was undertaken in selected solvents (methanol, ethanol, 1,2-ethanediol, 1,2,3-propanetriol, pyridine, and tetrahydrothiophen-1,1-dioxide). The effect of glycine on the shift was also measured.

To prevent any changes in concentration due to evaporation each sample was sealed immediately after preparation. This was accomplished by first freezing the sample in liquid nitrogen then sealing off the end of the bulb.

The shifts were measured at 25±0.1°C and referenced to an external standard of 1.994M $CsCl/H_2O$.

7.2.1 Solvents.

Solvent	Grade	Source	Preparation or Purification
methanol	Analar	Hopkins & Williams	Dried by repeated distillations.
methanol-d_1	-	-	The author would like to acknowledge Mr. C. Hall for the preparation of this solvent by repeated distillation of CH_3OH from D_2O. An ^1H n.m.r. spectrum showed < 1% H on the OH.
methanol-d_4	99.5 atom %D	Ciba	This sample, 5 gms, was used without further purification.
ethanol	Absolute	Distillers	
1-propanol	R	B.D.H.	
2-propanol	Analar	B.D.H.	
2-methyl-2-propanol	R	B.D.H.	
1,2-ethanediol	R	Griffin & George	
1,2,3-propanetriol	Analar	B.D.H.	

Solvent	Grade	Source	Preparation or Purification
formic acid	Analar	B.D.H.	
acetic acid	Analar	Fisons	
formaldehyde (36% w/v)	Analar	B.D.H	
formamide	R	B.D.H.	
hydrogen peroxide(100 volume)	R	May & Baker	
hydrazine hydrate	R	-	
methyl sulfinyl methane (dimethyl sulphoxide)	R	B.D.H.	
tetrahydrothiophen-1,1-dioxide (sulpholane)	R	B.D.H.	Purified and dried by twice distilling under vacuum from CaH.
pyridine	Analar	B.D.H.	

Acetone, acetylacetone, acetonitrile, triethylamine, dimethylformamide, 1,4-dioxane, and methylformate were tried but 0.1M CsCl solutions could not be prepared.

7.2.2 Salts.

CsCl was used throughout these measurements except for several instances when CsI had to be employed because of solubility difficulties. The salts used had the same purities as previously quoted.

7.3 Results.

The chemical shifts measured for 0.1M CsCl in a range of mixed aqueous and pure organic solvents are illustrated in figure 7.1. The wide range of shifts observed, ~120ppm, is quite startling, since it was expected from literature data (53,54) that any shifts present would be small.

The results of the concentration dependence measurements in mixed aqueous and pure methanol, ethanol, 1,2-ethanediol, 1,2,3-propanetriol, pyridine, and tetrahydrothiophen-1,1-dioxide are shown in figures 7.2, 7.3 and 7.4. The chemical shifts measured in the isotopically substituted methanols, CD_3OD and CH_3OD have already been presented and discussed in chapter 6.

7.4 Discussion.

The range of chemical shifts discovered for $^{133}Cs^+$ in solvents other than water is quite large (Figure 7.1). The ~120ppm shift is comparable in magnitude with the ion-ion shifts measured in water and shows quite conclusively that ion-solvent interactions are important. However there does not seem to be any correlation of the shift with bulk properties of the solvents. It is worth noting though that there seem to be the following trends:

1) In each of the series, alcohol and acid, the shift becomes more paramagnetic as the molecular weight of the alcohol or acid increases,

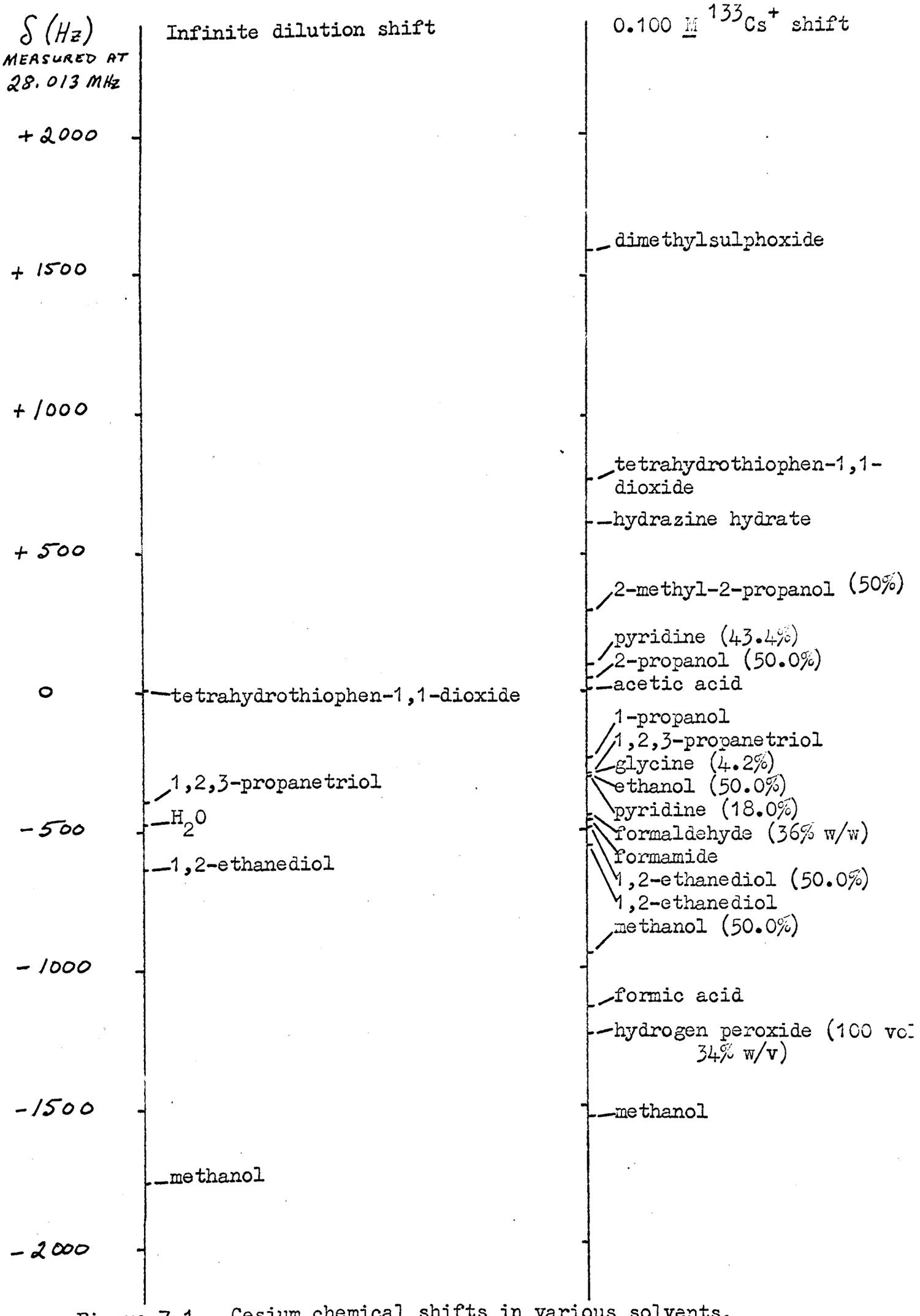


Figure 7.1 Cesium chemical shifts in various solvents.

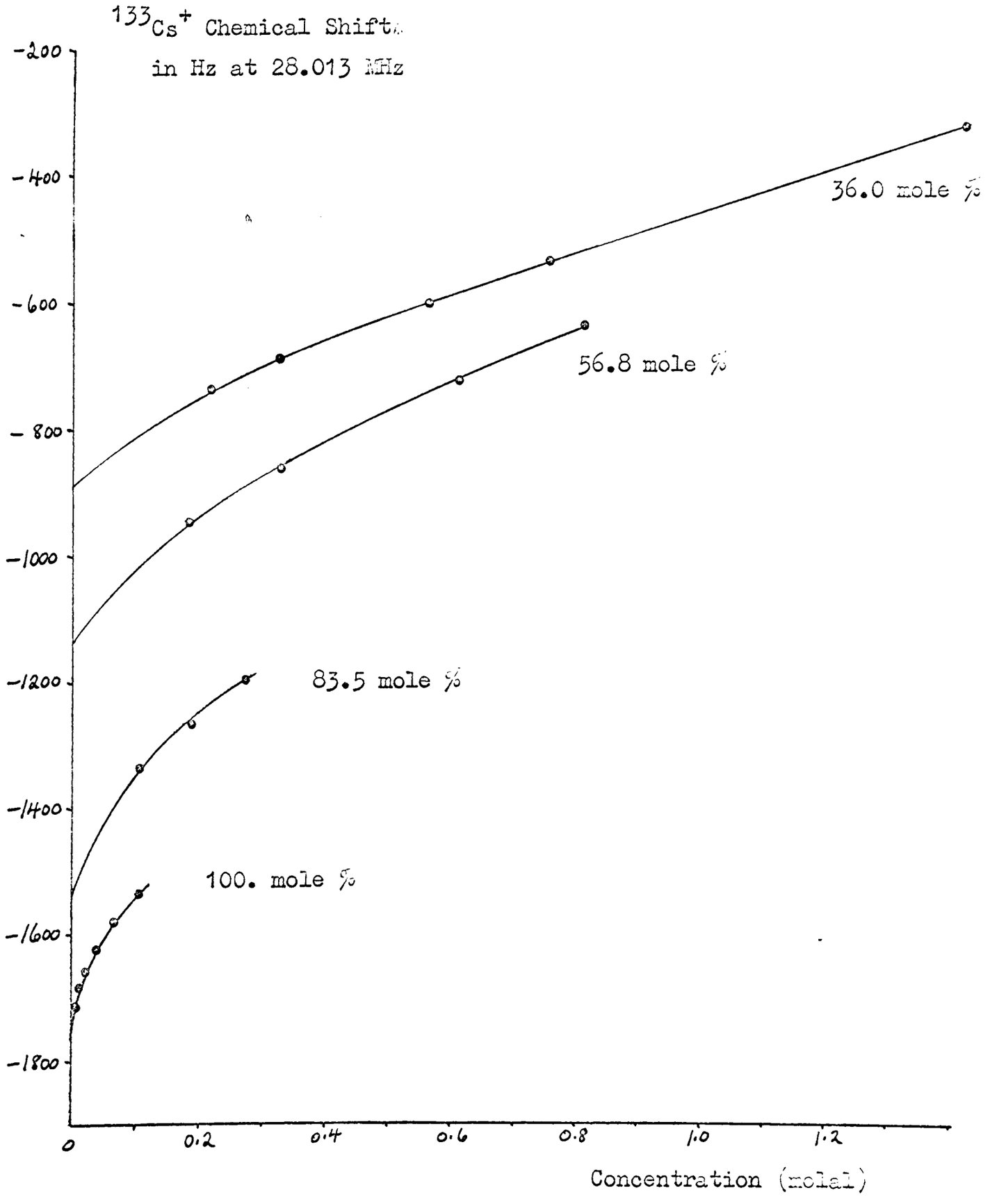


Figure 7.2 $^{133}Cs^+$ Chemical shift vs Concentration of CsCl in indicated mole % methanol/H_2O solutions.

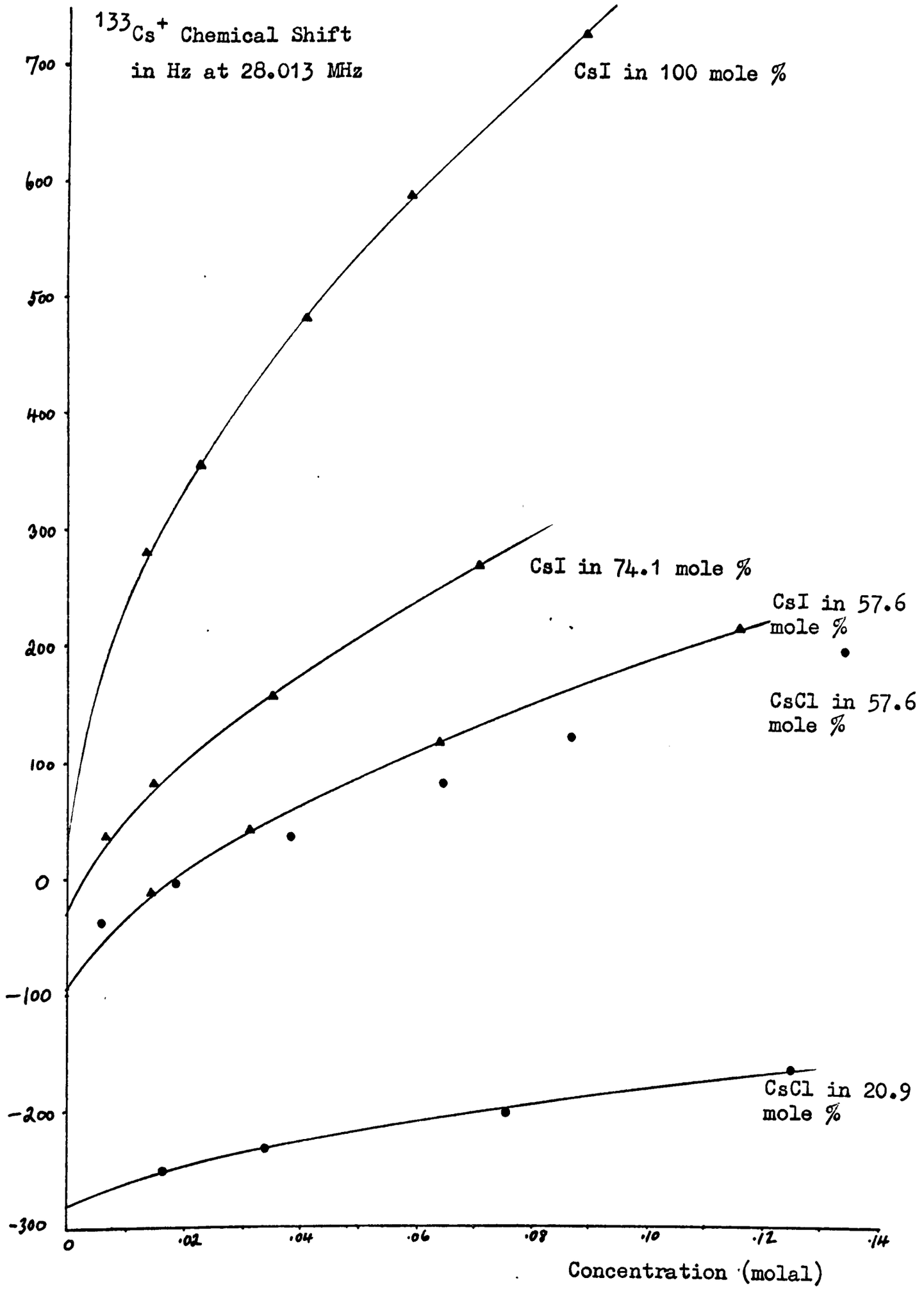


Figure 7.3 $^{133}Cs^+$ Chemical shift vs Concentration of CsI and CsCl in indicated mole % of tetrahydrothiophen-1,1-dioxide/H_2O solutions.

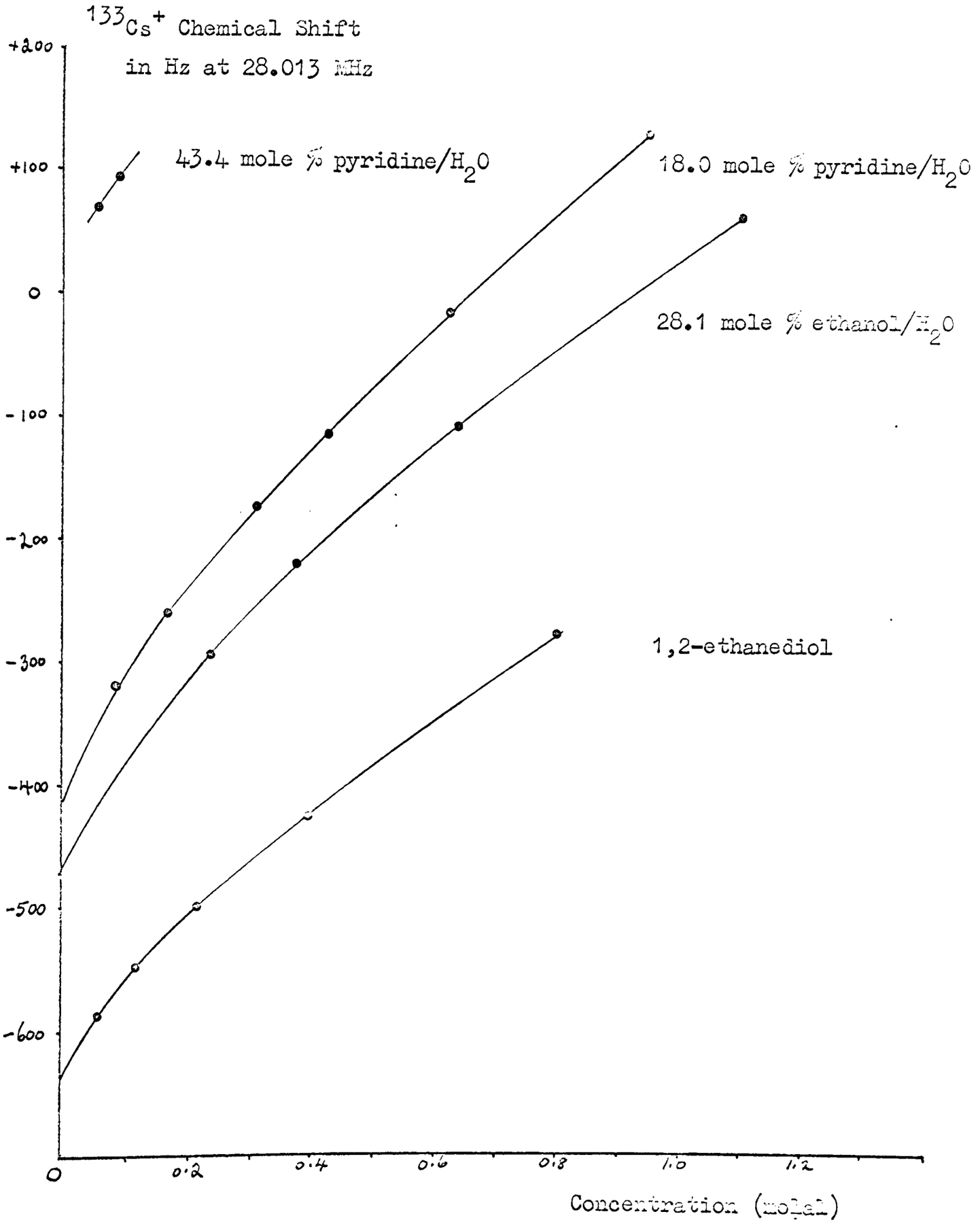


Figure 7.4a $^{133}Cs^+$ Chemical shift vs Concentration of CsCl in indicated solvents.

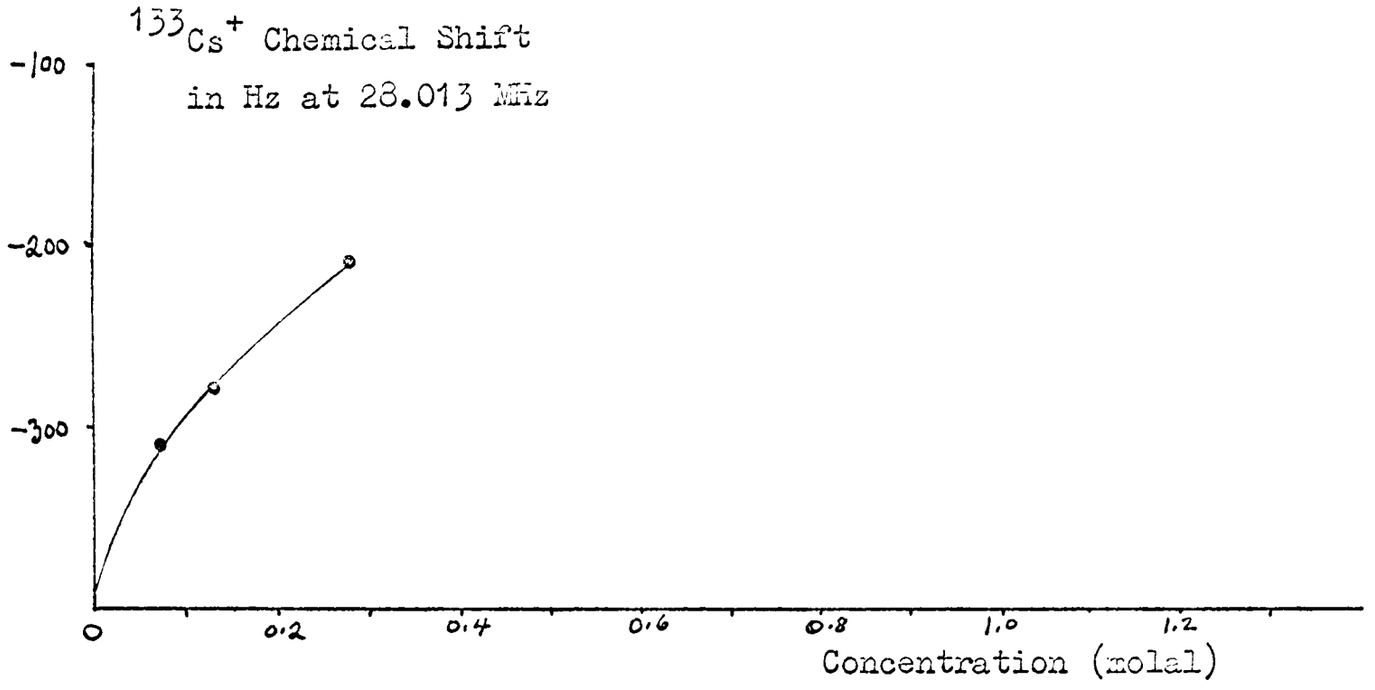


Figure 7.4b $^{133}Cs^+$ Chemical shift vs Concentration of CsCl in 1,2,3-propanetriol

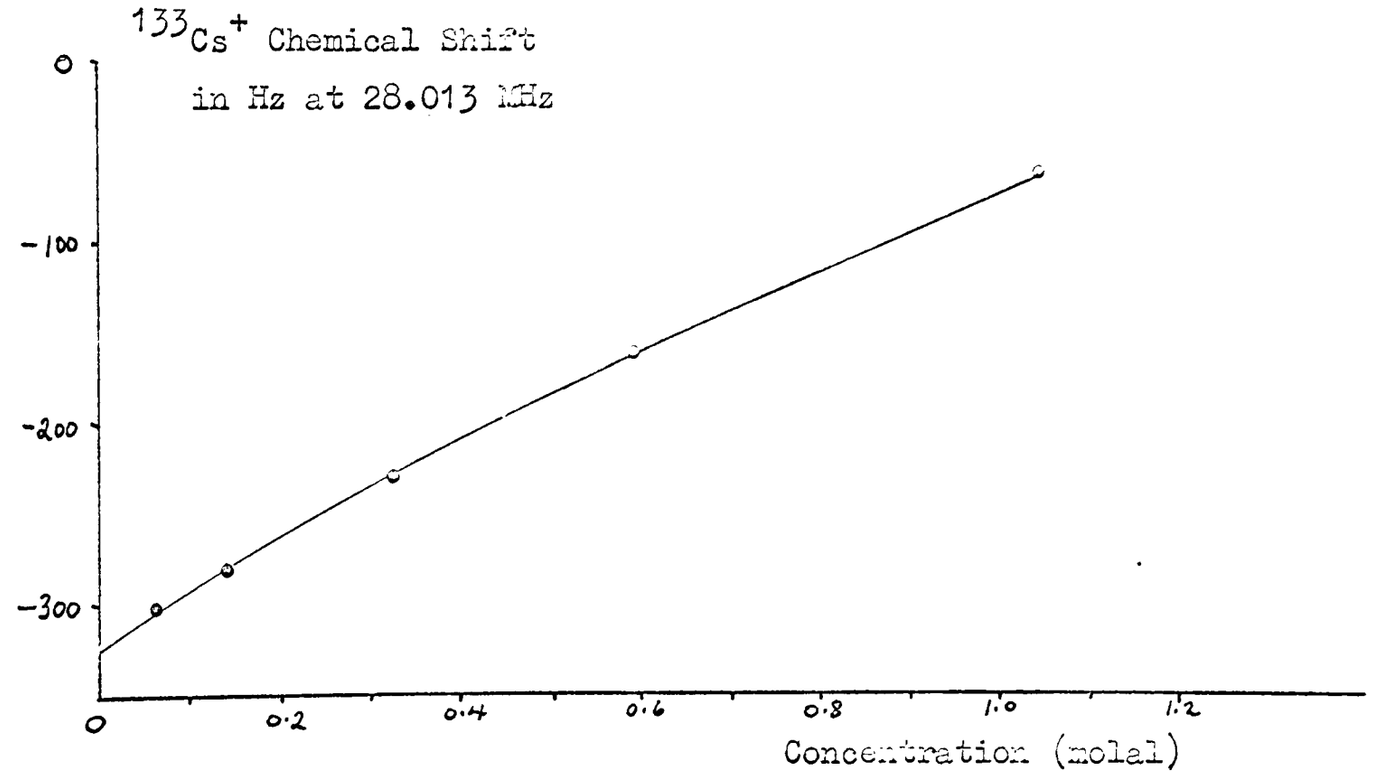


Figure 7.4c $^{133}Cs^+$ Chemical shift vs Concentration of CsCl in 4.19 mole % glycine/H_2O

and in the case of isomers, the shift is more paramagnetic for the bulkier isomer.

2) The two solvents giving the largest paramagnetic shifts relative to 0.1M $CsCl/H_2O$ are tetrahydrothiophen-1,1-dioxide and dimethyl sulphoxide, both with sulphur atoms attached to the oxygen.

A more detailed dependence of the shift of 0.1M CsCl on the composition of the solvent (for the series of alcohols from methanol to 2-methyl-2-propanol) is shown in figure 7.5.

The shift becomes more paramagnetic with increasing molecular weight. An interesting observation is that the shift for ethanol and 1-propanol are not significantly different while there is a considerable increase on going to the isomer 2-propanol.

If overlap of the cesium ion with the oxygen of the alcohol is considered as the shift producing mechanism then the degree of overlap must increase on going from methanol to 2-methyl-2-propanol to give the observed shifts. This increase in overlap could be caused by

1) the increased electron density on the oxygen going through the series methanol, ethanol, 1-propanol, 2-propanol, 2-methyl-2-propanol.

and/or 2) Steric effects may play a part.

Further studies were carried out on the effect of different solvents on the ion-ion shifts. As can be seen from figures 7.2, 7.3, and 7.4 these are quite pronounced. There is an enhancement of the magnitude of the chemical shift from infinite dilution with respect to

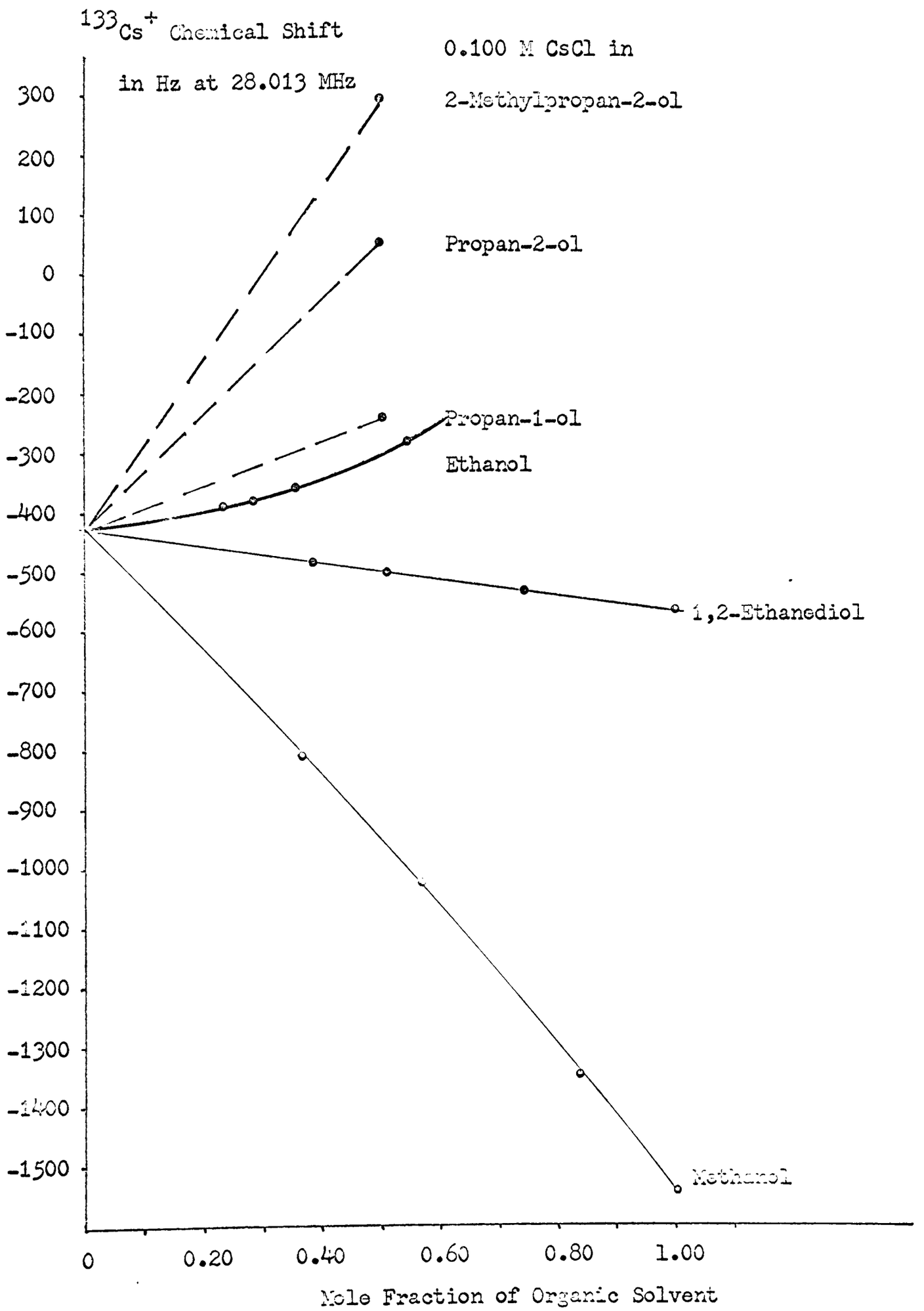


Figure 7.5 $^{133}Cs^+$ Chemical shifts of 0.100 M CsCl in alcohol/H_2O solutions vs Mole fraction of alcohol

that observed from infinite dilution in water and also a large change in n where n is the power the concentration is raised to, to give a linear relation with the shift. These results are tabulated in Table 7.1.

Table 7.1

Mole fraction	Solvent	$\mathcal{E}$	Shift of 0.1M $^{133}Cs^+$ from infinite dilution (Hz)	(ppm)	n
1.000	H_2O	78.54	48.6	1.73	
1.000	Methanol	32.6	215	7.68	0.494
0.835	"	36.4	190	6.78	0.510
0.568	"	45.2	121	4.32	0.634
0.360	"	55.0	80	2.86	0.690
0.281	Ethanol	49.0	84	3.00	0.714
1.000	1,2-ethanediol	37.7	78	2.78	0.712
1.000	1,2,3-propanetriol	42.5	103	3.67	0.557
0.180	Pyridine	45.6	107	3.82	0.718
0.042	Glycine/H_2O	132	34	1.21	0.896

These results produced much speculation initially since there were such varied effects. However, with the advent of Dr. R.R. Sharp's theory an explanation became available.

The theory proposed, initially for water, can be applied to any solvent since the Debye-Huckel potential in the Boltzmann distribution $n'(R,c)$ considers the solvent as a dielectric continuum. So a

different solvent can be allowed for by a change in the bulk dielectric constant.

Figure 7.6 shows the calculated change in n (continuous line) with changing dielectric constant for CsI and CsCl. The labeled points are the observed values for n. There is a very good correlation between the calculated and observed values, even for the CsCl/glycine/H_2O solutions. Glycine was used since it raises the dielectric constant of water.

Figure 7.7 shows the calculated shifts from infinite dilution for 0.1 molar solutions of CsCl (continuous line). The observed shifts are plotted on the same graph but the scale has been reduced by a factor of two. Once again the trend predicted by the theory is followed. The molar increments in the shift increase as the dielectric constant is lowered (methanol) and decrease when it is raised (glycine/H_2O).

That the proposed theory can predict the behaviour of the chemical shift over such a wide range of solvents is strong evidence for its validity. Further work is being done to improve the theory by the inclusion of more accurate distribution functions and also more experiments are contemplated to check its compatibility under different conditions.

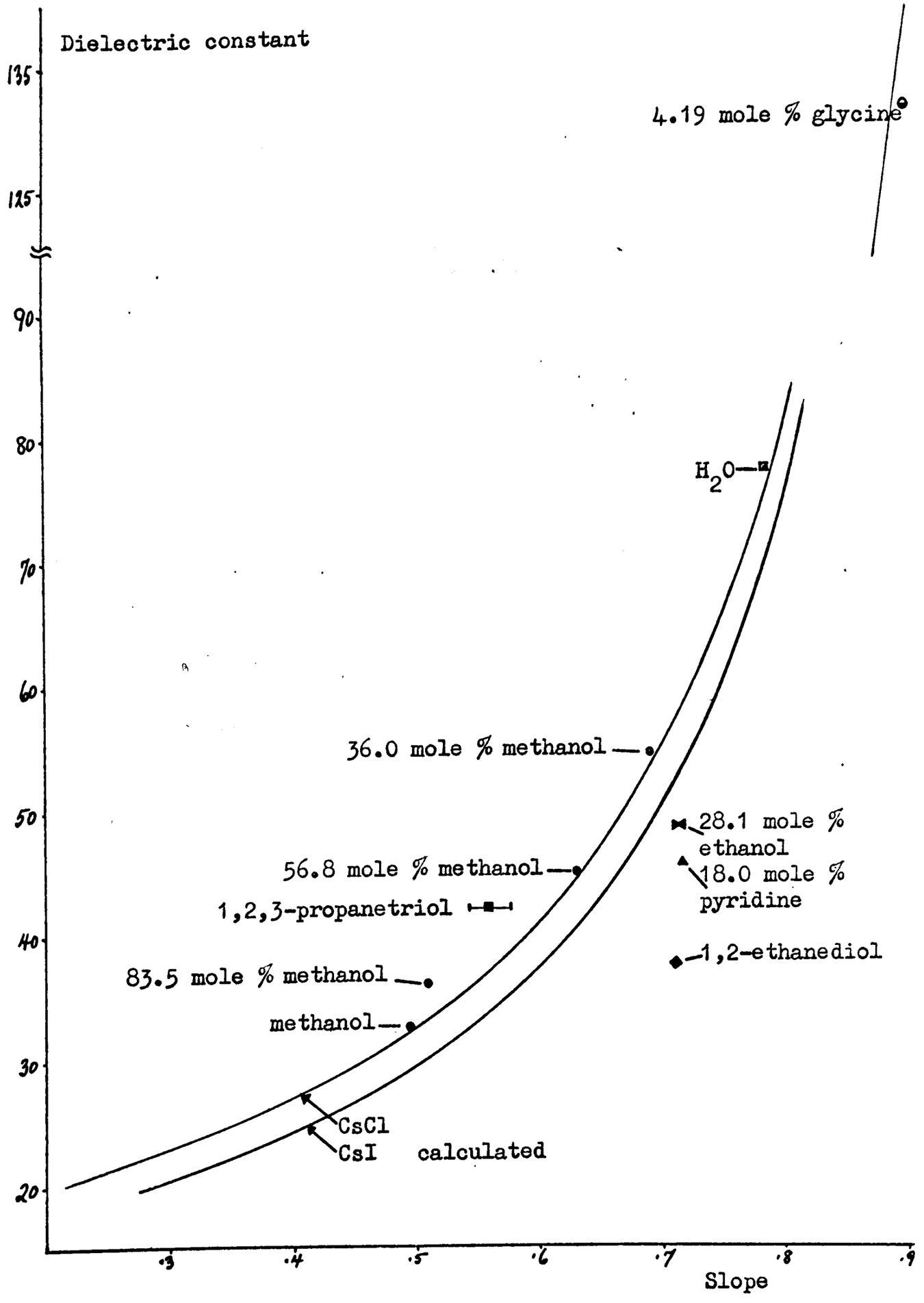


Figure 7.6 Change of slope (of log-log graph of chemical shift vs concentration) vs dielectric constant of solvent.

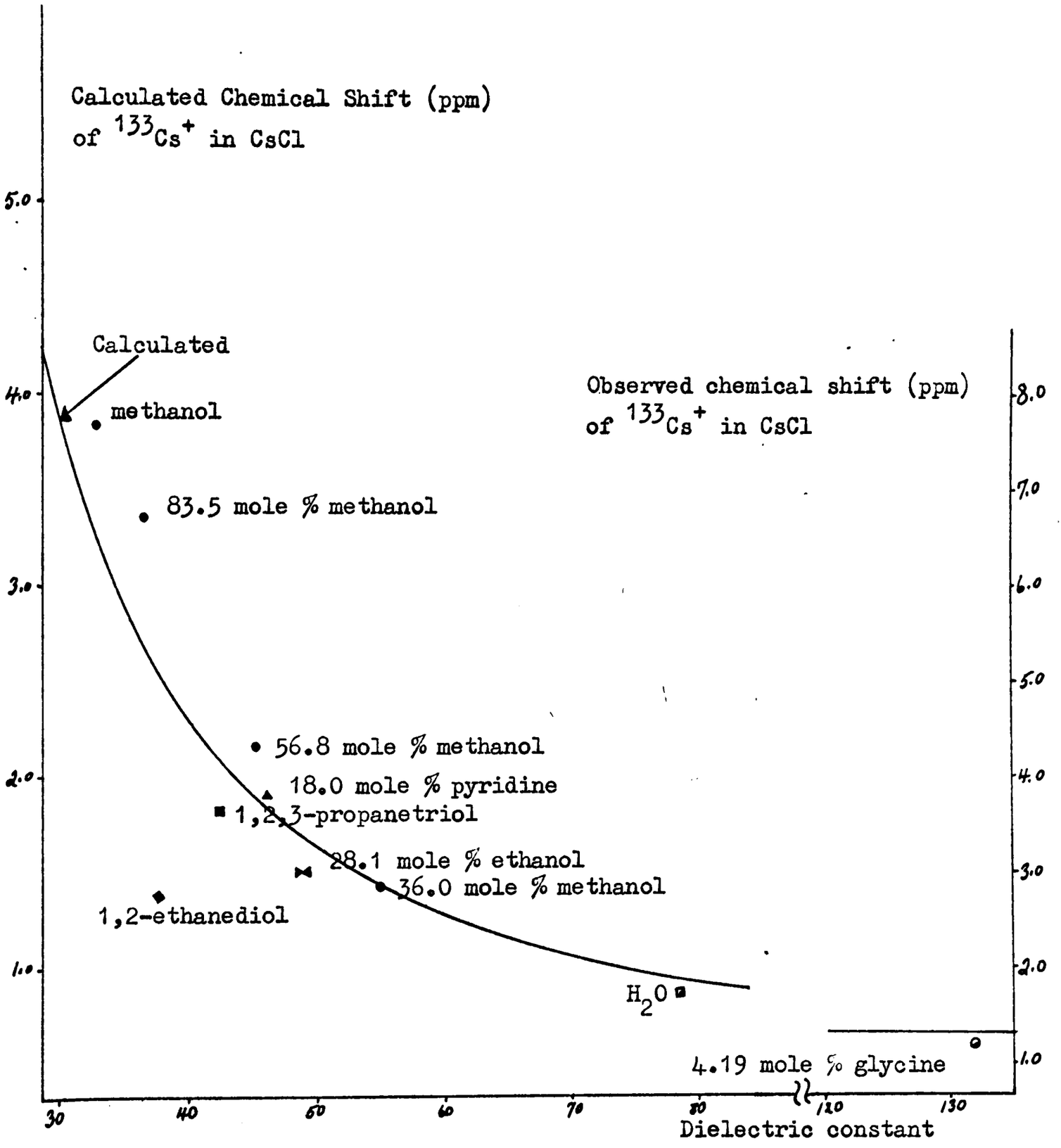


Figure 7.7 $^{133}Cs^+$ chemical shift of 0.1 M CsCl in various mixed solvents.

Appendix 1.

EXPERIMENTAL DATA.

$^{133}Cs^{+}$ CHEMICAL SHIFTS (Hz)

Measuring Frequency 28.013MHz

Temp. (unless otherwise STATED) $25 \pm 0.1^{\circ}C$

Concentrations expressed as Moles/kg H_2O

All shifts referenced to an external standard of 1.994M $CsCl/H_2O$

CsCl in :-

H_2O		D_2O		$H_2{}^{18}O$	
Conc.	Shift	Conc.	Shift	Conc.	Shift
10.508	1332.7	8.705	1218.4	8.653	1209.8
10.182	1290.4	8.568	1204.3	6.764	905.4
9.083	1135.2	7.313	990.9	2.823	206.8
8.009	980.1	6.492	857.0	1.931	29.0
6.854	806.7	6.032	780.3	0.741	-234.7
6.183	705.8	5.439	675.2	0.315	-351.2
4.859	493.6	4.891	580.0	0.174	-395.7
3.731	310.2	3.444	316.4	0.0926	-429.4
3.346	240.0	2.201	62.5	0.0378	-450.7
2.201	36.8	1.302	-122.0	0.0123	-465.0
1.994	0.0	1.045	-185.6		
1.737	-48.1	0.694	-274.1		
1.540	-87.4	0.539	-313.5		
1.295	-135.2	0.434	-348.0		
1.000	-197.4	0.209	-415.4		
0.845	-233.3	0.117	-447.9		
0.616	-277.5	0.0551	-477.9		
0.460	-322.4	0.0222	-492.4		
0.397	-338.4				
0.270	-373.4				
0.166	-406.4				
0.0535	-443.4				

CsBr in :-

H_2O		H_2O (59.3°C)	H_2O (89.5°C)
Conc.	Shift	Shift	Shift
4.714	975.9		
3.830	763.0		
3.089	574.9		
2.506	422.1		
1.878	237.6		
1.036	-24.9	-44.0	-57.7
0.411	-247.9	-264.9	-284.6
0.252	-323.5	-338.6	-357.3
0.196	-349.9	-364.4	-386.9
0.128	-385.9	-400.6	-418.7
0.0837	-411.5	-422.9	-444.9
0.0663	-421.3	-	-457.9
0.0390	-439.9	-452.7	-474.9
0.0180	-456.4	-470.0	-492.7
0.0096	-466.4		

CsBr in :-

D_2O		D_2O (59.3°C)	D_2O (89.5°C)
Conc.	Shift	Shift	Shift
0.926	-36.8	-	-77.6
0.617	-164.2	-191.0	-203.1
0.421	-253.3	-269.5	-287.1
0.272	-324.3	-337.5	-356.3
0.174	-379.3	-394.0	-411.3
0.109	-417.4	-431.0	-452.6
0.0678	-445.4	-459.0	-480.4
0.0523	-458.4	-	-489.4
0.0317	-477.9	-488.0	-508.9
0.0187	-489.4	-496.0	-520.7
0.0101	-496.5	-505.6	-

$CsNO_3$ in :-

H_2O	
Conc.	Shift
1.32	-554.1
0.565	-528.4
0.389	-516.3
0.279	-508.8
0.113	-493.8
0.105	-491.3
0.0672	-486.8
0.0526	-485.3
0.0511	-483.8
0.0372	-481.3
0.0252	-479.3
0.0169	-478.7
0.0106	-476.8

D_2O	
Conc.	Shift
0.645	-575.0
0.261	-546.4
0.146	-536.4
0.0912	-528.4
0.0513	-520.4
0.0166	-511.8

CsI in :-

H_2O	
Conc.	Shift
2.792	1085.4
1.995	744.2
0.976	235.8
0.556	-24.1
0.273	-209.5
0.114	-340.5
0.0587	-394.5
0.0150	-453.1

CsOH in :-

H_2O	
Conc.	Shift.
1.660	-228.0
1.065	-307.7
0.874	-333.3
0.454	-392.8
0.231	-428.6
0.196	-432.4
0.104	-448.9
0.0606	-457.6
0.0291	-465.2
0.0069	-468.8
0.0034	-470.7

CsCl in :-

CH_3OH		CD_3OD		CH_3OD	
Conc.	Shift	Conc.	Shift	Conc.	Shift.
0.1033	-1536.8	0.1038	-1510.1	0.1046	-1517.8
0.0671	-1578.9	0.0515	-1581.6	0.0565	-1578.3
0.0395	-1623.5	0.0290	-1627.3	0.0295	-1630.8
0.0218	-1656.6	0.0176	-1653.7	0.0120	-1677.8
0.0110	-1687.0	0.0093	-1683.7		
		0.0050	-1705.4		

CsCl in CH_3OH/H_2O Solutions

Mole Fraction CH_3OH

0.3600		0.5675		0.8350	
Conc.	Shift	Conc.	Shift	Conc.	Shift
1.420	-312.4	0.809	-624.7	0.273	-1192.4
0.754	-522.1	0.613	-715.9	0.192	-1256.4
0.560	-593.9	0.329	-858.7	0.102	-1331.5
0.328	-682.6	0.184	-940.7		
0.218	-733.4				

CsCl in :-

1, 2 -ethanediol		1,2, 3 -propanetriol	
Conc.	Shift	Conc.	Shift
0.8001	-275.3	0.281	-210.0
0.392	-425.0	0.134	-278.0
0.214	-497.7	0.0705	-308.5
0.112	-548.6		
0.0503	-587.0		

CsCl in 1, 2 -ethanediol/H_2O

Mole Fraction 1, 2 -ethanediol	Conc. CsCl	Shift
0.3802	0.100	-482.0
0.5051	0.100	-497.5
0.7394	0.100	-529.8

CsCl in Ethanol/H_2O

Mole fraction ethanol	Conc. CsCl	Shift
0.2323	0.100	-384.3
0.2813	1.689	257.3
	1.098	64.5
	0.635	-105.8
	0.371	-217.9
	0.233	-293.4
0.3571	0.100	-276.6
0.5410	0.100	-276.6

CsCl in :-

Solvent	Mole fraction Organic component	Conc. CsCl	Shift
Propan-1-ol/H_2O	0.5000	0.100	-236.9
Propan-2-ol/H_2O	0.4938	0.100	55.0
2-Methyl Propan-2-ol/H_2O	0.4969	0.100	296.4
Formamide	1.000	0.1206	-454.1
		0.0895	-475.6
Formic Acid	1.000	0.1132	-1153.4
		0.0974	-1159.4
Formaldehyde	(36%w/v)	0.1024	-440.1
		0.0905	-443.4
Acetic Acid	1.000	0.1082	7.9
		0.0861	-7.9
Hydrazine hydrate	1.000	0.1008	616.0
Hydrogen peroxide	(100 vol)	0.100	1241.2

CsI in :-

Solvent	Mole fraction Organic component	Conc.	Shift
Dimethylsulphoxide	1.000	0.100	1590.1
Formamide	1.000	0.100	-420.3

CsCl in Pyridine/H_2O

Mole fraction Pyridine

0.180		0.434	
Conc.	Shift	Conc.	Shift
0.946	129.9	0.0886	93.3
0.624	-12.8	0.0540	70.0
0.426	-112.8		
0.309	-171.5		
0.166	-295.5		
0.0843	-319.2		

CsCl in Tetrahydothiophen-1,1-dioxide/H_2O

Mole fraction tetrahydrothiophen-1,1-dioxide

0.2086		0.5758	
Conc.	Shift	Conc.	Shift
0.855	177.4	0.134	196.9
0.626	81.3	0.0869	124.7
0.509	31.7	0.0646	82.4
0.355	-44.6	0.0381	38.0
0.284	-86.1	0.0183	-3.8
0.125	-167.7	0.0058	-38.3
0.0757	-203.2		
0.0338	-233.5		
0.0163	-250.7		

CsI in tetrahydrothiophen-1,1-dioxide/H_2O

Mole fraction tetrahydrothiophen-1,1-dioxide

0.5758		0.7405		1.000	
Conc.	Shift	Conc.	Shift	Conc.	Shift
0.116	217.3	0.0704	272.2	0.0882	724.9
0.0639	119.3	0.0347	158.5	0.0585	589.7
0.0312	42.9	0.0142	81.2	0.0407	484.7
0.0142	-11.1	0.0062	38.7	0.0221	356.8
				0.0132	282.0

CsCl in 0.0419 mole fraction glycine/H_2O

Conc.	Shift
1.0215	- 61.0
0.590	-160.7
0.325	-229.5
0.144	-280.3
0.0623	-300.3

^{35}Cl Chemical shift from CsCl/H_2O solutions. Reference ^{35}Cl in 1.994 M CsCl/H_2O

Conc.	Shift
10.182	588.8
9.083	517.9
6.854	376.3
6.183	327.3
4.859	230.6
3.346	118.1
1.994	0.0
0.845	-110.9
0.460	-158.7
0.166	-202.3
0.0535	-225.4

References

1. F. Bloch, W. W. Hansen, and M. Packard, Phys. Rev., 69, 127 (1946)
2. E. M. Purcell, H. C. Torrey, and R. V. Pound, Phys. Rev., 69, 37 (1946)
3. Z. Luz and G. Yagil, J. Phys. Chem., 70, 554 (1966)
4. A. G. Marshall, Biochem., 7, 2450 (1968)
5. R. Freeman, R. P. H. Gasser, R. E. Richards, and D. H. Wheeler, Mol. Phys., 2, 75 (1959)
6. R. Freeman, R. P. H. Gasser, and R. E. Richards, Mol. Phys., 2, 301 (1959)
7. R. P. H. Gasser and R. E. Richards, Mol. Phys., 2, 357 (1959)
8. R. E. Richards and B. A. Yorke, Mol. Phys., 6, 289 (1963)
9. C. Deverell and R. E. Richards, Mol. Phys., 10, 551 (1966)
10. C. Deverell and R. E. Richards, to be published
11. N. Bloembergen, E. M. Purcell, and R. V. Pound, Phys. Rev., 73, 679 (1948)
12. F. Bloch, W. W. Hansen, and M. Packard, Phys. Rev., 70, 474 (1946)
13. H. D. W. Hill and R. E. Richards, J. Scient. Inst. (J. of Phys. E) Series 2, 1, 977 (1968)
14. A. Abragam, The Principles of Nuclear Magnetism, p.44 Oxford University Press, London, 1961)
15. F. A. Nelson and H. E. Weaver, Science, 146, 223 (1964)
16. See ref. 13
17. O. Howarth and R. E. Richards, Progress in N.M.R. Spectroscopy, 1, 1 (Pergamon Press, Oxford, 1966)

18. Technical Information Bulletin, Varian Associates, 3, No. 1 (1960)

19. R. R. Ernst, Rev. Sci. Inst., 36, 1689 (1965)

20. R. R. Ernst, Advances in Magnetic Resonance 2, 1 (Academic Press, New York, 1967)

21. H. Riemersma, J. K. Hulm, and B. S. Chandrasekhar, Advances in Cryogenic Engineering, 9, 329 (Plenum Press, New York, 1964)

22. D. H. Parkinson and B. E. Mulhall, The Generation of High Magnetic Fields, p.113 (Heywood Books, London, 1967)

23. J. C. Maxwell, Treatise on Electricity and Magnetism, 3rd Ed., Vol. 2, sect. 715 (Clarendon Press, Oxford, 1892)

24. M. W. Garrett, J. Appl. Phys., 22, 1091 (1951)

25. H. L. Marshall and H. E. Weaver, J. Appl. Phys., 34, 3175 (1963)

26. J. Gaffney and J. R. Clement, Rev. Sci. Inst., 26, 620 (1955)

27. D. ter Haar, Conférence de Physique des basses températures, Paris, 2-8 Sept., 1955

28. W. G. Proctor and H. E. Weaver, N. M. R. in Chemistry, p.7, Ed. B. Pesce (Academic Press, New York, 1965)

29. M. J. E. Golay, Private communication

30. A. G. Redfield, Rev. Sci. Inst., 27, 230 (1956)

31. W. Lamb, Phys. Rev., 60, 817 (1941)

32. N. F. Ramsey, Phys. Rev., 78, 699 (1950)

33. Y. Yamagata, J. Phys. Soc. Jap., 19, 10 (1964)

34. K. Yosida and T. Moriya, J. Phys. Soc. Jap., 11, 33 (1956)

35. J. Kondo and J. Yamashita, J. Phys. Chem. Solids, 10, 245 (1959)

36. D. Ikenberry and T. P. Das, J. Chem. Phys., 43, 2199 (1965)

37. D. Ikenberry and T. P. Das, Phys. Rev., 138A, 822 (1965)

38. D. Ikenberry and T. P. Das, J. Chem. Phys., 45, 1361 (1966)

39. D. W. Hafemeister and W. H. Flygare, J. Chem. Phys., 44, 3584 (1966)

40. H. S. Gutowsky and B. R. McGarvey, J. Chem. Phys., 21, 1423 (1953)

41. N. Bloembergen and P. P. Sorokin, Phys. Rev., 110, 865 (1958)

42. R. Baron, J. Chem. Phys., 38, 173 (1963)

43. A. Loewenstein, M. Shporer, P. C. Lauterbur, and J. E. Ramirez, Chem. Comm., p.214 (1968)

44. C. Deverell, Review, Nuclear Magnetic Resonance Studies of Electrolyte Solutions, to be published.

45. K. M. S. Saxsena and P. T. Narasiran, Int. J. Quantum Chem., 1, 731 (1967)

46. R. A. Robinson and R. H. Stokes, Electrolyte Solutions, p.79, (Butterworths, London, 1959)

47. G. Burns, Phys. Rev., 115, 357 (1959)

48. H. Eyring, J. Walter, and G. E. Kimball, Quantum Chemistry, p.351 (John Wiley & Sons, New York, 1944)

49. R. M. Lawrence and R. F. Kruh, J. Chem. Phys., 47, 4758 (1968)

50. E. A. Guggenheim, Electrolytes, p.47, Proc. Conf. Trieste (1962)

51. See ref. 46, p.495.

52. B. E. Conway, Ann. Rev. Phys. Chem., 17, p.492 (1966)

53. J. Burgess and M. C. R. Symons, Quart. Rev., 22, 276 (1968)

54. A. Carrington, F. Dravnicks, and M. C. R. Symons, Mol. Phys., 3, 174 (1960)

55. International Critical Tables, Vol. 3, 1st Ed., p.94
(McGraw-Hill, New York, 1926)

Abstract.

This thesis describes the construction of a very versatile broadline 10-100MHz frequency swept nuclear magnetic resonance spectrometer equipped with a 50 kilogauss superconducting magnet.

Measurements have been made, using this spectrometer, to obtain chemical shifts of the ^{133}Cs ion to high precision and to very low concentrations (.005M) in aqueous and non-aqueous media. Remarkable effects have been observed and a theory is proposed that can predict the ion-ion contribution to the chemical shift in solution.

Chapter 1 describes the n.m.r. experiment and discusses factors affecting the signal to noise ratio that are relevant for the construction of the spectrometer.

Chapter 2 gives a brief description of the properties of the superconducting materials used to wind the magnet for the spectrometer and describes the construction and handling of the magnet and its related components.

Chapter 3 describes experiments made on the superconducting magnet to determine and improve its homogeneity.

Chapter 4 gives an account of the construction of the spectrometer and cites examples of its performance.

Chapter 5 outlines a theory proposed by Dr. R.R. Sharp of this research group to interpret the cesium chemical shifts observed.

Chapters 6 and 7 describe the measurements of cesium chemical shifts in aqueous and non-aqueous media. These shifts are interpreted in terms of the theory proposed in chapter 5.

The Appendix contains the raw experimental data obtained for this thesis.